https://theses.gla.ac.uk/

Theses Digitisation:

https://www.gla.ac.uk/myglasgow/research/enlighten/theses/digitisation/

This is a digitised version of the original print thesis.

Copyright and moral rights for this work are retained by the author

A copy can be downloaded for personal non-commercial research or study, without prior permission or charge

This work cannot be reproduced or quoted extensively from without first obtaining permission in writing from the author

The content must not be changed in any way or sold commercially in any format or medium without the formal permission of the author

When referring to this work, full bibliographic details including the author, title, awarding institution and date of the thesis must be given

Enlighten: Theses
https://theses.gla.ac.uk/
research-enlighten@glasgow.ac.uk

ANALYTICAL ELECTRON MICROSCOPY OF INTERFACES IN CATHODIC ARC COATINGS

Maureen MacKenzie

submitted for the degree of Doctor of Philosophy at the Department of Physics and Astronomy, University of Glasgow.

January, 1997

© Maureen MacKenzie, 1997

ProQuest Number: 10992113

All rights reserved

INFORMATION TO ALL USERS
The quality of this reproduction is dependent upon the quality of the copy submitted.

In the unlikely event that the author did not send a complete manuscript
and there are missing pages, these will be noted. Also, if material had to be removed,
a note will indicate the deletion.

ProQuest 10992113

Published by ProQuest LLC (2018). Copyright of the Dissertation is held by the Author.

All rights reserved.
This work is protected against unauthorized copying under Title 17, United States Code
Microform Edition © ProQuest LLC.

ProQuest LLC.
789 East Eisenhower Parkway
P.O. Box 1346
Ann Arbor, MI 48106 – 1346

Thesis
10705
Copy 1

DECLARATION

This thesis is a record of work carried out by me in the Department of Physics and Astronomy at the University of Glasgow. The work described herein is my own, apart from the preparation of the coatings. The coatings were provided by Multi-Arc (UK) Ltd. Some of the work contained in this thesis has been published in the following papers:

MacKenzie, M., Craven, A.J., Nicholson, W.A.P. and Hatto, P. (1996) in "Proceedings of EUREM 1996, Dublin." published by Eurem'96, U.C.D. Belfield, Ireland.

MacKenzie, M., Nicholson, W.A.P., Hatto, P. and Craven, A.J. (1995) in " EMAS'95 - Modern developments and Applications in microbeam Analysis" (Eds. D. Benoit, J.-F. Bresse, L. Van't dack, H. Werner and J. Wernisch) published by European Microbeam Analysis Society, Antwerp, p.376

MacKenzie, M., Scott, C.P., Nicholson, W.A.P. Hatto, P. and Craven, A.J. (1994) in "Emas'94 - Electron Probe Microanalysis of Materials today - Practical Aspects" (Ed. E. Heikinheimo) published by Helsinki University of Technology, Helsinki.

Some of the results in chapter 4 were presented at EMAG'95 in Birmingham.

This thesis has not been previously submitted for a higher degree.

for my mum and late dad

CONTENTS

Summary iv

Acknowledgements vi

List of table headings viii

List of figure headings x

Chapter 1 Introduction

1.1	Hard coatings - general review	1
1.2	Cathodic arc evaporation	4
1.3	Review of previous studies	6
1.4	This work	12

Chapter 2 Instrumentation and experimental techniques

2.1	Introduction	15
2.2	Deposition of samples	16
2.3	Specimens	17
2.4	SEM	18
2.5	CTEM	
	2.5.1 CTEM bright and dark field imaging	18
	2.5.2 CTEM diffraction techniques	19
2.6	The extended VG HB5 STEM	20

2.7 EELS

2.7.1 The EELS spectrometer 23

2.7.2 EELS - microscope conditions 24

2.7.3 EELS - set-up and collection of data 24

2.8 EDX

2.8.1 EDX detector 28

2.8.2 EDX - microscope conditions 28

2.8.3 EDX - collection of data 29

2.9 Imaging & X-ray mapping on the HB5 30

2.10 Summary 31

Chapter 3 Theoretical considerations and analysis of data

3.1 Introduction 32

3.2 EELS

3.2.1 Theoretical considerations for EELS 33

3.2.2 Analysis of EELS data 36

3.2.3 Calculation of partial cross-sections for EELS analysis 40

3.3 EDX

3.3.1 Theoretical considerations for EDX 44

3.3.2 Analysis of EDX data 47

Chapter 4 CrN coating of Ti(6%Al, 4%V)

4.1 Introduction 50

4.2 Description of samples 52

4.3 Examination of CrN coating surface 54

4.4 Grain size and growth in the samples 55

4.5 Chemical composition and crystallographic structure of samples 62

4.6 Diffraction 75

4.7 Conclusions 80

Chapter 5 Investigation of the sputter cleaning process

5.1	Introduction	82
5.2	Description of samples	83
5.3	Cr sputter cleaning of Ti	87
5.4	Ti sputter cleaning of TiN and subsequent redeposition of TiN	89
5.5	Conclusions	93

Chapter 6 Deposition of droplets

6.1	Introduction	96
6.2	Description of samples	97
6.3	Distribution and shape of droplets	98
6.4	Growth of the coating around droplets	101
6.5	Composition of the droplets and surrounding material	102
6.6	Conclusions	106

Chapter 7 Conclusions and further work

7.1	Effect of sputter cleaning process on the substrate	108
7.2	Microstructure and microchemistry of the coatings	112
7.3	Analytical electron microscopy	115
7.4	Possibilities for further work	115

Appendix A1 Specimen preparation

A1.1	Planar specimen preparation	117
A1.2	Cross-sectional specimen preparation	119
A1.3	Preparation of specimens from standard powders	120

References 121

SUMMARY

The aim of this work was to study the effects of changing the substrate bias and orientation on arc evaporated nitride coatings. The microstructure and microchemistry of the coatings were investigated with emphasis placed on study of the coating/substrate interface region which governs the adhesion of the coating - a property that is vital to the functional performance of the coating. The effect of the sputter cleaning process prior to deposition of the coating was investigated in some detail.

Analytical electron microscopy techniques were employed in the investigations in this thesis. High resolution EELS and EDX line profiles across the interface region were used in analysis of the coatings, as well as bright and dark field imaging, EDX mapping and diffraction techniques. A non-standard diffraction technique, whereby the angle of convergence was decreased to increase the angular resolution, was used in diffraction analysis of the interface region where the diffraction patterns were difficult to resolve. In analysis of EELS data, the use of edges from standard compounds to remove the background from edges in similar compounds was demonstrated.

The substrate pre-treatment of Ti(6%Al, 4%V) by polishing and Cr sputter cleaning resulted in modification of the microstructure at the substrate surface with the formation of small grains of β-Ti(6%Al, 4%V). Cr was implanted in the substrate during the sputter cleaning process resulting in an interface layer

of graded composition; this layer was a bcc alloy of Cr and Ti. Etching of material from the substrate surface also occurred during the sputter cleaning process. Cr sputter cleaning of Ti resulted in both etching and implantation of material although there was net removal of material from the substrate. In contrast Ti sputter cleaning of TiN etched little of the substrate but deposited a layer of Ti, the thickness of which strongly depended upon the orientation of the substrate surface relative to the cathode surface.

Deposition of CrN on Ti(6%Al,4%V) resulted in the initial deposition of a layer of fine grained sub-stoichiometric Cr_2N. This was followed by columnar growth of sub-stoichiometric CrN. Changing the substrate bias from -70V to -200V resulted in deposition of coatings with larger grains and fewer faults.

Increasing the angle of orientation between the substrate surface and the cathode surface led to the deposition of thinner coatings which were of a more uniform thickness. Due to gas scattering the effect of the orientation upon the thicknesses of coatings deposited was much less pronounced during the deposition process than during the sputter cleaning process. For the deposition of the CrN coatings a decrease in the Cr content of the coating and an increase in the grain size was observed as the angle of orientation increased.

The presence of droplets increased the surface roughness of the coatings by about three orders of magnitude and led to defects with voids and growth defects being observed. The deposition of material in the form of droplets also showed a strong dependence on the orientation of the substrate to the cathode with the number of droplets deposited decreasing as the angle of orientation increased.

ACKNOWLEDGEMENTS

First of all I would like to sincerely thank my supervisors Drs Alan Craven and Patrick Nicholson for all their help and guidance throughout my research as well as their patience. I would also like to thank my industrial supervisor Dr Peter Hatto at Multi-Arc (UK) Ltd. for all his useful discussions and suggestions as well as arranging for my samples to be made.

I wish to express my gratitude to Prof John Chapman for helping me to decide to do this project (thank you!) as well as for his support and provision of facilities within the Solid State Physics group.

Also, thanks to EPSRC and Dr Ray Fontana of Multi-Arc for providing the funding for this CASE award.

Thanks to Dr Clive Davies and Mr Alan Holmes at Multi-Arc for depositing the samples.

A special big thank you to Dr Colin Scott who taught me how to make specimens and was always willing to help me.

For technical support I am indebted to the following people -
Mr Alan Howie for maintenance of the HB5 and for his patience with all my computer problems, Mr Steven Connor and Mr Colin How for maintenance of

the JEOL microscopes and developing negatives, Mr Donald MacDonald and Mr Andy Young for helping with the ion mill, the late Mr Jim Simms for maintenance of the JEOL microscopes, the late Miss Margaret Low for developing negatives and for teaching me how to, and Mr Iain Selkirk in the workshop.

Thanks to all other members of SSP both past and present for all help, advice and useful discussions on various topics.

I would like to thank -

my supervisors, Dr Pauline Thompson, Mr Richard Lindsay, Miss Flora MacKintosh, Miss Donna Ross, Miss Elizabeth Tallach and Dr Katherine Kirk

for reading chapters or sections of this thesis.

A big thank you to my flatmates who, as well as reading chapters, put up with a severe lack of social interaction over the last few months. Also to all my friends who kept phoning and writing me in spite of my reclusive lifestyle - especially Sheena Ross, Saiqa Khan, Fiona Dick and Fiona Thompson. I would like to give a special mention to Jan, Alice and family for providing a second home for me in Glasgow.

And anybody and everybody else who has helped me in the last three and a bit years.

Finally, a big big thank you to my mum and family.

List of table headings

1.1	Performance data summary for 1984 for TiN recoatings at an auto transmission plant (Hatto, 1996)	2
1.2	Characteristics of different pvd processes (Hatto et al, 1996)	3
1.3	Relative abundance, n_i and average energies, E_i of ions of various ionisation states for Cr and Ti arcs (Lunev et al, 1977)	6
2.1	EELS edges examined	26
2.2	EDX peaks of interest	29
3.1	Integration windows for table 3.2	43
3.2	Experimental Cr/N values calculated using different integration windows	43
3.3	Integration windows for analysis of EELS data	44
3.4	Bethe parameters calculated by Paterson et al (1989)	47
3.5	Atomic data for Ti and Cr cross-sections calculated from non-relativistic Bethe model for 100keV	48
3.6	Absorption coefficients (Heinrich, 1979) and densities (Kaye & Laby, 1975)	49
4.1	Summary of sputter cleaning and deposition parameters of samples discussed in this chapter	53
4.2	Summary of typical grain size observed in planar section	57
4.3	CrN coating thickness	59
4.4	Position of first plasmon for Ti and Cr in energy loss spectroscopy	65

4.5	Width of Ti:Cr alloy and Cr_2N layers from EELS line profiles	68
4.6	Estimated tilt errors during EELS microanalysis	70
4.7	Nitrogen to chromium ratios in the coatings	71
4.8	Width of the Ti:Cr alloy layer from EDX line profiles	74
4.9	Lattice parameters of materials of interest	75
5.1a	Summary of sputter cleaning and deposition parameters for preparation of substrates on Si wafers	84
5.1b	Sputter cleaning and coating parameters for treatment of substrates	84
5.2	Energy windows used to collect the X-ray maps in figure 5.4	88
5.3	Layer thicknesses after Ti sputter clean and TiN recoat	91
6.1	Summary of samples studied in this chapter	97

List of figure headings

1.1 Schematic diagram of cathodic arc evaporation coating chamber

1.2 Schematic of potential hump (Plyotto et al, 1965) in front of the cathode and schematic diagram of plasma process

2.1 Schematic cross-section of copper block for deposition at different orientations

2.2 Schematic of a planar specimen

2.3 Schematic of a cross-sectional specimen

2.4 The optical alignment of the VG HB5 STEM as used for the collection of EELS data

2.5 Schematic of the Gatan 666 PEELS detector

3.1 Electron energy loss spectrum

3.2 N K edge in CrN, VN and $TiN_{0.88}$ standards

3.3 N K edge in CrN, VN and $TiN_{0.88}$ standards interpolated for lattice parameters

3.4 N K edge in CrN standard being used to remove background from Ti $L_{2,3}$ edge

3.5 N K edge and cross-sections calculated by EL/P

3.6 Ti $L_{2,3}$ edge and cross-sections calculated by EL/P

3.7 Cr $L_{2,3}$ edge and cross-sections calculated by EL/P

3.8 Experimental Cr/N values obtained as a function of collection semi-angle

3.9 Energy dispersive X-ray spectrum

4.1 SEM image of parallel sample of CrN deposited at -70V
4.2 SEM image of 45° sample of CrN deposited at -70V
4.3 SEM image of perpendicular sample of CrN deposited at -70V
4.4 SEM image of sample of CrN deposited at -150V
4.5 Parallel CrN sample deposited at -70V
4.6 45° CrN sample deposited at -70V
4.7 Perpendicular CrN sample deposited at -70V
4.8 Parallel CrN sample deposited at -200V
4.9 45° CrN sample deposited at -200V
4.10 Perpendicular CrN sample deposited at -200V
4.11 10° CrN sample deposited at -150V
4.12 Cr sputter cleaned substrate
4.13 Parallel CrN sample deposited at -70V
4.14 Parallel CrN sample deposited at -70V
4.15 45° CrN sample deposited at -70V
4.16 Perpendicular CrN sample deposited at -70V
4.17 Parallel CrN sample deposited at -200V
4.18 45° CrN sample deposited at -200V
4.19 Perpendicular CrN sample deposited at -200V
4.20 Perpendicular CrN sample deposited at -70V
4.21 EELS line profile across grain boundary in -150V sample
4.22 EDX line profile of parallel -200V sample
4.23 EELS line profile of parallel -200V sample
4.24 EELS line profile of parallel -200V sample
4.25 Onset of N signal in line profile in figure 4.24
4.26 Cr:Ti phase diagram (Hansen, 1958)
4.27a First plasmon in spectra from Ti, Cr and alloys of Ti:Cr of graded composition
4.27b First plasmon in Ti:Cr alloy of roughly 1:1 composition and sum of first plasmons from Ti and Cr
4.28 EELS spectra from Cr_2N standard and region C1

4.29 EELS spectra from CrN standard and region C2
4.30 EELS line profile of parallel -70V sample
4.31 EELS line profile of 45° -70V sample
4.32 EELS line profile of perpendicular -70V sample
4.33 EELS line profile of 45° -200V sample
4.34 EELS line profile of perpendicular -200V sample
4.35 White lines in Ti $L_{2,3}$ edge
4.36 White lines in Cr $L_{2,3}$ edge
4.37 Ring patterns calculated using Diffract
4.38 Changing the angular resolution
4.39 Line scan diffraction sequence across interface
4.40 Diffraction pattern obtained scanning over region of coating
4.41 Selected area diffraction patterns from planar specimen
4.42 Point diffraction patterns from planar specimen
5.1 Special substrate to allow determination of original substrate surface
5.2 Ti layer deposited on Si wafer and capped with Hf
5.3 As in figure 5.2 but Cr sputter cleaned prior to Hf capping
5.4 X-ray maps of Cr sputter cleaned Ti sample
5.5 EDX line profile of Cr sputter cleaned Ti sample
5.6 Stationary parallel TiN recoat sample
5.7 Stationary 45° TiN recoat sample
5.8 Stationary perpendicular TiN recoat sample
5.9 EELS line profile for stationary perpendicular TiN recoat sample
5.10 Rotating parallel TiN recoat sample
5.11 Rotating perpendicular TiN recoat sample
5.12 EELS line profile for rotating perpendicular TiN recoat sample
6.1a Stationary parallel TiN coating
6.1b Stationary 45° TiN coating
6.1c Stationary perpendicular TiN coating

6.2a Rotating parallel TiN coating

6.2b Rotating 45° TiN coating

6.2c Rotating perpendicular TiN coating

6.3 Cr droplets in planar specimen

6.4 Cr droplet in cross-sectional specimen

6.5 Cr droplet in cross-sectional specimen

6.6 Cr droplet in planar specimen

6.7 EDX line profile across region in figure 6.6

6.8 EELS line profile across region in figure 6.6

6.9 Cr droplet in cross-sectional specimen

6.10 EDX line profile across region in figure 6.9

6.11 EELS line profile across region in figure 6.9

6.12 Schematic diagram of mesa droplet and surrounding material

6.13 Cr droplet in cross-sectional specimen

CHAPTER 1

Introduction

1.1 Hard coatings - general review

This introductory chapter begins by describing the commercial relevance of the coatings under investigation. The next section describes cathodic arc evaporation in more detail. A brief description of the coating chamber is given, followed by a discussion of the production of the plasma. The interaction of the ions with the substrate surface is also considered. Section 1.3 reviews previous studies of cathodic arc coatings which are pertinent to this work. The aim of this work is discussed in section 1.4 where a brief outline of this thesis is also given.

Hard coatings are used to enhance the surface of materials and increase their wear and corrosion resistance. There are many applications of hard coatings but one place where hard coatings have made a large technical and financial impact is in the tooling industry.

Increasing the wear resistance of tools, increases their life and hence reduces manufacturing costs. Such costs are not only associated with the initial purchase price of the tools but also with the need, in many instances, to regrind

them. Increased wear resistance decreases the need for regrinding and it also means that less material is removed when they are reground. The obvious benefit of this is that the tools last longer. While this saves money the real benefit comes from the fact that the coated tools can cut both faster and deeper, and hence the productivity of machines and operators is greatly enhanced providing much larger financial benefits than related to tooling costs alone. Further savings can be made by recoating the tools. Table 1.1 shows some typical data.

Table 1.1 *Performance data summary for 1984 for TiN recoatings at an auto transmission plant (Hatto, private communication).*

	uncoated	coated	recoated
hob			
gear cuts per tool	8000	14000	83200
tooling cost per gear ($)	0.02171	0.01265	0.00542
shaper cutter			
gear cuts per tool	1750	3653	31200
tooling cost per gear ($)	0.1406	0.1029	0.0320

For the purposes of wear resistance, transition metal nitride and carbide coatings have proved extremely successful (Sundgren et al, 1986). Although intrinsically brittle in the bulk, these materials loose this intrinsic brittleness when applied in thin films as coatings (Mack, 1990). The most common hard coating is TiN which has been widely used as a hard coating for many years. However, there are many different coatings available including metals, ceramics and multilayers. The particular coating used depends upon the application. For example, CrN has better corrosion resistance (Mack, 1990) and an equal or lower coefficient of friction than TiN (Erturk et al, 1989) and thus performs better in applications such as hot forming.

There are numerous coating techniques available but they fall into two general categories - chemical vapour deposition and physical vapour deposition.

Chemical vapour deposition (cvd) can be defined as a reaction of volatile components at the surface of a substrate with the formation of a solid surface layer and volatile reaction products (Habig, 1986). This technique requires high temperatures (normally 850-1250C) and high pressures (1-1000mbar) to ensure the necessary catalytic influence of the substrate surface on the process.

In physical vapour deposition (pvd) the coating is deposited from vapour derived using physical processes - evaporation or atomistic/ionic bombardment (sputtering). Although compound coatings may be deposited directly from compound sources, it is more normal to use reactive processes. Here metal ions in the vapour condense onto the substrate surface and react with a reactive gas to produce the coating. The deposition is normally done with substrate temperatures between 200-600C and a chamber pressure of 10^{-4}-10^{-1}mbar (Habig, 1986). Two main advantages of physical vapour deposition are that it is a relatively low temperature process and that it does not cause environmental pollution. The low temperature aspect is very important because it means that steel components can be coated without having to be reheat-treated.

To obtain good adhesion of coatings deposited at low temperatures the following stipulations must be met:

i) the ions must be energetic

ii) the ion current density at the substrate must be high

iii) there must be a high ion fraction in the metal vapour

(Mack, 1990).

Table 1.2 *Characteristics of different pvd processes (Hatto et al, 1996).*

	ionisation	average energy (eV)	ionisation state
magnetron sputtering	<5%	2-5	+1e
cathodic arc evaporation	>60%	50-100	+2e

Table 1.2 compares cathodic arc evaporation with magnetron sputtering which is another successful pvd process. It can be seen that cathodic arc evaporation offers the higher degree of ionisation and the higher average ion energy of the two techniques. It fulfils all the requirements for well adhered hard coatings at a low temperature as it also provides a sufficiently high ion current density at the substrate (Mack, 1990). Recently it has been shown that a suitably designed target can be operated in arc or magnetron mode (Robinson et al, 1990) leading to the possibility of combining an arc source with magnetron technology. Commercial use of this concept has been implemented by Münz and coworkers (Münz, 1991; Hauzer Holding BV, 1990) and has shown improvements in the adhesion of magnetron sputtered coatings as a result of using the arc source to sputter etch the substrate prior to deposition of the coating (see for example, Ives et al, 1993).

1.2 Cathodic arc evaporation

Cathodic arc evaporation is performed within a vacuum chamber because of the intense plasma reactions. Figure 1.1 shows the key parts of the coating chamber. The chamber walls act as the anode and there are several metal cathodes within the chamber which provide the metal ions for the coating. The substrate is held at negative bias by a power supply so that the metal ions will be accelerated towards it. There is an inlet to allow a reactive or inert gas into the chamber and a vacuum pump to evacuate the chamber There is also a trigger which is momentarily brought into contact with the cathode to initiate the arc.

A general review of the theory describing the production of a plasma from the cathode is given by Hantzsche (1981). Figure 1.2 shows a schematic of the potential in the chamber and the main directions of material transfer within the chamber. The process is initiated by striking an arc on the metal cathode.

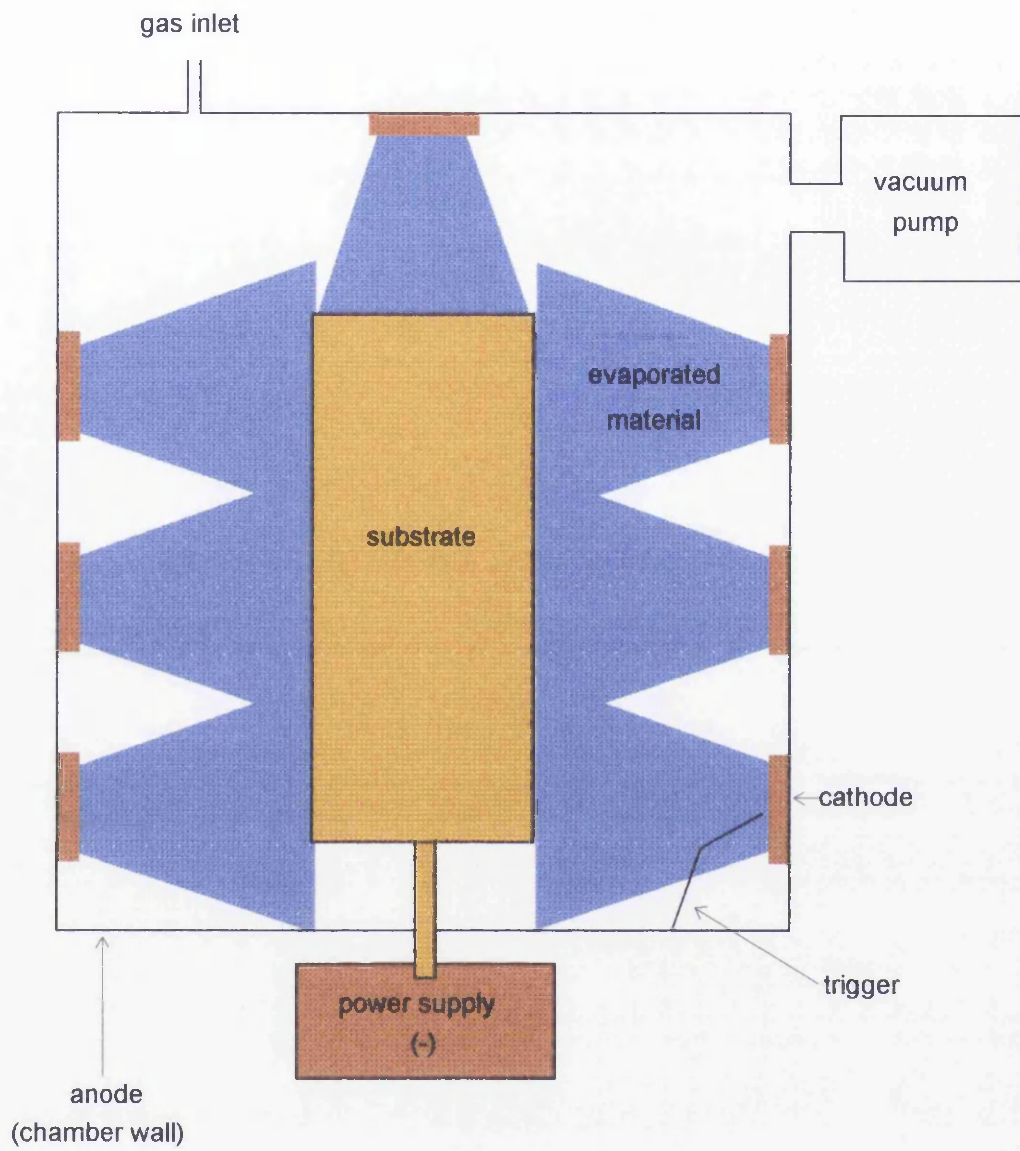

Figure 1.1 *Schematic diagram of cathodic arc evaporation coating chamber.*

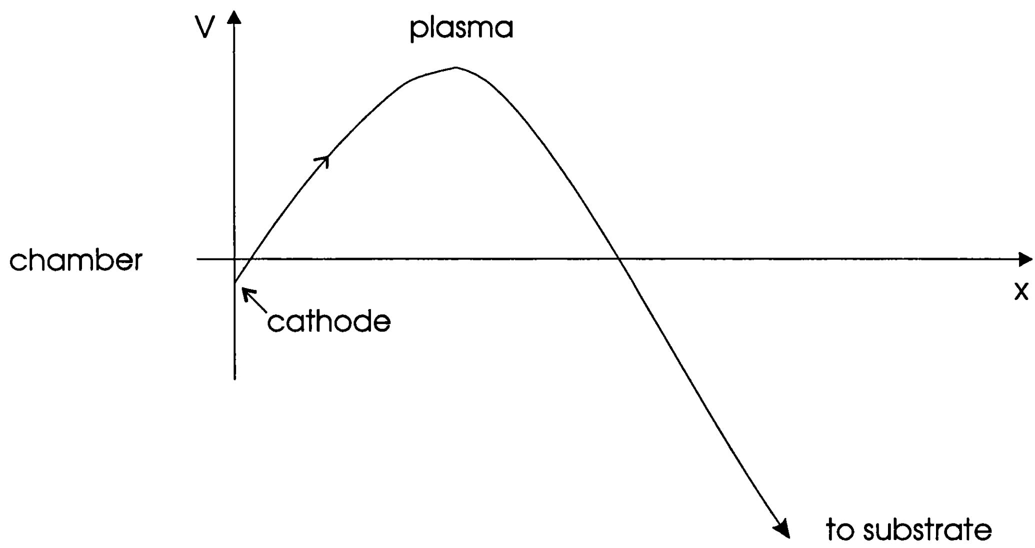

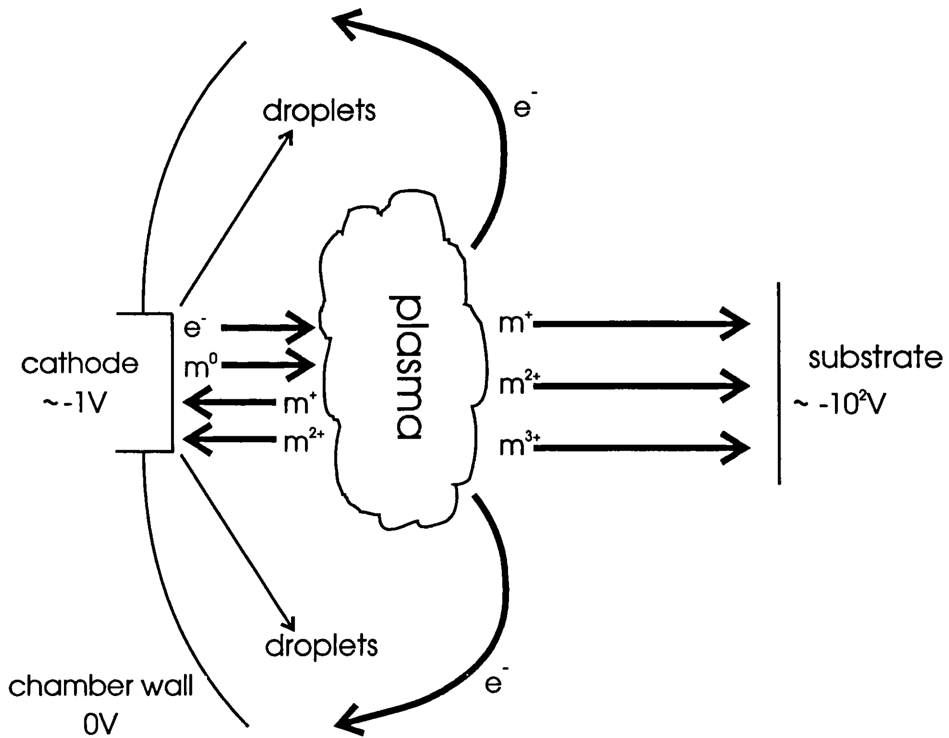

Figure 1.2 *Schematic of potential hump (Plyotto et al, 1965) in front of the cathode and schematic diagram of plasma process.*

Because of the low pressure in the chamber the arc attacks only a small spot rather than the entire cathode so that the phenomenon is known as a cathode spot. The local region of metal is vaporised and forms an intense plasma cloud in front of the cathode. Electrons emitted from the cathode ionise the metal atoms in the plasma cloud. Some of these metal ions flow back towards the cathode bombarding it with sufficient energy to locally melt it, emitting further neutral metal atoms, metal ions and electrons. Droplets of molten metal are also released from the cathode surface around the cathode spot during the process. The cathode spot is not stationary but moves rapidly over the cathode surface.

Metal ions emerging from the other side of the plasma are rapidly accelerated towards the negatively biased substrate and bombard it with high energies. The nature of the interaction between the incoming metal ion and the surface of the substrate is determined by the energy of the metal ion (Dorodnov, 1978) in contrast to thermal techniques where the energy of the incoming ion is not significant.

For energies in the range of about 3 to 1000eV, the main effect is condensation of ions from the accelerated plasma stream onto the substrate surface. This results in a coating on the substrate and is the basis of the deposition process. As the energy of the incoming ions is increased towards 10^3eV sputtering of the substrate surface becomes increasingly important and a point is reached about 10^3eV where the sputtering rate equals the deposition rate.

Increasing the energy of the ions above 1000eV results in a net removal of material from the surface. Sputtering of the surface layer is accompanied by implantation of ions into the surface layer with the concentration of the arriving species decreasing rapidly with depth (Benninghoven et al, 1987). The result is a surface layer of graded composition which moves into the substrate at the same velocity as the surface itself during the sputtering process.

It has been found that the adhesion between the coating and the substrate is improved if the substrate surface is sputtered with the same ion species in vacuum prior to deposition of the coating (Dorodnov, 1978). This sputtering cleans the substrate surface by removing surface oxides and produces an interface region between the substrate and the coating in the form of a layer of graded composition at the substrate surface. This interface region adheres well to both the substrate and the coating.

In cathodic arc evaporation, the energies of the incoming metal ions are determined by the substrate bias which accelerates the ions and by the ionisation states of the ions. These parameters therefore are of paramount importance to the process. Table 1.3 gives the relative abundance and average energies of various ionisation states found with Cr and Ti cathodes at the source. The ions will gain energy through acceleration by the electric field. However, if there is N_2 gas present in the chamber they will lose energy via gas scattering.

Table 1.3 *Relative abundance, n_i and average energies, E_i of ions of various ionisation states for Cr and Ti arcs (Lunev et al, 1977).*

	ion	charge			
		1+	2+	3+	4+
n_i (%)	Cr	16	68	14	2
E_i (eV)	Cr	73	37	34	
n_i (%)	Ti	27	67	6	
E_i (eV)	Ti	65	39	34	

1.3 Review of previous studies

The properties of the coatings deposited by cathodic arc evaporation depend upon various parameters in the sputter cleaning and coating processes such as

the substrate bias (and hence, the ion energy), the substrate temperature and the gas pressure in the chamber. In order to understand how these parameters are effecting changes in the physical properties of the coatings, it is necessary to characterise the microstructure of the coatings. Such understanding should lead to improvements in the control of coating properties and the reproducibility of the process.

The overall picture for the microstructure of sputtered metal coatings was determined in early work by Movchan and Demchishin (1969) and Thornton (1974). Movchan and Demchishin (1969) documented the effect of the substrate temperature on the structure of evaporated coatings. They split the temperature scale into three ranges in which they observed different microstructures. At low temperatures they observed tapered crystals with domed tops whose width increased with temperature. Columnar grains were observed for $0.25\text{-}0.3 < T/T_m < 0.45$ where T is the substrate temperature and T_m is the melting point of the material being deposited. For higher temperatures the structure consisted of equiaxed grains. Thornton (1974) extended this model for sputtered coatings up to ~25μm thick by investigating the effect of argon pressure as well as temperature on the microstructure. Thornton's results were similar to those of Movchan and Demchishin. For low temperatures he observed tapered crystallites separated by voids which filled in as the temperature increased and the structure passed into a transition zone of tightly packed fibrous grains which generally did not extend through the coating. Increasing the temperature increased the length and width of these grains so that between T/T_m of ~0.4 and 0.75 columnar grains were observed. Increasing the Ar pressure increased the temperature necessary to achieve columnar growth. The gross features in the columnar growth region were independent of the argon pressure. For higher temperatures equiaxed grains were observed for Cu coatings deposited at very high deposition rates (10 000-20 000 Å/min). High Ar pressures at low temperatures generally led to more voids in the structures. At higher temperatures the effect of increasing the Ar pressure was reduced. Thornton noted that the results were essentially independent of the substrate material and the deposition rate in the range 1000-2000Å/min.

However, he said that the equiaxed grains seen by Movchan and Demchishin were the result of high deposition rates.

Thornton's studies were for sputtered coatings, the structures of which are very dependent upon the pressure, the substrate bias and the temperature. Large variations in the stoichiometry of sputtered coatings can also be achieved. Arc coatings are almost always close to stoichiometry and columnar grain growth is characteristic (Håkansson, 1991). In cathodic arc deposition the columnar growth is achieved when the temperature of the substrate is only about 25% of the melting point of the coating material. However, the incoming ions are very energetic and hence the effective temperature during deposition is considerably higher than the average substrate temperature as the ions provide energy that was formally supplied as thermal energy.

There have been many investigations of the microstructure and properties of coatings but very few of the interface region between the coating and the substrate. Work in Glasgow has looked mainly at nanoscale multilayers deposited on Si. Some characterisation of interfaces between TiN and steel was done in Linköping in Sweden but the spatial resolution was only of the order of 5nm. Some results from these studies will be discussed below along with other relevant work.

The characterisation of the interface region between the coating and the substrate requires spatial resolution of less than 10nm. Sundgren et al (1986) showed the usefulness of analytical electron microscopy for the microstructural and microchemical characterisation of coatings on such a scale. Previous studies which have been made on the effect of various process parameters on the microstructure and microchemistry of coatings and in particular the interface region using analytical electron microscopy are reviewed below.

The majority of the research on hard coatings reported in literature has been on sputtered films. Some research on cathodic arc coatings has also been reported but due to the complexity of the process and the diversity of parameters, there

is little understanding of the exact relationships between the properties of the coatings and the process parameters. Due to differences in the materials and the difficulty in controlling deposition parameters, it is not easy to correlate differences in microstructure and microchemistry, the properties of the coatings and the changes in process parameters. The effect of some of the process parameters on the microstructure and microchemistry of the coatings have been investigated previously. Some of these effects are now described.

Coatings

An increase in column width with increasing substrate temperature has been observed by Jacobson et al (1979) who studied arc deposited TiN coatings of the order of 20μm thick. The grain sizes varied from 0.5μm at 550C to 20μm at 1000C. This constitutes a considerable change in grain size but the temperatures involved were much greater than those which normally occur during cathodic arc deposition. Gåhlin et al (1995) also observed an increase in grain size with temperature in TiN coatings between ~200C and ~400C. However, the coatings were deposited with different substrate biases and they also noted that the grain size in CrN coatings deposited at the same substrate bias did not appear to be affected by such a change in temperature. In light of this and results presented in chapter 4 of this thesis it seems likely that the changes in grain size observed by Gåhlin et al were a result of changes in the substrate bias.

The substrate bias has been shown to effect the preferred orientation of the coating (Martin et al, 1987; McKenzie et al, 1996; Hatto et al, 1996). The substrate bias also affects the internal stress of the coating. An increase in the substrate bias (and hence the ion energy) was accompanied by a decrease in the lattice parameter and a reduction in stress (Martin et al, 1991).

Modification of the substrate

The crystallographic texture of the substrate surface can be modified by ion bombardment. (111) textured silver and gold films were altered to (110) texture after irradiation (Marinov, 1977). Hexagonal close packed cobalt was converted to face centred cubic cobalt with a (110) texturing (Dobrev, 1982). Dobrev postulated that these modifications in the structures were a result of focusing of collisions along preferred directions in the film. Such channelling of incident particles causes changes in the orientation of the film crystallites. Ion bombardment of other materials such as NaCl, Si and Ge led to the formation of amorphous regions (Martin, 1986).

Gerstner et al (1995) studied C films deposited on Si and noted the presence of an amorphous region at the interface where C had been implanted into the Si. This interface layer had very high bonding to both the coating and the substrate. Mechanical failure occurred in the substrate before delamination of the coating. They postulated that this failure might be a result of damage from the implantation process and suggested that such damage could possibly be annealed out.

The effect of the substrate bias during sputter cleaning on the adhesion of TiN coatings on stainless steel was investigated by Hovsepyan and Dimitrov (1991). They studied sputter cleaning in atmospheres of Ar and of N_2 with biases between -700V and -1500V. They observed that in the presence of Ar the adhesion had its optimum value when the substrate bias was -900V. With a substrate bias of -700V a layer of Ti was deposited, showing that the deposition rate was greater than the sputtering rate. As the bias was increased the thickness of this layer decreased. A TiC layer formed at the interface, the C content of which increased as the substrate bias increased. The adhesion was low when layers of pure Ti were observed but increased as TiC formed as an underlayer. As the thickness of the TiC region increased, the adhesion then decreased because of the brittleness of the TiC. The maximum adhesion was found where there was interdiffusuion between the substrate and the coating

and the layer of TiC was relatively thin. In the presence of N_2 the adhesion increased monotonically as the substrate bias increased, however the values obtained using N_2 were significantly lower than those obtained with Ar. With the N_2 atmosphere TiN was deposited on the surface. As the substrate bias was increased some of the Ti diffused into the steel increasing the adhesion.

Work in Glasgow was done as part of a Link project looking mainly at multilayers deposited on Si substrates. Part of this work showed that to deposit uniform narrow multilayers the substrate should be perpendicular to the cathode surface. The Link work also established the presence of amorphous interface layers. Ti sputter cleaning of a Si wafer resulted in the presence of an amorphous interface layer of Si and Ti of graded composition (Hatto et al, 1996). This amorphous layer was observed whether the sputter cleaning was performed with the substrate surface parallel or perpendicular to the cathode surface. However, the uniformity of the layer increased as the angle of orientation of the substrate surface to the cathode surface increased. Similar amorphous layers containing Ti and Fe of graded composition were observed at the interface between TiN and steel where the steel substrate surface was perpendicular to the cathode surface during the sputter cleaning cycle. In the case of both Si and steel substrates protracted Ti sputtering of the surface resulted in the deposition of a layer of α-Ti on top of the amorphous layer. The uniformity of this layer also increased as the relative orientation of the substrate and cathode surfaces increased.

Research in Linköping looked at the interface between coatings and steel substrates for a variety of pvd techniques including cathodic arc evaporation. The elemental distributions across the interfaces were similar in to those studied in Glasgow although Håkansson (1991) showed the presence of a recrystallised zone between TiN and a steel substrate which had been sputter cleaned with Ti. This recrystallisation could be a result of either the different substrate or different deposition parameters from those used in the Glasgow work. The Linköping substrate had a double rotation motion for both the sputter cleaning and the deposition cycles which would have led to changes in

the instantaneous deposition rates. Yamada et al (1980) and Takagi (1984) observed that the crystallinity of Si films prepared by ionised cluster beam deposition depended on the acceleration voltage and hence the energy of the clusters; increasing the voltage led to the deposition of crystalline films.

1.4 This work

The aim of this work was to study the microstructure and microchemistry of nitride coatings prepared by cathodic arc evaporation and in particular the interface between the coatings and the substrates. By controlling the process parameters, the relationship of some of the parameters to the resultant microstructure and microchemistry could be investigated.

All of the samples studied in this thesis were prepared by Multi-Arc (UK) Ltd. at their coating factory in Consett. Multi-Arc (UK) Ltd. is part of a world-wide network of coating centres (The Ion Bond® Network) using cathodic arc evaporation to produce hard coatings.

Analytical electron microscopy was used to study the microstructure and microchemistry of the samples. Chapter two describes the instrumentation and the analytical techniques employed for this end. In particular electron energy loss spectroscopy and energy dispersive X-ray spectroscopy were used for microchemical analyses across the coating/substrate interfaces.

The use of analytical electron microscopy to study the samples necessitates the preparation of electron transparent regions of sample for examination in the electron microscope. The term 'sample' will be used in this thesis to describe the coating and substrate as it has been prepared by cathodic arc evaporation. The samples as prepared for use in the microscopes will be referred to as specimens. Specimens were prepared in both planar and cross-sectional orientations to allow three-dimensional characterisation of the samples. The

specimen preparation techniques employed were based upon techniques developed by Scott et al (1996) with modifications to overcome some problems peculiar to the type of materials being studied. These techniques are described in appendix A1.

In order to analyse the experimental results, it is necessary to have some understanding of the theoretical background to the experimental techniques. The requisite theoretical considerations are discussed in chapter three where the analysis of the data is also addressed.

The final chapter brings together the conclusions which can be drawn from the results presented in this thesis and discusses the general overview. Further studies following on from this work are suggested.

At an early stage of this project it was decided that the coating of Ti(6%Al, 4%V) would be investigated because this alloy is of current interest to Multi-Arc. It was decided to use CrN to coat the Ti(6%Al, 4%V) because very little had been documented on CrN coatings in literature and it also is of industrial relevance to Multi-Arc. It was decided that the process parameters which would be investigated were the substrate bias during coating and the orientation between the substrate and the cathode. The characterisation of these samples is discussed in chapter 4.

It became apparent during the study of the CrN coatings on Ti(6%Al, 4%V) that it was impossible to determine the direction of net material transfer during the sputter cleaning process because of the nature of the substrate surface. This sputter cleaning process is known to influence the interface between the substrate and the coating and is of great consequence to the adhesion of the coating. Chapter 5 looks at the sputter cleaning process in more detail using specially designed substrates which allow the determination of the net direction of material transfer. The first system investigated was Cr sputter cleaning of Ti. This modelled the Cr sputter cleaning of Ti(6%Al, 4%V) in chapter 4. The second system studied was the Ti sputter cleaning of TiN followed by

deposition of further TiN. This study is of relevance to Multi-Arc because of their interest in the recoating of tools which involves deposition of TiN onto an existing TiN coating. Chapter 6 looks at another aspect of material transfer namely the deposition of droplets at the substrate.

CHAPTER 2

Instrumentation and experimental techniques

2.1 Introduction

The deposition of samples and preparation of specimens are outlined in this chapter which also describes the general analytical electron microscopy techniques and the instrumentation used to collect the data for the results presented in this thesis. Specific techniques will be dealt with in the appropriate results chapters.

Investigation of a sample began by examining its surface in a scanning electron microscope (SEM). This technique gave information on the surface of the coating but not on the bulk of the coating or the substrate.

The grain nucleation, growth and size in the coating were investigated using standard bright and dark field imaging in a conventional transmission electron microscope (CTEM). Diffraction techniques on the CTEM were used to identify the phases present by indexing the diffraction patterns and measuring the lattice parameters.

Investigation of the microchemistry was achieved using electron energy loss spectroscopy (EELS) and energy dispersive X-ray spectroscopy (EDX) performed in a scanning transmission electron microscope (STEM). EELS was used to identify elements present in the specimen and to examine changes in the chemical composition across the coating/substrate interface. In addition, EELS was utilised to determine changes in crystallographic structure. EDX was also used in the identification of elements present and to provide information on changes in chemical composition.

The magnifications and camera lengths of the microscopes were calibrated using cross-gratings and polycrystalline specimens with well determined crystal structures and known lattice parameters.

2.2 Deposition of samples

Samples were prepared by Multi-Arc (UK) using thin wafers of Ti(6%Al, 4%V) or silicon as substrates. The surface for coating was about $16cm^2$ and the thickness about 0.7cm for the metal substrates. The metal substrates were degreased and polished prior to being placed in the chamber.

A copper block was designed on which the substrates could be mounted at three different angles of orientation, namely with the substrate surface parallel, at 45° and perpendicular to the cathode surface. This block had the advantage that the three samples could be made in the same cycle, thereby keeping all parameters apart from the orientation constant. Another advantage of using the copper block was that its large thermal mass helped to keep the temperature of the thin substrates constant during the deposition. Figure 2.1 is a schematic diagram of the block showing the geometry of the substrates to the cathode. The axis of rotation of the copper block is also shown in figure 2.1. In practice, components are usually coated in double rotation on the planetary i.e., the

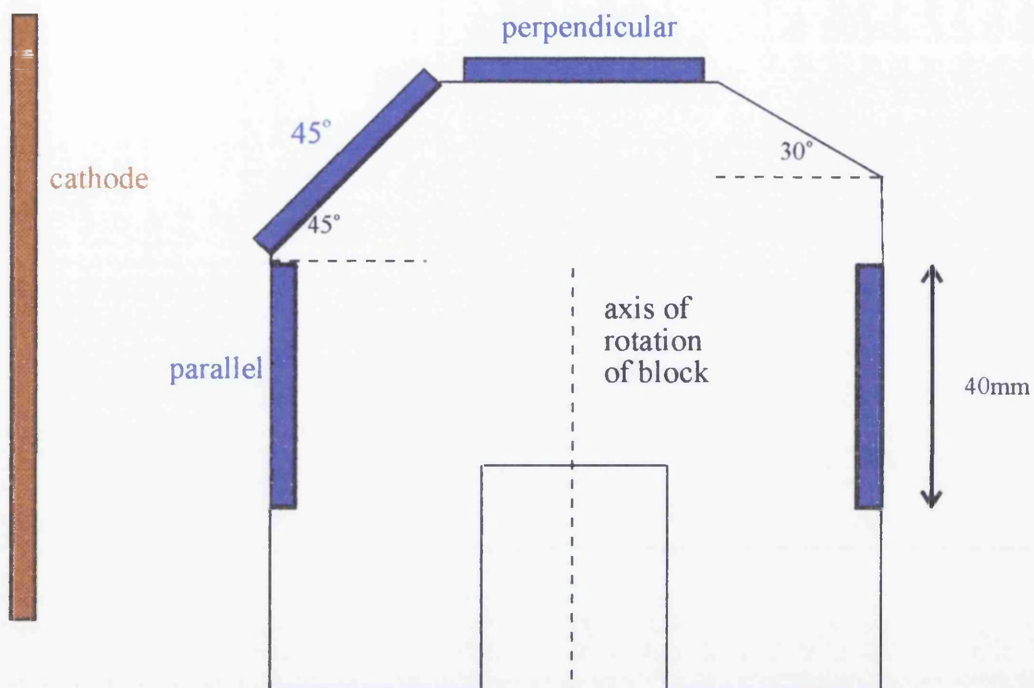

Figure 2.1 *Schematic cross-section of copper block for deposition at different orientations.*
Positioning and terminology of substrates used in this thesis are shown in blue.
Substrate to cathode distance and cathode size are not to scale.

components rotate around their own axis and around the axis of the centre of the chamber. During rotation the distance and orientation of the substrate surface to the cathode surface changes. In order to make it easier to establish the effect of the orientation some of the samples studied in this work were prepared with their substrates held stationary during the sputter cleaning and deposition processes.

All of the samples studied in this thesis were sputter cleaned with either Cr or Ti ions prior to deposition of the coating. The sputter cleaning took place in vacuum and with a substrate bias of -1000V. The temperature of the substrate was measured during the processes using an infra red pyrometer.

Subsequent deposition of coating was achieved by reducing the substrate bias and introducing N_2 gas into the chamber. These changes were performed manually while monitoring the gas pressure. Substrate biases between -70V and -200V were used during the coating cycle. The partial pressure of the N_2 gas was typically 1-2Pa.

One of the parameters used in this thesis to describe the samples is the product of the cathode current and the time for which the arc was running. This parameter is measured in Amp hours and is used by Multi-Arc as a guide to the thickness of coating deposited.

2.3 Specimens

One of the prerequisites for analysis in a transmission electron microscope is the preparation of an electron transparent region of specimen. At 100kV this means a maximum thickness of about 200nm. If electron energy loss spectroscopy is to be performed then the maximum useable thickness is about 100nm. However, the specimen as a whole should be sufficiently robust to

allow transfer between the specimen holders of different microscopes. Particular care has to be taken to prepare specimens with sufficient mechanical stability when there are high levels of internal stress in the coatings as such stress can cause the specimen to distort or break during thinning.

To allow the coating to be characterised in three-dimensions, specimens were prepared in planar and cross-sectional orientations. Figures 2.2 and 2.3 are schematics of planar and cross-sectional specimens, respectively. Planar specimens were made by thinning from the substrate side to leave electron transparent regions of coating. Preparation of the cross-sectional specimens was more complex with the specimens being thinned from both sides. The full preparation techniques for these specimens are described in appendix A1.

2.4 SEM

Scanning electron microscopy was used to study the surface morphologies of the samples. A Hitachi S800 SEM (scanning electron microscope) and a Philips 515 SEM were used for this purpose. The SEMs gave images of the surface at modest magnifications (up to ~20k) allowing qualitative structural analysis of the surface. These images were obtained using secondary electrons.

2.5 CTEM

2.5.1 CTEM bright and dark field imaging

Bright and dark field imaging were used to study the grain nucleation, growth and size in the coatings. Most of the imaging was performed using a JEOL

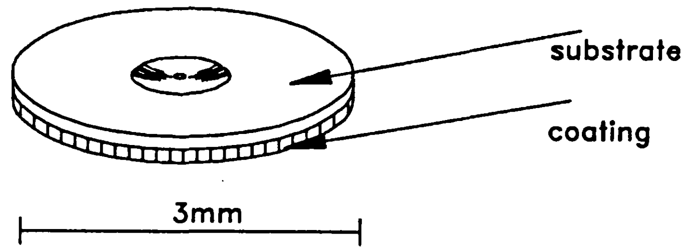

Figure 2.2 *Schematic of planar specimen.*

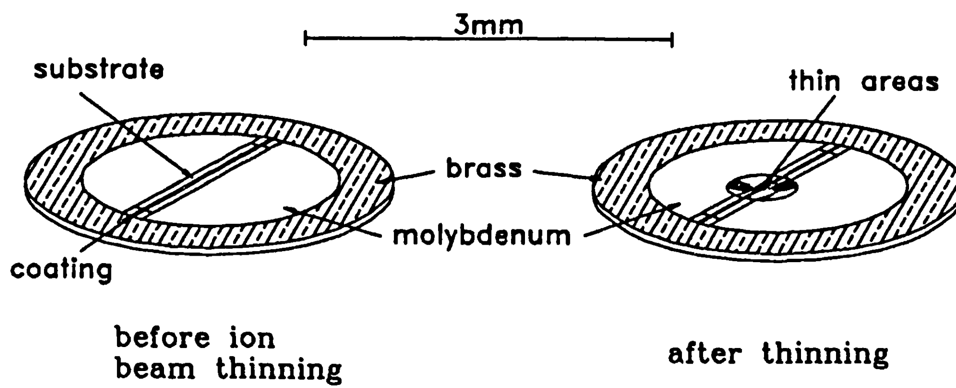

Figure 2.3 *Schematic of cross-sectional specimen.*

1200 CTEM operated either at 120kV or 100kV. A JEOL 2000 CTEM operated at 200kV was also used for some image studies.

Standard bright field imaging was performed with an objective aperture positioned on the optic axis of the microscope to remove all scattered electrons from the image and give enhanced contrast in the image. Dark field imaging was performed by tilting a bright spot or arc in the selected area diffraction pattern onto the optic axis of the microscope. The smallest objective aperture was then inserted on the optic axis to prevent other reflections from contributing to the image. Using this technique particular orientations in the specimen were highlighted. Dark field imaging uses only electrons which have been scattered in a small range of directions. Therefore, it is a much less efficient use of electrons and the intensity of the image is usually reduced but there is greater contrast in the image.

The method employed when imaging cross-sections in the microscope was to tilt the specimen until the contrast at the interface was maximised.

2.5.2 CTEM diffraction techniques

Diffraction techniques were used to identify phases present in the specimens by indexing diffraction patterns and measuring the lattice parameters. Diffraction was also used to look for preferred orientations e.g. texturing and for relationships between orientations of grains in the substrate and coating.

Selected area diffraction was performed by placing a selected area aperture in an imaging plane conjugate to the specimen. However, the spatial resolution was low and diffraction information could only be obtained from relatively large areas of the specimen since the smallest selected area aperture on the JEOL 1200 had a diameter equivalent to ~450nm at the image. To obtain higher spatial resolution, microdiffraction was used. This technique involved focusing the beam down to a small spot or probe on the sample in imaging

mode. The resulting diffraction pattern was thus obtained from a much smaller region of specimen, typically 70nm in diameter in the JEOL 1200. However, although the spatial resolution was increased the angular resolution was reduced, because of the increased convergence of the illumination.

2.6 The extended VG HB5 STEM

The Glasgow VG HB5 which operates at 100kV has been modified by the addition of three post specimen lenses and a z-lift stage (Craven & Buggy, 1981).

The imaging in this microscope was done mainly using an annular dark field (ADF) detector. STEM annular dark field imaging differs from CTEM dark field imaging in that an ADF detector collects a large fraction of the angular range of the electrons scattered outside the central beam resulting in a much more efficient use of electrons. The resulting contrast is therefore lower but all phases and orientations are imaged. Most of the work done on this microscope was microanalysis consisting of EELS and EDX microscopy. Imaging was used to identify regions of interest and to record the regions of specimen from which microanalytical data had been taken.

Microanalysis requires high spatial and energy resolution which necessitates a small probe with a high intensity of electrons i.e., a high brightness. It has been demonstrated that at 100kV a field emission source gives the highest brightness and hence the largest current in a small spot (Crewe, 1971). The field emission gun (FEG) on the HB5 consists of a single crystal of tungsten with a very sharp point supported on a tungsten wire. The application of typically 4kV to this point gives a potential difference of several V/Å resulting in a field emitted current. Due to a build up of gas on this tip increasing its work function, the electron emission decreases with time and it is necessary to 'flash' the tip about

every twenty minutes. This is done by briefly passing a high current through its support wire to remove the contaminants. The FEG requires an operating vacuum of the order of 10^{-11}mbar to prevent production of ions which could damage the tip. The rest of the column which has an operating vacuum of about 10^{-8}mbar is separated from the gun by a differential pumping aperture.

Figure 2.4 shows the main components of the HB5. The rays indicated are those of the bright field cone when the microscope is set-up for EELS. The components shown in dashed lines are not in use in this mode. A virtual objective aperture (VOA) defines the angular convergence of the probe. The size of the probe, which is the factor limiting spatial resolution, is determined by the condenser and objective lenses. There are two condenser lenses on the HB5 allowing greater flexibility in probe size and convergence. However, for this work only condenser lens one was used as it gives the higher current. The condenser lens is focused to form an image of the electron source in the plane of the selected area aperture (SAA); stray electrons are thus removed by the SAA. The probe is transferred to the specimen by the objective lens field and can either be held stationary on the specimen or scanned across it in a raster by the scan coils. The magnification of the image is determined by the area of specimen being scanned.

The image is focused by adjusting the height of the specimen with the z-lift mechanism and only adjusting the objective lens current slightly to finely tune the focus. The use of the z-lift mechanism allows the microscope to be operated with an essentially standard objective lens setting. This gives a fixed post-specimen field and therefore a fixed angular compression.

The three post-specimen lenses (PSLs) allow flexibility in the range of angles reaching the detectors. These three lenses can be used independently or combined. PSL1 gives the greatest angular compression and therefore, the largest EELS signal, thus it was used for the collection of EELS data. The large angular compression means that the resultant contrast in the image is scattering contrast which highlights differences in atomic number. PSL 2 and 3

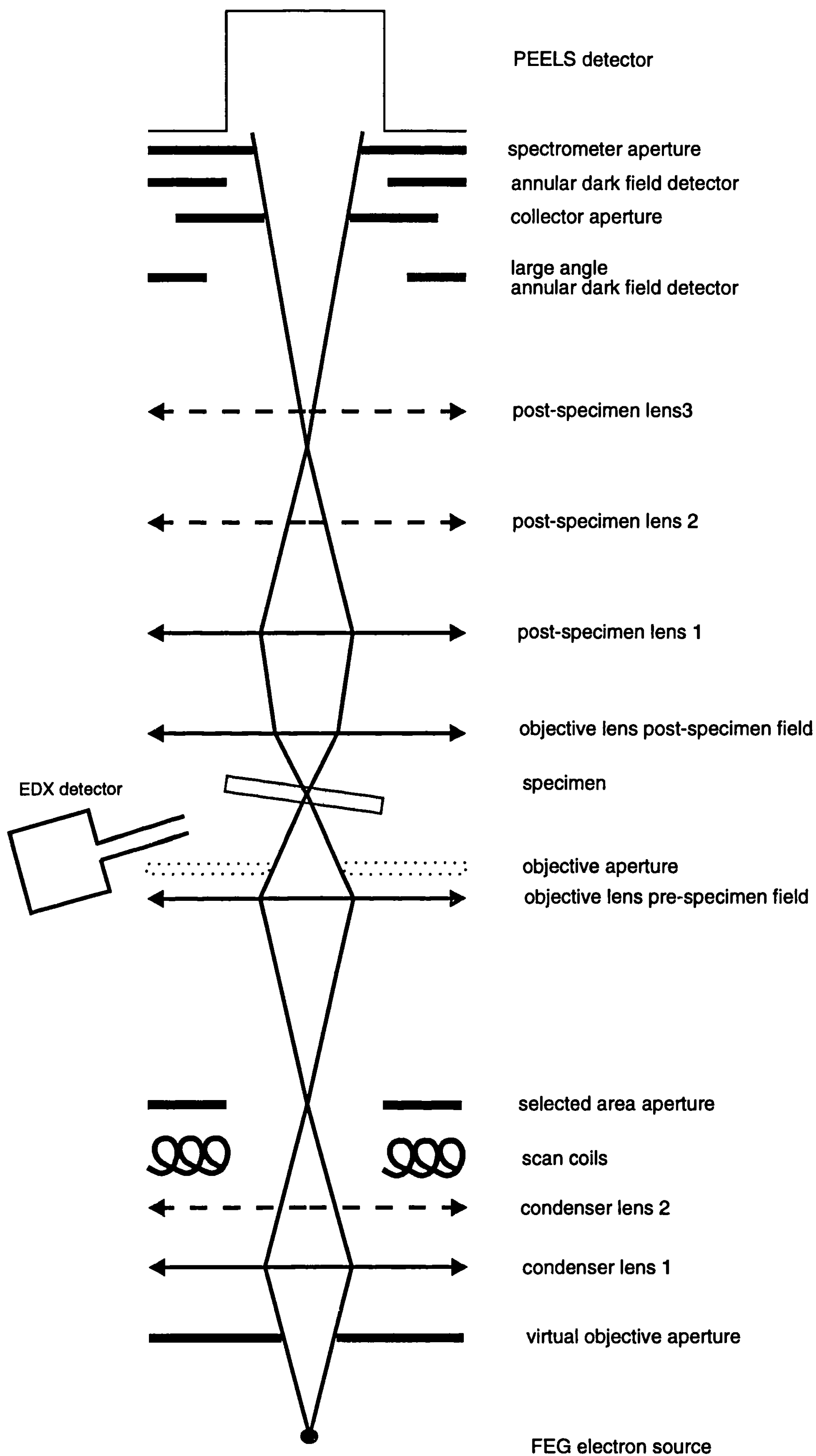

Figure 2.4 *Electron optics of the VG HB5 STEM as aligned for collection of EELS data.*
Apertures and lenses shown as dashed lines are not in use.

compress the electrons less so that the contrast in the image is diffraction contrast. The images obtained with PSL 2 or 3 were used for imaging because they accentuate differences in phase or orientation. More contrast in ADF images from the graded composition interface regions was thus obtained using PSL 2 or 3 rather than 1 at their respective standard settings.

The HB5 is fitted with several detectors. The position of the detectors of interest in this thesis are shown in figure 2.4.

There are three annular dark field detectors and a bright field detector on the HB5. Two of the ADF detectors are interchangeable with the bright field detector; the third is a large angle ADF detector situated lower down the column which can be used in conjunction with one of the other detectors. The ADF detectors are electron detectors in the form of annular scintillators which emit photons on being hit by an electron. These are detected by a photomultiplier tube, amplified and passed to two cathode ray tubes which synchronously display the image allowing simultaneous imaging with the large angle ADF detector and one of the three interchangeable detectors. Electrons which have been scattered through solid angles less than that subtended by the ADF detector pass through the annulus and can be detected by the Gatan PEELS (parallel electron energy loss spectroscopy) spectrometer. The PEELS spectrometer is described in section 2.7.1. The collection semi-angles of the interchangeable ADF detectors are 25mrad and 50mrad, so a smaller aperture is usually used to define the collection angle of the PEELS spectrometer. A spectrometer aperture (SpA), situated between the collector aperture and the entrance aperture of the PEELS spectrometer, was originally used for this purpose but spurious scattering was found in the spectra. To remove this scattering a collector aperture (CA) is normally used as the defining aperture with the spectrometer aperture acting as a spray aperture to intercept stray electrons. Some material was trimmed from the edge of the collector aperture blade so that ADF images can still be acquired even with the collector aperture on axis.

There is also a Link EDX detector on the HB5. The key features of this detector are given in section 2.8.1.

2.7 EELS

2.7.1 The EELS spectrometer

A GATAN model 666 parallel-detection electron energy loss spectrometer was used to collect electron energy loss spectra. The main components of the spectrometer are shown in figure 2.5. Electrons enter the spectrometer through the entrance aperture. The spectrum is focussed with two quadrupole and two sextupole lenses. A magnetic sector disperses the electrons into an energy spectrum. The dispersion of the spectrum is increased by four quadrupole lenses and projected onto a single crystal yttrium aluminium garnet (YAG) scintillator. The scintillator is coupled to a linear photodiode array consisting of 1024 channels. This array enables parallel detection i.e., the simultaneous collection of electrons which have lost different amounts of energy. The electrically isolated drift tube allows the energy offset of the spectrum to be varied by applying a voltage to it. The final energy dispersion of the spectrum is determined by the four quadrupole lenses which can be varied to give a range of dispersion settings from 0.05 to 2.0eV per channel with a 100kV electron microscope.

The next section describes the HB5 as it was aligned for the collection of EELS data.

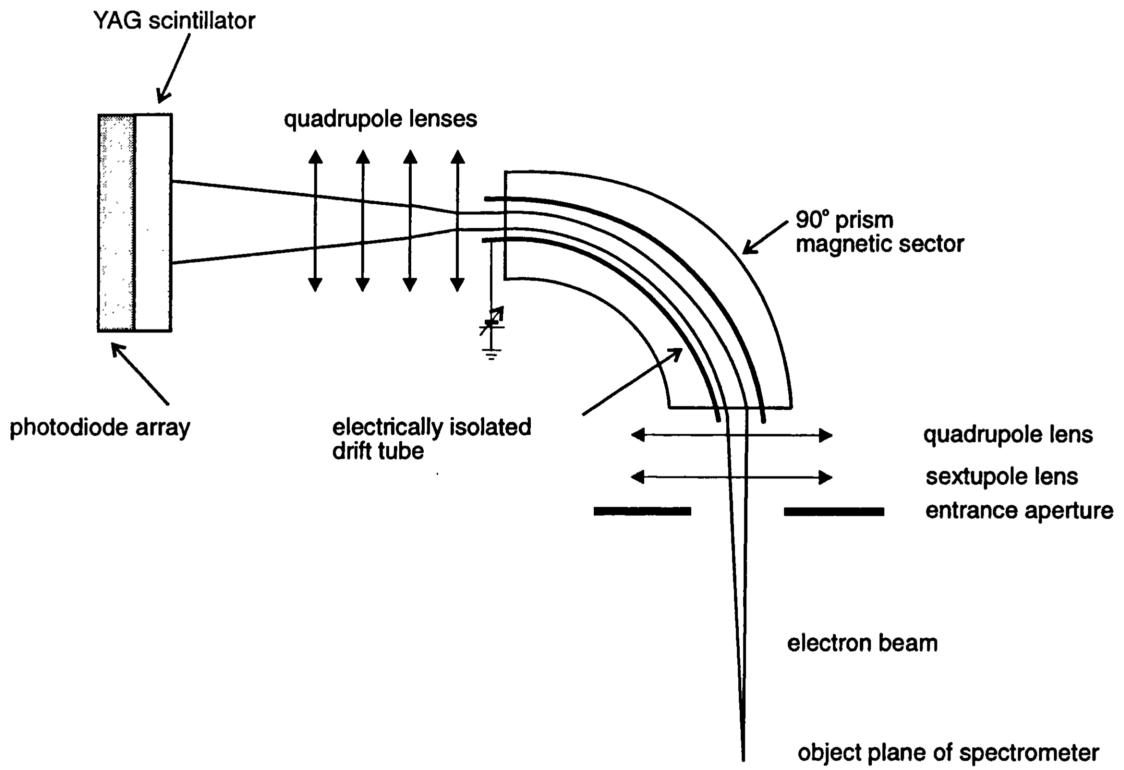

Figure 2.5 *Schematic of EELS detector.*

2.7.2 EELS - microscope conditions

Figure 2.4 shows the HB5 as it was aligned to collect EELS data. This alignment is achieved as follows.

The axis of the lower column of the microscope was defined by centring the objective aperture with the PSLs off. This was done by wobbling the objective lens current and mechanically shifting the aperture until the image became stationary and just pulsed in and out of focus. The condenser lens wobble was also checked and adjusted if necessary. The objective aperture was then removed and a VOA positioned on the defined optic axis. An SA aperture was inserted. Electrical shifts were used to position the beam on the spectrometer axis. The collector aperture was inserted on axis. The individual PSLs were then mechanically aligned to this axis.

PSL 1 was used to give an angular compression of 10, thus increasing the signal and reducing the collection time accordingly. The data presented in this thesis was collected using either a 1mm collector aperture to define the collection angle with a 1.25mm spectrometer aperture as a spray aperture or using a 0.75mm spectrometer aperture as the defining aperture. With PSL 1 at its standard setting these set-ups gave collection semi-angles of 12.5 and 7.5mrad respectively.

Either the 70μm or 100μm VOA were used to define the probe giving convergence semi-angles of 8 and 11mrad respectively.

2.7.3 EELS - set-up and collection of data

Photodiode arrays give their optimum performance just below their saturation level as the signal to noise ratio is at its maximum at this point. However, the response of the photodiode array used to collect the spectra is non-linear above

10 000 counts and it saturates at 16 000. Therefore, during collection of data care was taken to ensure collection of a sufficiently high level of signal to enable quantification of the edges while ensuring that the counts did not go above 10 000 in a single acquisition. Prior to collection of data, the photodiode array was flooded for about 10 minutes to equalise the charge distribution in the YAG scintillator. This was done by removing all apertures from the beam apart from the 250μm VOA and using the 0eV energy dispersion setting on the PEELS spectrometer which uniformly spreads the illumination over the whole active area of the scintillator.

After flooding the diode array and re-inserting all the relevant apertures on axis the EELS spectrum was finely focused by minimising the width of the zero loss peak (see section 3.2.1). The focusing provided a useful check on the alignment of the microscope; only a fine trim should be required because of the essentially standard optical conditions. The energy dispersion of the spectrum was then calibrated using an automated routine provided in the Gatan software. The zero loss peak was positioned about channel 100.

An edge spectrum and a low-loss spectrum (see section 3.2.1) were collected at each point analysed before moving the probe. The low-loss region is required in the subsequent analysis of the data and can be used to measure the thickness of the specimen.

The number of counts in the zero loss peak is typically 2 orders of magnitude higher than the counts in edge spectra. Therefore, to optimise the counts in both low-loss and edge spectra, a beam blanking system which reduced the number of counts reaching the spectrometer, was used in the collection of the low-loss signals thus removing the need for changing the microscope conditions. Low-loss spectra were usually acquired by summing 100 acquisitions, each with an integration time of 0.04s during which the beam was unblanked for about 0.001s. The edge spectra were typically acquired with integration times of 4s. Spectra were collected with the same acquisition parameters as the low-loss and edge spectra but with no beam incident on the

detector so that the dark currents from the photodiode array could be measured for subsequent removal from the spectra.

An energy dispersion of 0.5eV per channel was used to collect most of the data and with the 1024 channel photodiode array this gave a range of ~500eV in each spectrum. A voltage scan module (VSM) was used to apply a voltage to the drift tube which changed the energy offset of the spectra. Data was collected at 0.1eV per channel for examination of fine structure.

When looking at fine structure in detail, any channel to channel fluctuations in the photodiode array become important. Such artefacts were removed from the data by using the voltage scan module to progressively shift the spectra by 5eV. The spectra were aligned and summed during processing of the data.

The edges of interest were C K, N K, Ti $L_{2,3}$, O K and Cr $L_{2,3}$. Table 2.1 lists these edges along with their energies.

Table 2.1 *EELS edges examined.*

element	edge type	edge energy, eV (Ahn & Krivanek,1983)
C	K	283.8
N	K	401.6
Ti	$L_{2,3}$	455.5, 462
O	K	532
Cr	$L_{2,3}$	574, 584

All of the edges listed in table 2.1 could be collected in a single spectrum using an energy dispersion of 0.5eV per channel and an energy offset of 300 or 350eV. The N, Ti and Cr edges were collected for quantification. Some O appeared as an impurity in many of the spectra as a result of oxidation. The C edge was collected to monitor contamination of the specimen from the electron beam.

Carbon contamination was one of the main problems encountered in the collection of EELS data. Carbon from the electron beam built up on the surface of the specimen, increased the specimen thickness and quickly rendered the specimen too thick for EELS analysis. This problem was sometimes overcome by flooding the specimen. This involved removing all the apertures and gradually reducing the area of specimen being irradiating. The electron beam pinned down the carbon fixing it in place. If the contamination was very bad the problem was sometimes solved by baking the specimen on a light bulb for about half an hour just before replacing it in the microscope. Care was taken in the specimen preparation to reduce the likelihood of carbon contamination but the problem was difficult to control. The glues used in the specimen preparation contain hydrocarbons and are therefore likely to be a source of contamination. Two different types of glue were used, and there appeared to be less problems with contamination when using Gatan G1 epoxy rather than Devcon 5 minute epoxy. Specimens were cleaned and gloves were worn in the final stages of the preparation process.

Another major problem in the collection of data was specimen drift. After mechanically moving the specimen it continued to drift for a period. The ability to obtain an ADF image with the same set-up as for collection of EELS data allowed the drift to be monitored by examining the image in scanning mode in between each point collection. In the collection of line profiles, the probe was generally held stationary on a point and stepped along a line perpendicular to the interface. Between each point the probe was returned to scanning the specimen to allow the positioning of the probe to be checked. If the drift per acquisition was less than the separation of the steps it was corrected using electrical image shifts on the microscope and the distance of drift recorded. Provided the electrical shift required was not too big, the alignment of the microscope was not significantly affected. The maximum beam movement used for this purpose was about 5% of the total length of the line profile.

For some of the line profiles in the droplet analyses in chapter 7, the probe was scanned across a small area of specimen, typically 15nm^2. The area of specimen being irradiated was selected using the electrical shifts on the microscope.

2.8 EDX

2.8.1 EDX detector

The X-ray detector on the HB5 is a Link Si(Li) detector. This detector allows detection of X-rays emanating from elements with atomic number of 10 or greater and has been described in detail elsewhere (Zaluzec, 1979). A collimator prevents off-axis high energy X-rays from entering the detector. The collimator entrance is situated in the gap of the objective lens with the mean angle between the collimator axis and the emergent electron beam being 100.5°. Hence the specimen should be tilted towards the detector for collection of data.

The efficiency of the detector is essentially uniform at 100% in the 3-15keV range (Zaluzec, 1979).

2.8.2 EDX - microscope conditions

EDX data was collected on the HB5 with the lower part of the column aligned as shown in figure 2.4.

The solid angle of X-rays detected by EDX means that the detector is likely to detect X-rays emanating from sources other than the irradiated region of specimen (Nicholson, 1994a).

Spurious signals from stray electrons are reduced by the use of a selected area aperture imaged in the plane of the specimen. This aperture is in a plane conjugate with the electron source and is at the optimum position for eliminating the vast majority of spurious electrons since they are very defocused in this plane (Craven, 1995a) whereas the electron beam is at a crossover.

The use of a virtual objective aperture before the condenser lens rather than an objective aperture in the back focal plane of the objective lens, further reduces spurious signals. The objective aperture is positioned sufficiently close to the specimen that some of the electrons scattering from the aperture blade could hit the specimen resulting in spurious X-rays.

2.8.3 EDX - collection of data

The main peaks of interest were Ti Kα,β and Cr Kα,β. Other peaks which were examined were Si Kα, Al Kα and the Hf L series. The peak energies are listed in table 2.2.

Table 2.2 *EDX peaks of interest*

element	peak	energy, keV (Bearden, 1967)
Ti	Kα	4.508
Ti	Kβ	4.931
Cr	Kα	5.411
Cr	Kβ	5.947
Si	Kα	1.740
Al	Kα	1.487
Hf	Lα	7.899

Data was typically collected for 30s with an energy dispersion of 20eV per channel. With 1024 channels this gave an energy range from zero to about 20keV in the spectra. This allowed the collection of the peaks of interest along with a window of about 5keV in the 10-15keV energy range which can be used as a measure of the specimen mass-thickness (Hall, 1971).

2.9 Imaging & X-ray mapping on the HB5

A digital image is made up of a two-dimensional array of pixels whose intensities represent some physical parameter. For electron imaging the intensity in each pixel is related to the intensity of electrons emanating from the corresponding point on the specimen being irradiated. Images were usually collected with a resolution of 256 by 256 pixels, the spatial resolution depending upon the magnification. About 100 frames were collected per image and these were averaged to increase the signal to noise ratio.

An X-ray map is an image where the intensity in the pixels represents numbers of X-rays rather than electrons. Energy windows in the X-ray spectrum may be selected and all X-rays within this energy range will contribute to the intensity in a pixel. Several windows can be mapped simultaneously, so that maps relating to the concentration of several elements can be collected. X-ray mapping is a very useful technique for obtaining information relatively quickly from a large area of sample but with relatively low resolution. X-ray maps were usually collected with a resolution of 128 by 128 pixels using typical dwell times of 1ms or 5ms per pixel and with integration over several frames to give sufficient counts.

2.10 Summary

The techniques described in this chapter provide the mechanisms for investigating the microstructure and microchemical composition of the coatings and the substrate/coating interfaces. However, in order to obtain meaningful quantitative results it is necessary to have an understanding of the fundamental processes giving rise to the EELS and EDX data. Theoretical considerations for these two processes are the subject of the next chapter along with the methods used to analyse the data.

CHAPTER 3

Theoretical Considerations and Analysis of Data

3.1 Introduction

When a beam of fast electrons are incident on a thin solid specimen, they interact electrostatically with the atoms in the specimen. These interactions can take several forms and are the basis of analytical electron microscopy. If the electrons are scattered elastically the change in their momentum is absorbed by the specimen as a whole, resulting in a large scattering angle. Such electrons lead to diffraction effects. However, electrons can also be scattered inelastically. Quasi-elastic scattering excites a vibrational mode, involving an energy in the meV range but can involve a significant momentum change leading to a large angle of scattering. This cannot be separated from the elastic scattering. There are several mechanisms by which electrons can lose energy, the most important of which are briefly outlined below.

Plasmon excitation occurs when there is a collective excitation of the valence electrons of more than one atom in the form of a charge density oscillation. This energy loss which is quantised leads to small angle scattering. As the scattering angle increases, the volume of excitation decreases until eventually it becomes a single electron excitation.

Single electron excitation occurs when the energy of the incident electron is sufficient to eject a single bound electron. If this electron comes from a shell with sufficient binding energy, the atom de-excites with the emission of either an X-ray or an Auger electron. The scattering angle, θ is small at low energy losses with θ varying as $E/2E_0$ where E is the energy lost and E_0 is the incident energy. The electron can either be a core or a valence electron.

Bremsstrahlung X-rays are produced when the incident electrons are accelerated in the field of the atomic nuclei resulting in loss of energy by the electrons.

By measuring the energy loss of the transmitted electrons and/or the energies of the emitted X-rays, we can obtain information on the chemical composition of the specimen. In order to quantify this, it is important to have some understanding of both the scattering events which give rise to these events and the probability with which they occur.

3.2 EELS

3.2.1 Theoretical considerations for EELS

'Electron energy loss spectroscopy in the electron microscope' by Egerton (1986) is a good introduction to the subject. The key points relevant to this thesis are summarised below.

In electron energy loss spectroscopy, the energy lost by inelastically scattered electrons is measured and utilised to provide information on the chemical composition of the specimen irradiated by the electron beam. If an incident electron ejects an electron from an inner shell to the continuum, then this will

result in an ionisation edge in the energy loss spectrum. The edge onset or threshold is at the binding energy for that shell. Therefore, the edges are characteristic of the material being irradiated and can be used to determine the chemical composition. Excitation of electrons to empty valence states rather than to the continuum, results in peaks superimposed on the edge.

A typical energy loss spectrum is shown in figure 3.1. The energy loss spectrum contains a large zero loss peak resulting from electrons which have not lost energy or have lost less than the resolution of the system. The next most intense feature is the first plasmon peak where electrons have lost energy via plasmon excitations. The region containing the zero loss and the valence excitations is called the low-loss region. Characteristic edges are superimposed on the background which falls off monotonically as E^{-r}. These ionisation edges contain fine structure which can be split into two regions, namely near edge fine structure (ELNES) which is within 50eV of the edge threshold and extended edge fine structure (EXELES) which can extend for several hundreds of eV beyond the edge. Multiple scattering can also occur leading to a redistribution of the energy spectrum. The probability of an electron experiencing two plasmon or two core excitations is low, however, the probability of a core and a plasmon excitation occurring increases as the thickness of the specimen increases.

On the assumption that scattering events are independent then their occurrence should obey Poisson statistics. The probability, P_n of n successive collisions is given by

$$P_n = \left(\frac{1}{n!}\right)\left(\frac{t}{\lambda_T}\right)^n \exp\left(-\frac{t}{\lambda_T}\right) \tag{3.1}$$

where t is the specimen thickness and λ_T is the total mean free path which is given by

$$\frac{1}{\lambda_T} = \sum_i \frac{1}{\lambda_i} \tag{3.2}$$

where λ_i is the mean free path for each collision.

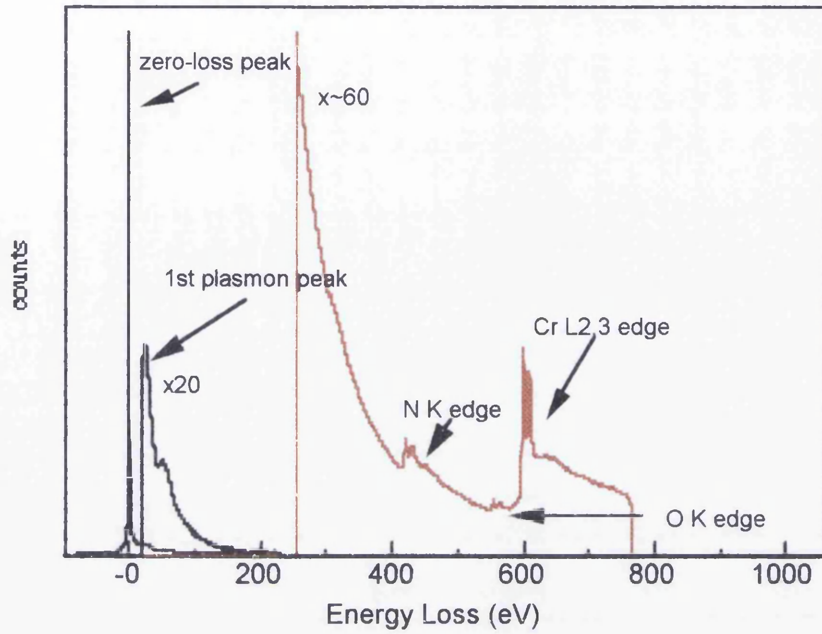

Figure 3.1 *Electron energy loss spectrum.*

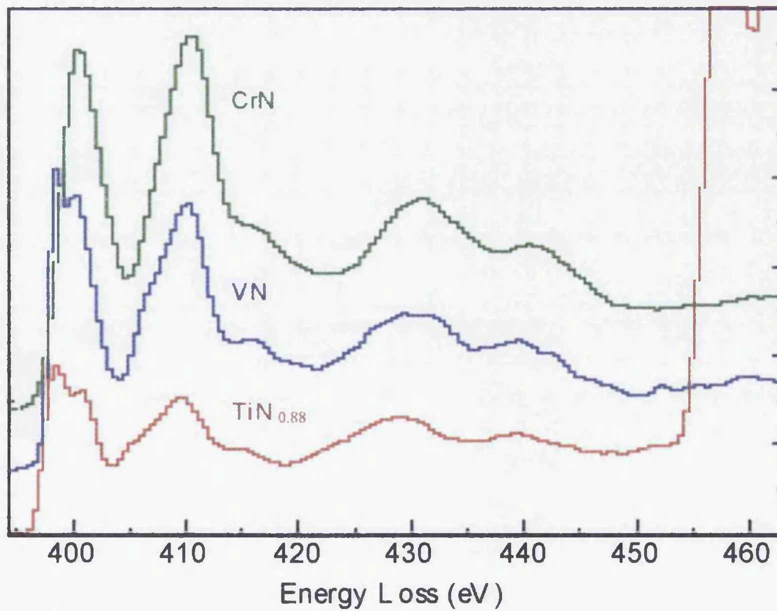

Figure 3.2 *N K edge in CrN, VN and $TiN_{0.88}$ standards.*

The probability, P_k of an electron exciting an inner shell electron of the element giving rise to an edge, k is given by

$$P_k = \left(\frac{t}{\lambda_k}\right)\exp\left(-\frac{t}{\lambda_k}\right) = N\sigma_k \exp(-N\sigma_k) \qquad (3.3)$$

where λ_k is the mean free path for ionisation of the shell k, N is the number of atoms of type giving rise to the edge per unit area and σ_k is the ionisation cross-section per atom for the k shell (Egerton, 1986).

The total core-loss intensity, I_k of the edge k (excluding the background) is given by

$$I_k = P_k I \qquad (3.4)$$

where I is the total transmitted intensity.

Because λ_k is several orders of magnitude bigger than t equations 3.3 and 3.4 can be combined to give

$$I_k = N\sigma_k I \qquad (3.5)$$

For thin specimens the effects of backscattering and absorption are negligible so I is equal to the incident beam current. In practice, the electrons passing through the specimen may undergo multiple scattering events, making interpretation of the energy loss spectrum more difficult and resulting in loss of accuracy.

Equation 3.5 can be used to find N but it is more usual to obtain N via use of the following relationship, namely

$$I_k(\Delta,\alpha,\beta) = N\sigma_k(\Delta,\alpha,\beta)I_o \qquad (3.6)$$

where $I_k(\Delta,\alpha,\beta)$ is the intensity in a window of energy width Δ (excluding the background), I_o is the intensity in the zero loss peak and $\sigma_k(\Delta,\alpha,\beta)$ is the partial cross-section for the window Δ. The intensity in the window and the partial cross-section are functions of the convergence and collection semi-angles, α and β. This is because the presence of the collector aperture only allows electrons into the spectrometer which have been scattered through an angle less

than β. Equation 3.6 is more useful for quantitative analysis than equation 3.5 because the presence of more than one edge in the spectrum constrains the size of the integration window. Extrapolation errors in the removal of background intensity will be reduced if the size of the integration window is limited.

However, in this thesis it is the atomic ratios that are of interest rather than the absolute number of atoms of a particular element in the specimen. The atomic ratio of two elements, a and b may be calculated via the following relationship, derived from equation 3.6

$$\frac{N_a}{N_b} = \frac{I_{ka}(\Delta_a,\alpha,\beta)\sigma_{ka}(\Delta_a,\alpha,\beta)}{I_{kb}(\Delta_a,\alpha,\beta)\sigma_{kb}(\Delta_b,\alpha,\beta)} \tag{3.7}$$

The energy loss spectrum can also be used to measure the thickness of the specimen. For independent scattering events within a foil, the probability of several successive collisions of an electron occurring is given by a Poisson distribution. The zero loss intensity, I_o is given by

$$I_0 = I_t \exp\left(-\frac{t}{\lambda_T}\right) \tag{3.8}$$

where I_t is the total intensity reaching the spectrometer, so if λ_T is known for the specimen, then the thickness can be calculated. If λ_T is not known then the relative thicknesses may still be calculated.

As the sample thickness increases the peak to background ratio falls rapidly making it difficult to distinguish edges. However, if the specimen is too thin then there is very little scattering and the signal to noise ratio is low. At 100keV the optimum thickness is a few 10's of nanometres (Egerton, 1986).

3.2.2 Analysis of EELS data

Analysis of the EELS data was performed using the EL/P versions 2.1 and 3.0 software provided by Gatan. This software facilitates various operations which

may be performed on the spectra to aid quantitative analysis. The 'process' menu provides generic mathematical tools and the 'analyze' menu contains routines which allow the extraction of physical data about the specimen from the EELS spectra. The main physical data required in this work are the relative specimen thicknesses and the relative concentrations of the elements present. All of the spectra were analysed in a similar way to allow comparisons to be made between different data sets. The method of analysis is described below.

The dark currents were removed from the spectra and the energy scales were calibrated by setting the channel in the low-loss spectrum with the maximum number of counts equal to 0eV. The same channel in the corresponding edge spectrum was set to the value of the energy offset applied by the VSM during acquisition. Removal of the dark current from the low-loss spectrum often resulted in channels containing no information or negative counts and it was necessary to set such channels to zero. This process will be referred to as tidying. The EL/P 'compute thickness' routine was applied to the low-loss spectrum to calculate the t/λ value. The background before the first edge of interest in the edge spectrum was stripped off using the background fit provided by EL/P. The resulting spectrum was tidied before the edge onset and at the end where the data began to roll off. It was found that it was necessary to set the channels prior to the edge onset to 1, to allow the next stage of the processing to work satisfactorily so a single count was added to each channel. The plural scattering was then removed from the edge spectrum using the 'Fourier-Ratio' routine. This routine required the input of the isolated edge spectrum (i.e. one with the background subtracted and tidied) and the corresponding low-loss spectrum. The low-loss spectrum is deconvoluted from the edge spectrum to remove the plural scattering.

The instrumental broadening introduced by the detector can make background fitting difficult because of the smearing effect it has on the edge onset. This effect was removed from the spectrum in a process called sharpening. This routine required the input of two spectra, namely an edge spectrum and a zero-loss peak. The zero-loss peak was obtained by collecting a low-loss spectrum

through a hole or by extracting it from the low-loss spectrum using the compute thickness routine.

The edges were then quantified by integrating the counts in each edge over a window of width Δ after the background was removed. The removal of the plural scattering gave greater flexibility in choosing the windows because different positions relative to the edge onset and different values of Δ could be used for different edges. Equation 3.5 was used to calculate the atomic ratios. Equation 3.5 also requires that the partial cross-sections are known. The partial cross-sections used for quantification of the N K, Cr $L_{2,3}$ and Ti $L_{2,3}$ edges were obtained from standard CrN, Cr_2N and $TiN_{0.88}$ specimens. The calculation of these partial cross-sections and the reason for using standards are dealt with in section 3.2.3.

As can be seen from table 2.1 in chapter 2, some of the edges of interest were quite close in energy. This made background fitting difficult due to the fine structure, and in some cases, the background fit routine in EL/P did not work. This is because the routine fitted a power law function of the form

$$AE^{-r} \tag{3.9}$$

where A and r are parameters determined by the routine. However, if this function was not a reasonable fit to the shape of the background then the model was deemed invalid and EL/P did not remove the background. The presence of the O K edge before the Cr $L_{2,3}$ was not in general a problem. This was because O was usually only present when there was a large Cr (or Ti) peak and the intensity of the O peak was small compared to the metal peak. The proximity of the N and Ti edges proved far more problematical. The routine generally failed to fit a background before the Ti edge in the presence of N because equation 3.9 was a very poor description of the shape of the background spectrum in this region.

It was decided to remove the background from the Ti edge by matching the N edge in a CrN standard specimen to the N edge in the spectrum of interest, because the background appears to be a much better fit than that generally

provided by EL/P and because EL/P occasionally failed to fit a background. It is known that the nitrogen and carbon edges in transition metal nitrides and carbides have very similar shapes (Craven, 1995b). Figure 3.2 shows the N K edge in three metal nitride standards, namely $TiN_{0.88}$, VN and CrN. The energy dispersions used to collect the three spectra were different so for ease of comparison all three were scaled to the same energy dispersion and the edges were aligned. The spectra were processed as described above but because they were collected with a higher energy dispersion, a 0.5eV smoothing filter was applied to them. The $TiN_{0.88}$ and VN spectra were collected and processed by Craven. From figure 3.2 it can be seen that the overall shape of the edges is similar but the separation of the peaks in the ELNES in each edge increases as the lattice parameter decreases. These separations have been predicted to vary inversely with the square of the distance to the shell, R with

$$\left(E_r - \overline{V}\right)R^2 = constant \qquad (3.10)$$

where $\overline{V}$ is the muffin tin potential and E_r is the energy of the peak relative to the edge threshold (Natoli, 1983). Kurata et al (1993) showed that such a relationship holds approximately for ELNES. Craven (1995b) suggested that in the case of compounds with the same crystal structure, R might be replaced with the lattice parameter, a, but with a different value of constant for each shell. Craven also plotted the separation of the first and sixth peaks in the ELNES as a function of $1/a^2$ for some of the transition metal nitrides. The data fitted to a straight line of equation

$$y=0.977x-0.0242 \qquad (3.11)$$

The variation of the separation with lattice parameter can be seen in figure 3.2 where the N peaks in the CrN and VN, which have very similar lattice parameters of 4.149Å and 4.139Å respectively (Goldschmidt, 1967), have very similar separations of peaks whereas the N edge in the $TiN_{0.88}$ spectrum is more compact. The lattice parameter of TiN is 4.244Å (Goldschmidt, 1967).

The spectra from the standards were interpolated to allow for the differences in lattice parameters using equation 3.11. The N edges in the spectra were aligned to take into account the chemical shift in the edge onsets and the counts in the

spectra were matched in a 25eV window from 422eV. This window was chosen because it is just before the Ti edge onset i.e., in the position where the background should be matched. The interpolated N edges are shown in figure 3.3. Figure 3.4 shows the N edge in a CrN spectrum being used to remove the background from a Ti edge in the presence of N. The resulting stripped edge is also shown. From figures 3.3 and 3.4 it can be seen that the N edge in the CrN spectrum is not a perfect fit. However, as the concentration of Ti drops and the error caused by a poor fit increases, the fit improves.

The effects of deconvolution of low-loss and sharpening (deconvolution of broadening by the detector) were investigated. For specimens with a thickness of less than ~$0.5t/\lambda$, deconvoluting for thickness and instrument resolution had little effect on the atomic ratios obtained. However, for thicker samples deconvoluting resulted in more consistent results and sharpening made the background fitting easier. Deconvolution also gave more flexibility in the positioning and size of the integration windows used. (If the data had not been deconvoluted then the same integration window relative to edge threshold would have had to have been used for each edge to allow for plasmon scattering.)

3.2.3 Calculation of partial cross-sections for EELS analysis

In the calculation of chemical composition it is necessary to use ionisation cross-sections as described in sections 3.2.1 and 3.2.3. The Gatan EL/P software used to collect and analyse the EELS spectra will calculate such partial cross-sections for the user. The parameters which influence the partial cross-section are edge onset position, collection angle, convergence angle, incident electron energy, size and position of the integration window and the model used for the calculation. EL/P allows the user to choose the model and input the other parameters.

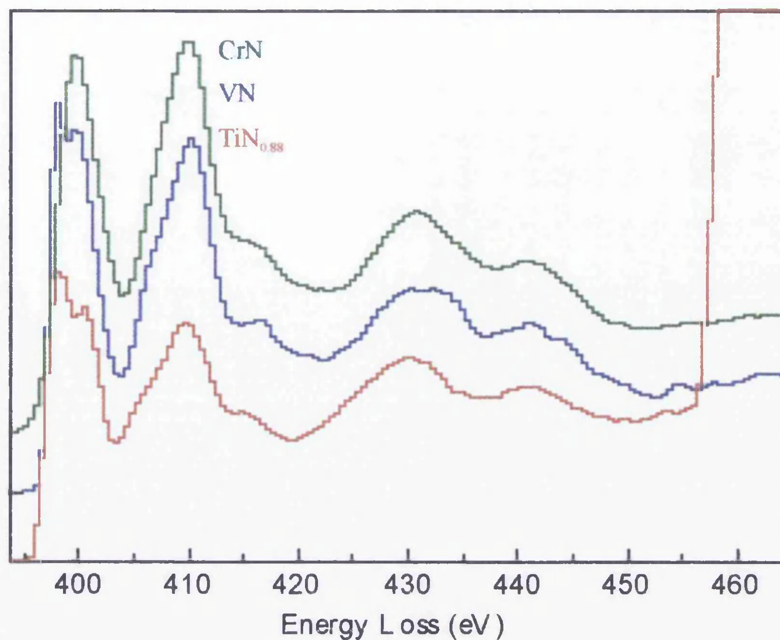

Figure 3.3 *N K edge in CrN, VN and $TiN_{0.88}$ standards interpolated for lattice parameters.*

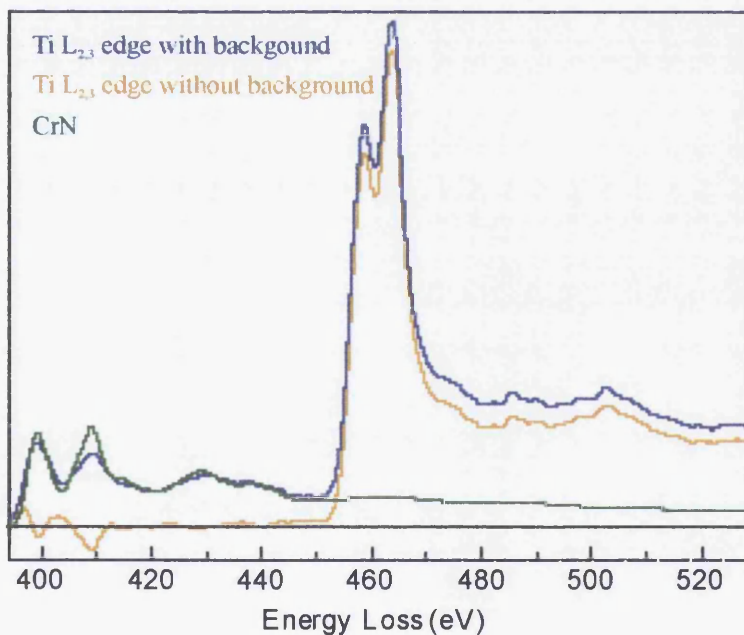

Figure 3.4 *N K edge in CrN standard being used to remove background from Ti $L_{2,3}$ edge.*

EL/P 2.1 calculates the partial cross-sections using a Hydrogenic model. The routines used are modified versions of Egerton's SIGMAK2 and SIGMAL2 routines which calculate the atomic cross-sections for ionisations of the K and L shells respectively. The absolute error on these cross-sections is 10%. The K edge cross-section is calculated theoretically from first principles. However, the L shell cross-section calculation gives the option of inputting a semi-empirical parameter which Egerton tabulates within SIGMAL2. This parameter takes account of the 'white lines' - the sharp peaks at the ionisation edge onset present in transition metal edges such as Ti $L_{2,3}$ and Cr $L_{2,3}$. The prominence of these peaks is accounted for by the dipole selection rule $\Delta l=\pm 1$, resulting in transitions from the 2p valence shell to the 3d shell just above the Fermi level. These are not considered by the theoretical atomic model as it neglects excitation to bound states e.g., the empty d-states in the transition metals (Egerton, 1986). These atomic levels form a narrow energy band with a high density of vacant d states resulting in strong peaks at the edge threshold. There are two of these white lines because spin-orbit splitting causes a difference in the binding energy of the L_2 and L_3 shells (Egerton, 1986).

EL/P 3.0 allows the cross-sections to be calculated using the Hartee-Slater model as well as the Hydrogenic model of Egerton. This model is atomic and therefore, does not take the effect of nearby atoms on the wavefunctions into account. The generalised oscillator strengths and cross-sections for the K, L and M edges calculated by P. Rez are used by EL/P 3.0 in these calculations. The Hartree-Slater model should calculate more accurate cross-sections for the L and M shells. However, it ignores excitation to discrete bound states and therefore does not take the white lines into account. The computations do not take spin-orbit splitting into account either, which in the case of Cr is considerable at 9eV. Instead the L_2 edge is shifted +9eV relative to the L_3 edge and the intensities weighted 2:1 (this is a theoretical weighting from multiplicity). Therefore, it is anticipated that the Hartree-Slater model will calculate more accurate cross-sections in the region of the edge away from the white lines but less accurate ones at the edge threshold. The problems with the

Cr white lines in particular are highlighted in the literature (Leapman et al, 1980).

The cross-sections calculated by EL/P using the Hydrogenic model with and without the white line correction and using the Hartree-Slater model were compared for the N K edge and the Ti $L_{2,3}$ and Cr $L_{2,3}$ edges to see how well they modelled the experimental data. Figures 3.5 to 3.7 show the respective edges along with the cross-sections calculated by EL/P. In the case of the N edge, both models give very similar cross-sections. For the Ti and Cr edges, the three models give very different results in the first 30eV. The Hydrogenic model with the white line correction gives the closest shape to the experimental edge, followed by the Hartree-Slater model. The absolute values of the Hydrogenic (with white line correction) and the Hartree-Slater cross-sections in the first 30eV differ by a factor of 16% and 11% for the Ti and Cr edges respectively.

To investigate the consistency of the atomic ratios obtained using these cross-sections, a series of spectra were collected from the same region of specimen using different convergence and collection angles. The atomic ratios were calculated from each spectrum using combinations of the integration windows defined in table 3.1. The windows were chosen to represent feasible windows for analysis and so that the contribution of the white lines was changed. The partial cross-sections used were obtained from EL/P 3.0 using the Hartree-Slater model and the Hydrogenic model with white line corrections. The atomic ratios are shown in table 3.2. Figure 3.8 presents this data graphically for the integration windows in table 3.1. The trends obtained with the two other combinations of integration windows are very similar. It can be seen that a difference of up to 25% may be obtained using the two different models. Using a convergence angle of 11mrad and changing the collection angle from 7.5 to 12.5mrad results in up to 7% difference in the Hartree-Slater model and 10% for the Hydrogenic. If an 8mrad convergence angle is used then the differences are larger at 15% and 16%. The differences obtained by changing the collection angle are similar. Overall, the absolute value of the ratio can

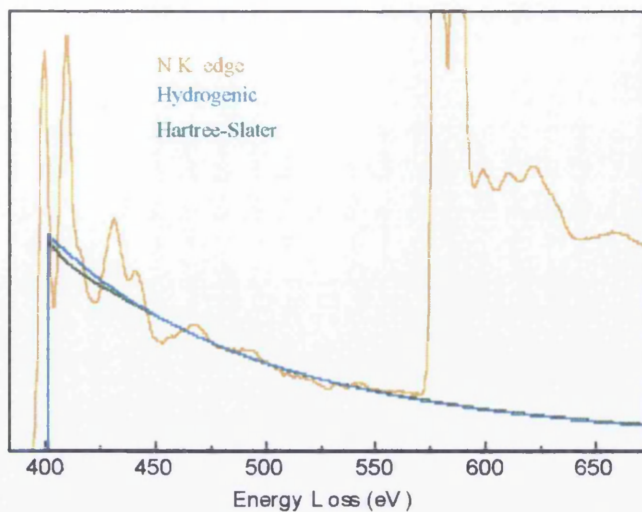

Figure 3.5 *N K edge and cross-sections calculated by EL/P.*

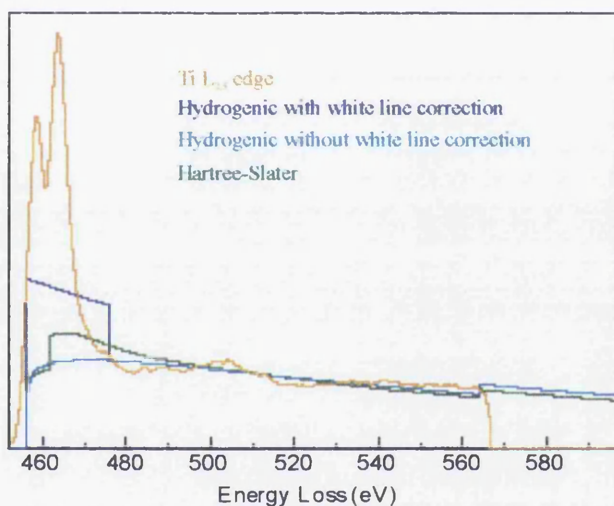

Figure 3.6 *Ti $L_{2,3}$ edge and cross-sections calculated by EL/P.*

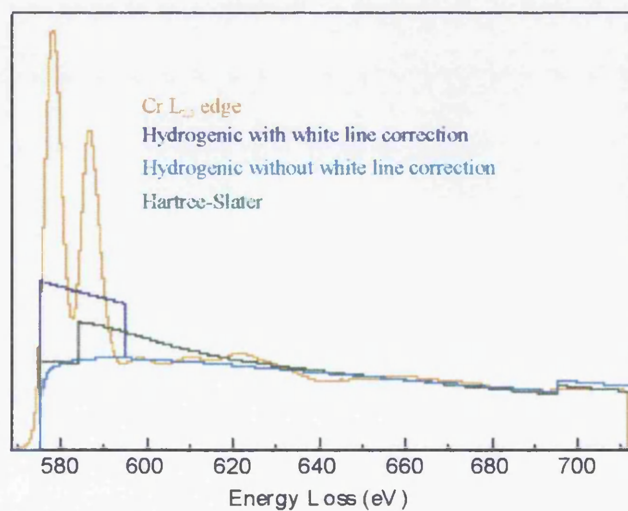

Figure 3.7 *Cr $L_{2,3}$ edge and cross-sections calculated by EL/P.*

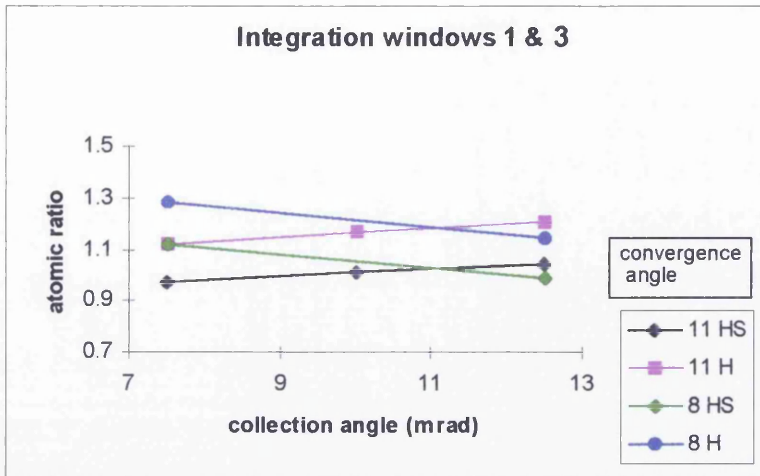

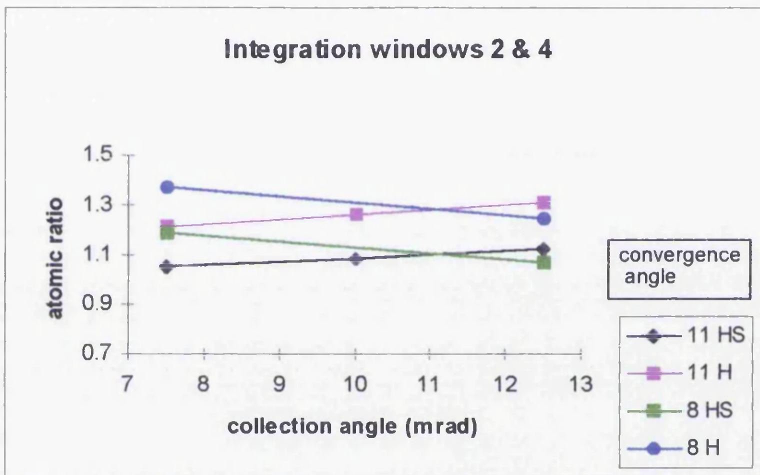

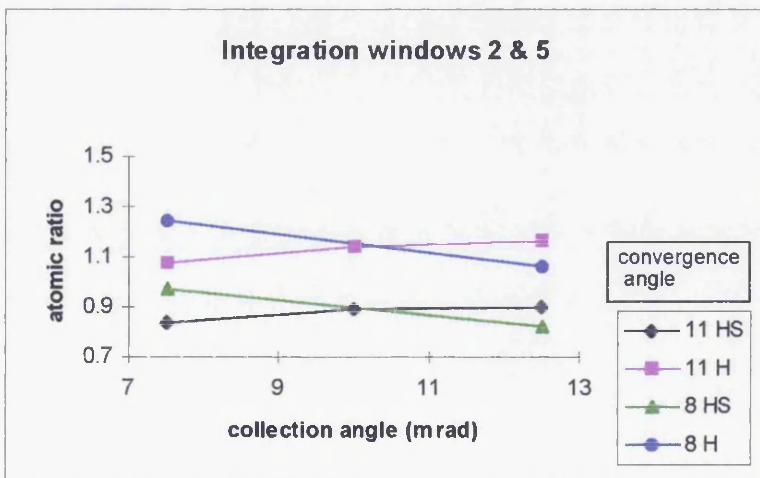

Figure 3.8 *Experimental Cr/N values obtained as a function of collection semi-angle. Data is shown for different convergence semi-angles and using both the Hartree-Slater and the Hydrogenic (with white line correction) models. The integration windows are defined in Table 3.1.*

change by ~25% depending upon the acquisition conditions and the processing parameters. Thus, if data is to be compared it is essential that the same experimental and processing conditions are used.

Table 3.1 *Integration windows for table 3.2.*

window number	window onset (eV)	window width (eV)
1	~397	52
2	~397	102
3	~575	70
4	~575	100
5	600	100

Table 3.2 *Experimental Cr/N values calculated using different integration windows.*
The integration windows which are abbreviated by numbers are described in table 3.1.

collection semi-angle (mrad)	convergence semi-angle (mrad)	Hartree-Slater			Hydrogenic		
		1&3	2&4	2&5	1&3	2&4	2&5
7.5	8	1.12	1.19	0.97	1.28	1.37	1.24
12.5	8	0.99	1.06	0.82	1.14	1.24	1.06
7.5	11	0.97	1.05	0.84	1.12	1.21	1.07
10.5	11	1.01	1.08	0.89	1.16	1.26	1.14
12.5	11	1.04	1.12	0.90	1.21	1.31	1.16

Because of the problems with the cross-sections calculated by EL/P, it was decided to use standard CrN, Cr_2N and $TiN_{0.88}$ to calculate the partial cross-sections. Assuming composition of the standards are as stated, the values of the Cr/N and Ti/N partial cross-sections can be obtained for any specific integration windows. If the same integration windows are used for the data being analysed then these partial cross-section ratios can be used to give the

atomic ratios. The Cr/Ti partial cross-sections can be obtained by matching the N edges in the integration window in the spectra from the different standards.

In order to maintain consistency it was decided to use the integration windows listed in table 3.3 when analysing data. The window onset was chosen as half-way up the steepest part of the edge. It was found that including the pre-edge counts in the integration made a negligible difference to the ratios finally obtained.

Table 3.3 *Integration windows for analysis of EELS data.*

edge	edge threshold (eV)	window onset (eV)	width of window (eV)
N K	401	~397	52
Ti $L_{2,3}$	456	~455	70
Cr $L_{2,3}$	575	~575	70

As seen above using a model to calculate the reduced cross-sections results in an absolute error of about 10%. However there are also random errors that have to be taken into consideration. Random errors were considered by taking a data set where the composition of the specimen should have been uniform. The mean value was calculated along with the standard deviation of the data set and the standard deviation of the mean.

3.3 EDX

3.3.1 Theoretical considerations for EDX

When incident electrons of 100keV are incident on a thin specimen then X-rays are produced by two different mechanisms resulting in bremsstrahlung and

characteristic X-rays. A typical EDX spectrum is shown in figure 3.9 showing characteristic peaks and the bremsstrahlung background.

Bremsstrahlung X-rays are produced when electrons are accelerated in the electric field of the atomic nuclei. The energy of the bremsstrahlung X-rays can be anything between zero and 100keV. The number of these X-rays produced increases as the atomic number of the specimen increases but their energy distribution does not change much so the bremsstrahlung X-rays do not give any chemical information. However they can be used to give an estimate of the mass-thickness of the specimen. A window in the 10-15keV region, known as the white window is commonly used for this purpose in biological applications (Hall, 1971) but has not as yet been widely used in other disciplines. An instrumental contribution is always present in EDX spectra in the form of bremsstrahlung photons from surrounding material. Even if the surrounding material consists of light elements from which characteristic lines are not detected there will still be a bremsstrahlung contribution. It is particularly important to realise this if the bremsstrahlung is being used to obtain an estimate of specimen mass-thickness.

The incident electrons may remove an electron from an inner shell of an atom if they have sufficient energy to overcome its binding energy. The subsequent de-excitation of the atom may result in the production of an X-ray. The energy of this X-ray is the difference in energies of the initial and final states involved in the de-excitation and is therefore characteristic of the atom involved. The total number of these characteristic X-rays produced in a given solid angle, $d\Omega$ is related to the number of atoms of the species of interest in the specimen by a cross-section. The cross-section for the production of a $K\alpha$ X-ray may be defined as

$$\sigma_c = s\omega\sigma_{ik} \qquad (3.12)$$

where σ_{ik} is the total cross-section for the K shell, ω is the fluorescence yield and s is the partition function or branching ratio i.e. the ratio of the $K\alpha$ X-rays

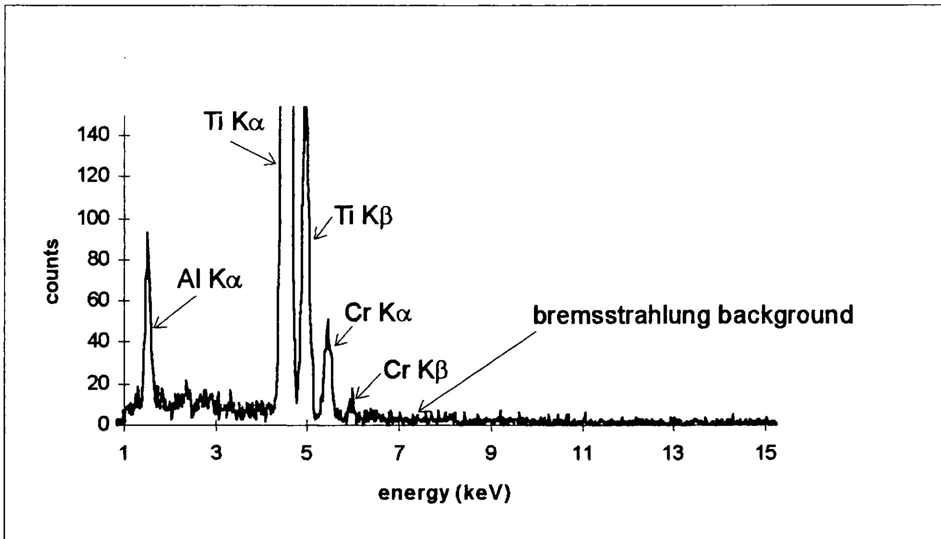

Figure 3.9 *Energy dispersive X-ray spectrum.*

to the total number of X-rays from the K shell. The number of characteristic photons $N_c d\Omega$ emitted in a solid angle $d\Omega$ is given by

$$N_c d\Omega = \frac{IN_o \rho t}{A} \sigma_c \frac{d\Omega}{4\pi} \quad (3.13)$$

where I is the number of incident electrons, N_0 is Avogadro's number, ρt is the mass thickness (ρ is the density and t is the thickness of the thin film) and A is the atomic weight. (Chapman et al, 1984)

Both s and ω have been the subject of extensive investigations and tabulated values are available (Krause, 1979). The ionisation cross-sections can be calculated using the Bethe model (Bethe, 1930) in which the K shell ionization cross-section σ_{iK} is given by

$$\sigma_{iK} = \frac{4\pi e^4 b_K \ln\left(\frac{c_K T_o}{I_K}\right)}{T_o I_K} \quad (3.14)$$

where T_o is the incident electron energy, I_K is the K shell binding energy and b_K and c_K are empirically determined parameters. In this equation T_o is usually taken as the product of the accelerating voltage and the charge of the electron. No account is taken of relativistic effects. If relativistic effects are taken into account then

$$\sigma_{iK} = \frac{8\pi e^4 b_K \left[\ln\left(\frac{c_K m_o v^2}{2I_K(1-\beta^2)}\right) - \beta^2\right]}{m_o v^2 I_K} \quad (3.15)$$

(Inokuti, 1971) where v is the velocity of the incident electrons, β=v/c and b_K and c_K have different values. Paterson et al (1989) examined the variation of b_K and c_K for a range of atomic numbers, Z and incident electron energies, T_o. They found that the use of a universal pair of constants appears to provide a simple and reliable way of calculating ionization cross-sections. Their parameters are given in table 3.4. They noted that the relativistic form of the Bethe model yields a small improvement in accuracy for higher incident electron energies i.e. greater than 100keV. All of the data presented in this thesis was collected with an incident electron energy of 100keV and therefore the non-relativistic Bethe parameters were used.

Table 3.4 *Bethe parameters calculated by Paterson et al (1989).*

model	b_K	c_K	mean deviation (%)	maximum deviation (%)
non-relativistic	0.62	0.90	6.8	19
relativistic	0.43	1.26	6.8	19

Cliff and Lorimer (1975) showed that the weight ratio, C_A/C_B of two elements present in the specimen is directly proportional to the intensity ratio, I_A/I_B of two characteristic X-ray lines and

$$\frac{I_A}{I_B} = \frac{k_A \varepsilon_A}{k_B \varepsilon_B} \frac{C_A}{C_B} \tag{3.16}$$

where

$$k_A = \frac{\sigma_{ik} \omega s}{A} \tag{3.17}$$

and ε is the detector efficiency. The k_{AB} factor for two elements is defined as

$$k_{AB} = \frac{k_A}{k_B} \tag{3.18}$$

The situation is more complicated in the case of the L shell in that the fluorescence yields for the L shells are not so accurately known and radiationless transitions may occur between shells. However, all the quantitative analysis performed in this thesis involved K X-rays.

3.3.2 Analysis of EDX data

In order to analyse data quantitatively the background must be stripped from the peaks of interest. If the peak to background ratio is sufficiently high then the background can be removed using a linear fit. This is done by integrating the counts in windows set on either side of the peak and using these to estimate the background. If the peaks are such that suitable windows cannot be set then

it is necessary to fit a quadratic to the background. The shape of the background is described by a modified Bethe-Heitler (MBH) formula (Chapman et al, 1984) which can be approximated by a quadratic with sufficient accuracy. The main peaks of interest were the Ti Kα and the Cr Kα situated at 4.5 and 5.4 keV respectively. The data were quantified by taking the ratio of the counts and using equation 3.16 to convert to weight ratios. The k_{ab} factor was calculated to be 0.995 for Cr and Ti using the values in table 3.5. The atomic ratios can be calculated from the weight ratios using the atomic weights.

Table 3.5 *Atomic data for Ti and Cr and cross-sections calculated from non-relativistic Bethe model for 100keV. Values of ω and s from Krause (1979).*

atom	atomic number, A	fluorescence yield, ω	partition function, s	cross-section, σ_c (barns)	detector efficiency, ε
Ti	22	0.214	0.8842	477.78	1
Cr	24	0.275	0.8826	370.55	1

In some cases a white window was set on the bremsstrahlung background from 10 to 15 keV. The counts in this window were used as a measure of the mass-thickness of the specimen.

If the specimen is thick then corrections have to be made for fluorescence and adsorption effects. Formulae for such corrections are given in a paper by Nicholson (1994b).

Assuming that the depth distribution of production of X-rays of type A and B are uniform and equal then the following equation can be derived from Goldstein et al (1977) to calculate the differential absorption correction

$$\frac{\left[\mu/\rho\right]_B}{\left[\mu/\rho\right]_A} \times \frac{1-\exp\left\{-\left[\mu/\rho\right]_A \operatorname{cosec}(\alpha)\rho t\right\}}{1-\exp\left\{-\left[\mu/\rho\right]_B \operatorname{cosec}(\alpha)\rho t\right\}} \tag{3.19}$$

where $[\mu/\rho]_A$ is the mass absorption coefficient for absorption of X-rays of type A in the specimen , ρ is the specimen density, t is the specimen thickness and α is the take-off angle of the detector. The take-off angle is the angle between the specimen surface and the axis of the collimator on the X-ray detector. The large take-off angle of the detector on the HB5 reduces the effect of absorption by decreasing the path length for the X-rays in the specimen. The density and mass absorption coefficients for Ti and Cr are tabulated in table 3.6. It was estimated that the maximum thickness of specimen on which EELS could be performed was of the order of 100nm. The maximum thickness of specimen used for collection of EDX data was estimated to be roughly 300nm. The differential absorption coefficients were calculated for a range of specimen compositions and a take-off angle of 38°. The mass absorption coefficient changed from 0.95 to 1 as the composition varied from pure Ti to pure Cr. Therefore, even assuming that the specimens were as thick as 300nm, absorption will have little effect on the significance of the data.

Table 3.6 *Absorption coefficients (Heinrich, 1979) and densities (Kaye & Laby, 1975).*

absorber	density ($g\ cm^{-3}$)	μ/ρ for Ti Kα ($cm^2\ g^{-1}$)	μ/ρ for Cr Kα ($cm^2\ g^{-1}$)
Ti	4.508	108	571
Cr	7.194	144	86.7

CHAPTER 4

CrN coating of Ti(6%wtAl, 4%wtV)

4.1 Introduction

At atmospheric pressure, pure Ti exists as hcp α-Ti up to a temperature of ~882°C (Hansen, 1958). Above this temperature the bcc β-phase is stable. The addition of relatively small amounts of other elements raises or lowers the α/β transition temperature. There is a wide range of Ti alloys, the most common of which is Ti(6%wtAl, 4%wtV). This is an α+β alloy of Ti, containing Al which is an α-stabiliser (raising the transition temperature) and V which is a β-stabiliser (lowering the transition temperature). Therefore, this alloy contains both phases although the α phase is predominant, with only small amounts of retained β phase. The relative quantities of the α and β phases present are dependent upon the heat treatment.

Due to the high cost of Ti, the use of Ti(6%wtAl, 4%wtV) is generally restricted to applications where materials with both high performance and a high strength to weight ratio are required, such as in the aerospace industry where it is widely used. The alloy is also widely used in biomedical implants. The coating of Ti(6%wtAl, 4%wtV) is therefore of industrial interest because

enhanced performance as a result of coating would have great financial benefits.

CrN is used as a coating for corrosion protection and in applications where abrasion is the wearing element. Although there has been extensive reporting of TiN in literature, there has been relatively little recorded on the characterisation of CrN. This chapter presents imaging, analytical and diffraction results from samples of CrN deposited on Ti(6%wtAl, 4%wtV) under different conditions with particular attention being paid to the study of the interfacial region.

The samples, which are described in detail in section 4.2, consist of coatings deposited with different substrate biases and with different angles of orientation between the substrate surface and the cathode surface. Section 4.3 examines the surface structure of these coatings. The grain growth and size is investigated in section 4.4. Section 4.5 discusses the chemical composition and crystallographic structure of the samples. Complete chemical data sets were taken from all of the samples. However, these samples were deposited in a way that would be suitable for the production of commercial coatings and therefore there are inherent complications in studying them. The substrate is a commercial alloy with an uneven surface which proves difficult to polish. As mentioned above, Ti(6%wtAl, 4%wtV) is a complex material containing more than one phase. The polycrystalline nature of the substrate means that there is no simple crystallographic direction normal to the surface. The implication of this is that the substrate orientation cannot be used to align the interface. Therefore, the only way of orientating a cross-section specimen in the microscope, to ensure that the incident electron beam direction is parallel to the interface plane, is by tilting until the interface appears as narrow as possible. This is difficult to achieve and practical difficulties with contamination make it undesirable to use the local area of specimen to be analysed for the purpose of orientating the specimen in the electron beam. Even if a cross-section specimen is orientated correctly in the microscope, there may still be some regions of different chemical composition or crystallographic structure

overlying one another because of the local surface roughness of the substrate. The deviations of the interfaces from the ideal orientation are estimated from the measured concentration profiles and are summarised in table 4.6 (page 70). Such deviations make the understanding of the chemical analyses data more difficult. Therefore, to give the clearest picture to the reader, the discussion will initially centre on the data set with the minimum estimated tilt error. Comparisons with the other data sets will be made as the discussion develops. Section 4.6 presents the results of diffraction work on two samples. Finally, section 4.7 summarises the observations made in this chapter and the conclusions that can be drawn.

4.2 Description of samples

The samples studied in this chapter were made by depositing CrN onto Ti (6%wt Al, 4%wtV). Table 4.1 summarises the conditions which the samples were subjected to in the sputter cleaning and coating cycles. During the sputter cleaning process the substrate bias was always held at -1000V and therefore the term 'substrate bias' will be used to refer to the substrate bias during the coating process, unless otherwise stated.

Two sets of three samples were deposited with different substrate biases (table 4.1). For the first set, the titanium alloy substrates were mounted on the copper block described in section 2.2 with their surfaces parallel (0°), at 45° and perpendicular (90°) to the cathode surface. The substrates were sputter cleaned with Cr ions for 25 Amp hours at -1000V substrate bias. The substrate bias was then reduced to -70V and the substrates were coated with CrN for 41 Amp hours. The second set of samples were prepared as the first, but with a substrate bias of -200V for the coating process which lasted 40 Amp hours. The surface temperatures of the samples in the two separate sets were 230C and 300C respectively. These differences are not thought to be significant for three reasons. Firstly, the process is dynamic rather than being in thermodynamic

equilibrium (P. Hatto, private communication). Secondly, the technique for measuring the temperature is not exact enough to differentiate unequivocally between such values. Thirdly, Aharonov et al (1993) and showed that CrN coatings deposited at ~200C and ~500C had very similar properties. Similarly Gåhlin et al (1995) observed that CrN coatings deposited at ~200C and ~400C had similar grain sizes and showed very similar mechanical and tribological properties. The 10° samples will be discussed later.

Table 4.1 *Summary of sputter cleaning and deposition parameters of samples discussed in this chapter.*

angle of orientation to cathode	sputter cleaning cycle		coating cycle		
	temperature (C)	Amp hours	substrate bias (V)	temperature (C)	Amp hours
0°	240	25	-70	230	41
45°	240	25	-70	230	41
90°	240	25	-70	230	41
0°	320	25	-200	300	40
45°	320	25	-200	300	40
90°	320	25	-200	300	40
10°	320	9.5	-150	260-340	12
10°	340	7.1	-	-	-

Because of the nature of the cleaning and deposition cycles, there will be some similarities between samples from the first two sets. For the two sets of samples, the copper block was rotating in the chamber for both the sputter cleaning and the deposition processes. This rotation took the form of a single rotation around the axis in the centre of the chamber. The resultant geometry meant that the samples whose surfaces were parallel and at 45° to the cathode surface experienced changes in orientation to and distance from the cathode as they rotated. These two orientations should produce very similar coatings and

interface regions in a given deposition cycle as their projected surface areas in the plane of the cathode surface are similar. The perpendicular sample should be quite different as its projected area in the plane of the cathode is zero. The orientation of this sample to the cathode remained unchanged during the rotation although it rotated within the plane of its surface and its distance from the cathode varied.

The sputter cleaning process was the same for both runs and should therefore, have an identical effect on a substrate with a given geometry. However, the surface structure formed may have been modified in different ways during the subsequent coating process because of the different substrate biases (and hence different ion energies). However, the difference in bias should have a far greater effect on the coating than on the interface region. Features of the coating that may be affected by the substrate bias are the stoichiometry of the coating, its internal stress, its grain size, its grain structure and its crystallography.

Some results from a coating deposited with a substrate bias of -150V and an orientation of roughly 10° to the cathode (table 4.1) are also presented in this chapter. This sample was Cr sputter cleaned for 9.5 Amp hours and coated for 12 Amp hours. The temperature achieved during sputtering was 320C.

The final sample listed in table 4.1 was Cr sputter cleaned for 7.1 Amp hours, achieving a substrate temperature of 340C. This sample was not coated and was therefore used to examine the effect of the sputter cleaning process alone.

4.3 Examination of CrN coating surface

Secondary electron imaging in a scanning electron microscope (SEM) was used to examine the surface structure of the coatings. Figures 4.1-4.3 show SEM

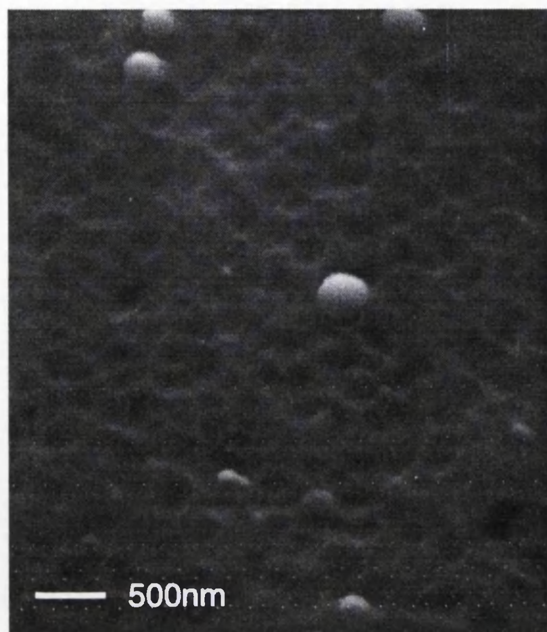

Figure 4.1 *SEM image of parallel sample deposited at -70V.*

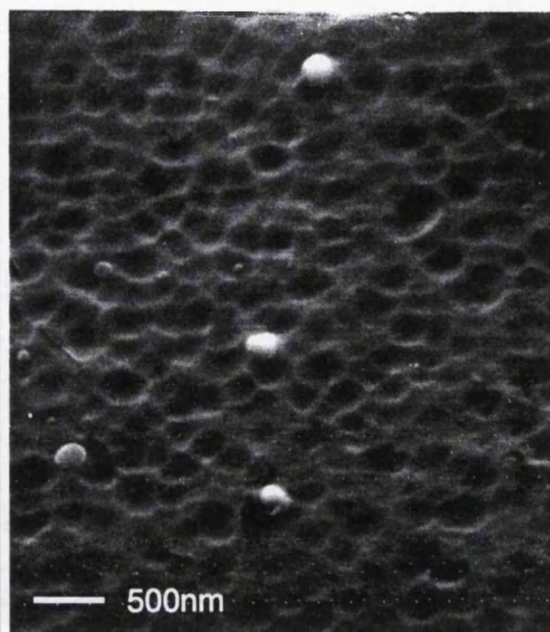

Figure 4.2 *SEM image of 45° sample deposited at -70V.*

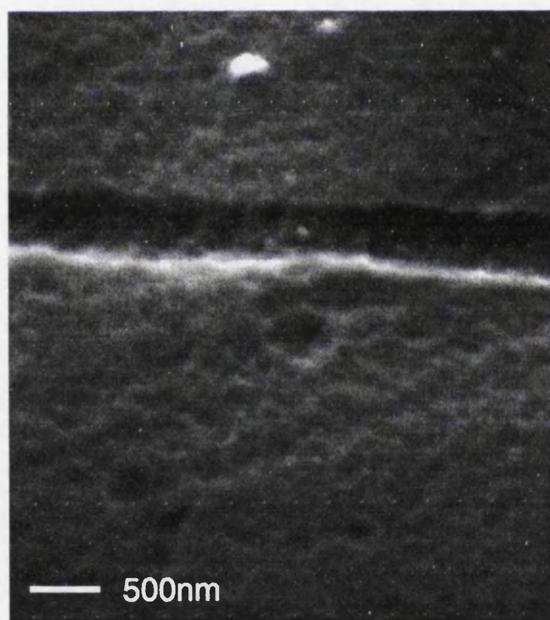

Figure 4.3 *SEM image of perpendicular sample deposited at -70V.*

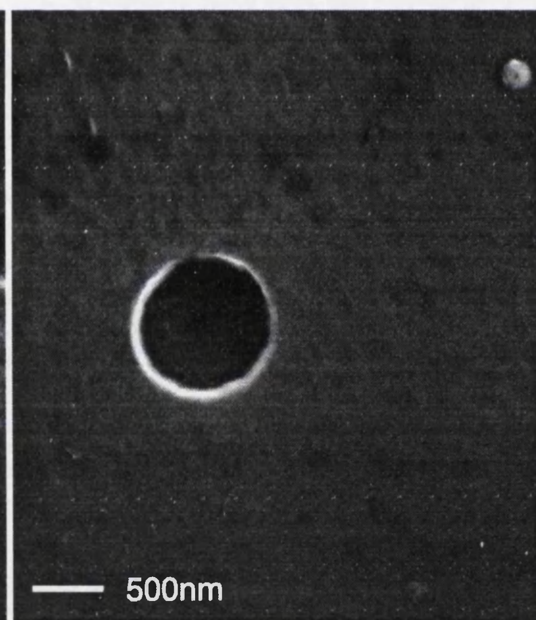

Figure 4.4 *SEM image of sample deposited at -150V.*

images of the three samples deposited at -70V. These samples were tilted 45° in the electron beam in the SEM to increase the contrast in the resulting image. Figure 4.1 shows that the coating deposited with the cathode surface parallel to the substrate surface has a surface structure with pits which have diameters of the order of 300nm and are separated by regions of about 100nm. Several microdroplets can be seen on the coating surface. These are droplets of chromium which are present on all of the coatings and will be studied in more detail in chapter 6. The 45° coating is very similar to the parallel coating as is illustrated in figure 4.2. The perpendicular coating in figure 4.3 has some pits of the same dimensions as those in the coatings in figures 4.1 and 4.2. However, most of the pits apparent in this image are of the order of 100nm across and have less depth than those in figures 4.1 and 4.2. The scratch which can be seen in this figure suggests that the surface morphology of the coating may be closely related to the surface structure of the underlying substrate.

Figure 4.4 shows the coating deposited at -150V and at 10° i.e., essentially parallel to the cathode. The surface is similar to that of the -70V parallel sample in figure 4.1 although there is less image contrast as the sample was not tilted.

A closer investigation of the coating is required to determine whether the structure surface of the coatings is a direct result of the grain size and growth within the coatings or if it is also related to some other parameter such as the surface structure of the underlying substrate.

4.4 Grain size and growth in the samples

Figures 4.5-4.11 show typical TEM bright and dark field pairs of samples taken from planar specimens. The images in figures 4.5-4.7 illustrate that the three coatings deposited with a substrate bias of -70V have a distribution of grain

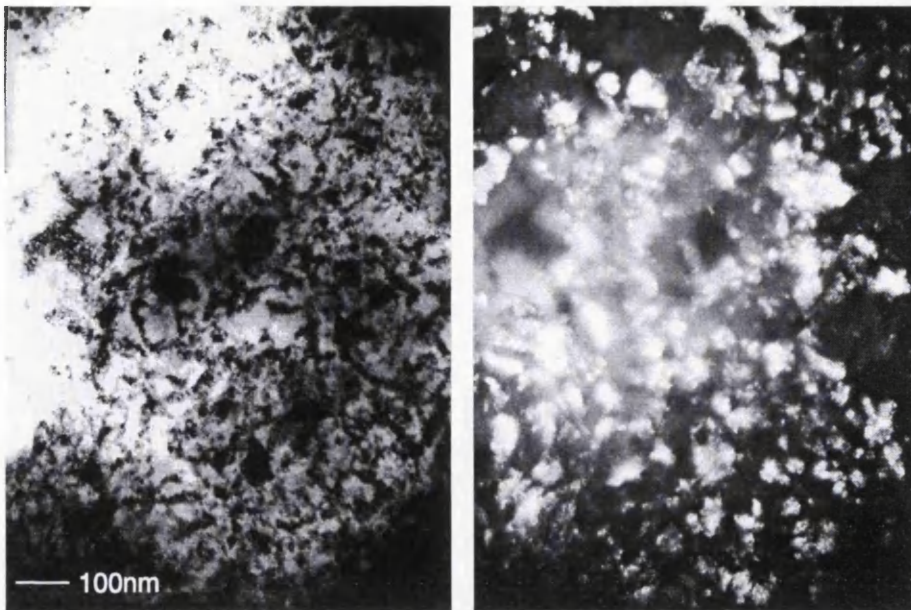

Figure 4.5 *Bright and dark field pair of parallel sample deposited at -70V.*

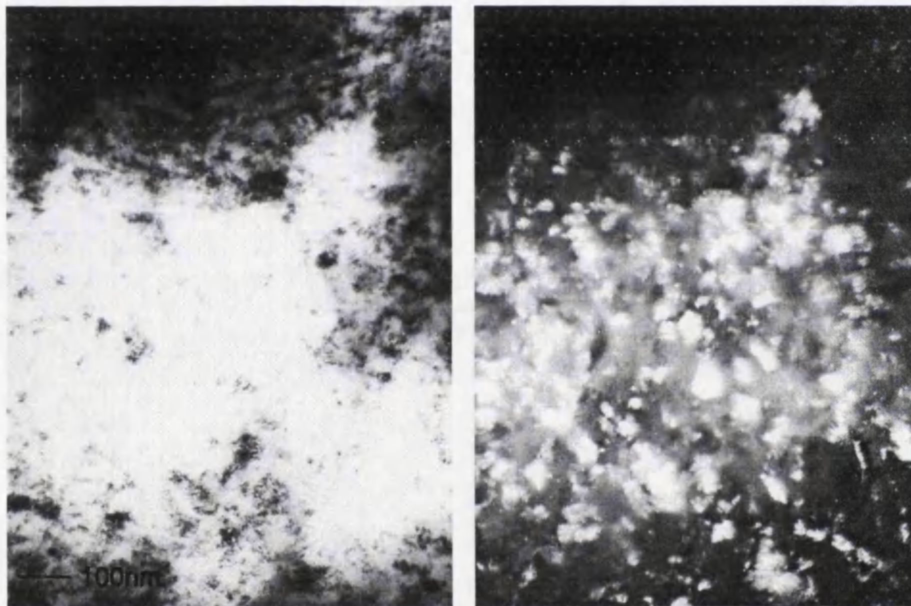

Figure 4.6 *Bright and dark field pair of 45° sample deposited at -70V.*

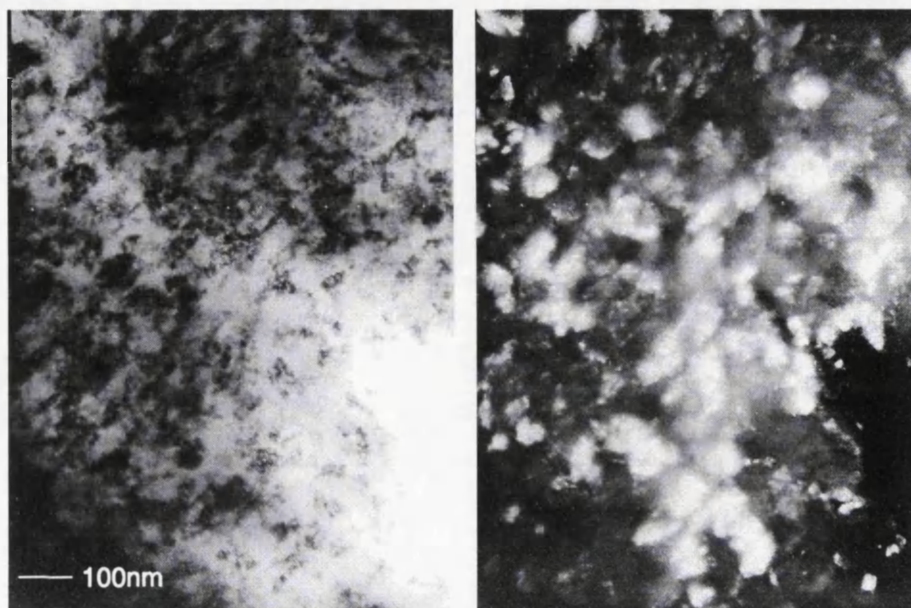

Figure 4.7 *Bright and dark field pair of perpendicular sample deposited at -70V.*

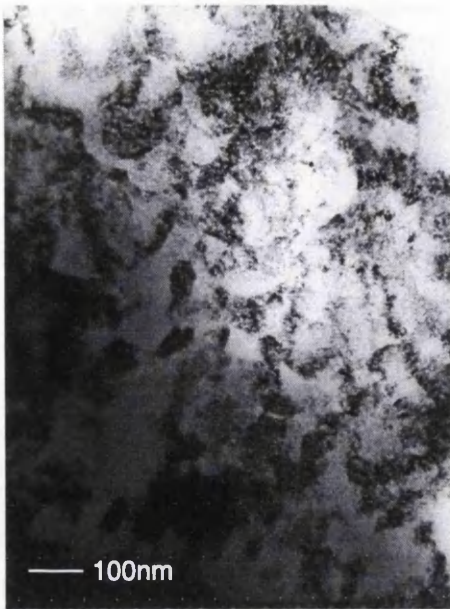

Figure 4.8 *Bright and dark field pair of parallel sample deposited at -200V.*

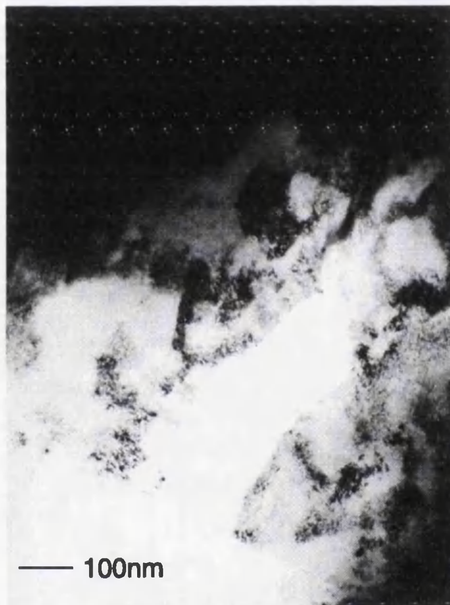

Figure 4.9 *Bright and dark field pair of 45° sample deposited at -200V.*

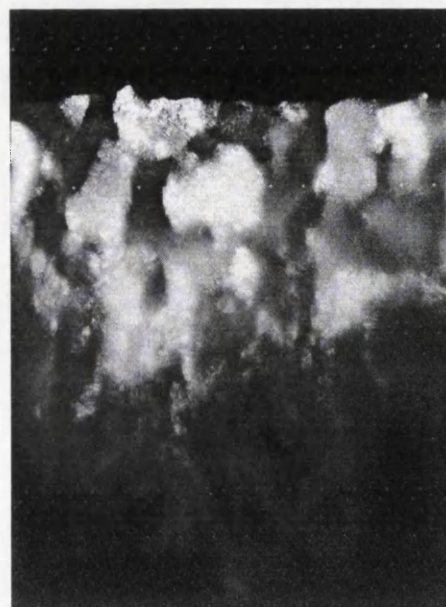

Figure 4.10 *Bright and dark field pair of perpendicular sample deposited at -200V.*

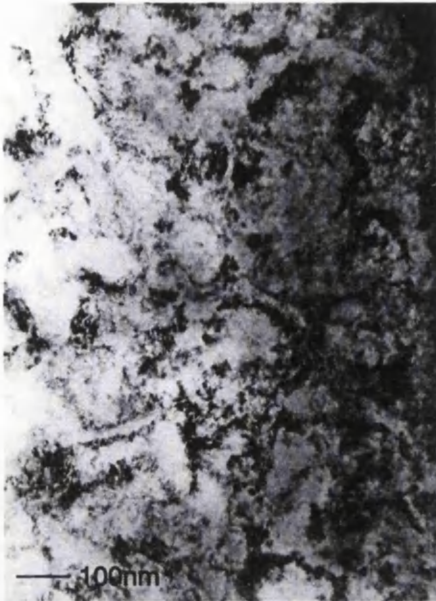

Figure 4.11 *Bright and dark field pair of 10° sample deposited at -150V.*

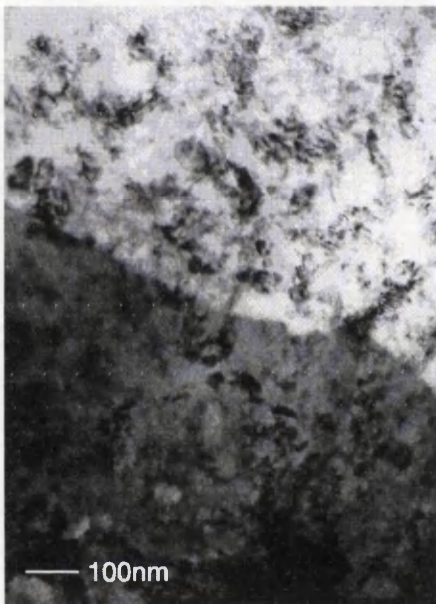

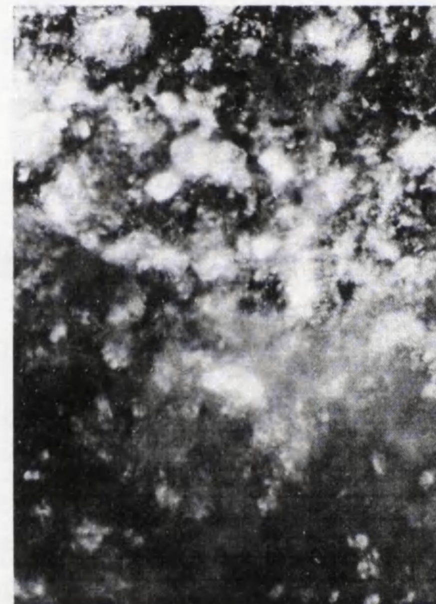

Figure 4.12 *Bright and dark field pair of Cr sputter cleaned substrate.*

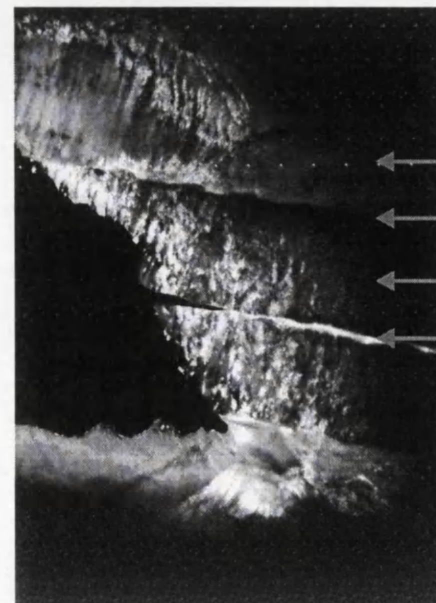

Figure 4.13 *Bright and dark field pair of parallel sample deposited at -70V.*

sizes. The sample which was prepared with its surface parallel to the cathode surface is shown in figure 4.5. The grains have dimensions between 20nm and 170nm with a typical grain size of 50nm. These grain sizes are estimated by eye from the images. The 45° sample in figure 4.6 has a similar distribution of grain sizes. Figure 4.7 shows that the perpendicular sample also has grains with sizes ranging from about 20nm to 170nm. However, the relative number of larger grains has increased and a typical grain size is 100nm.

The grains in the parallel coating deposited at -200V, shown in figure 4.8 are larger than those observed above, with a typical grain size of 100nm and a range of 50-230nm. The 45° sample (figure 4.9) has a similar range of grain size with a typical size of 140nm. The grains in the perpendicular coating (figure 4.10) range from 50-230nm with a typical grain size being 170nm.

For a substrate bias of -150V the distribution of grain sizes is 30-220nm as is demonstrated in figure 4.11; a typical grain size in this sample is 90nm.

Figure 4.12 shows the grains in the sample which was sputter cleaned but not coated. The distribution of grain size is between 20nm and 150nm with a typical grain size of 50nm. This figure shows the structure at the surface of the substrate but it is also likely to show some of the underlying substrate. At this stage it is not possible to separate these structures although it is likely that the two large regions of different contrast are a result of different underlying substrate grains. The substrate structure near the surface has possibly been modified by the polishing and sputter cleaning processes resulting in the small grains seen in the image. It is necessary to look at the substrate in cross-section in order to determine whether these grains are only representative of the structure near the surface of the substrate or are typical of the bulk substrate.

A summary of the typical grain sizes observed above are given in table 4.2 below. Two conclusions can be drawn from these observations. The grain size increases as the substrate bias increases, with the characteristic grain size for a given orientation roughly doubling for a change of substrate bias from -70V to

-200V. A similar effect was noted by Wang et al (1995) for films grown by ion beam enhanced deposition. There is a grading of grain size as the angle of orientation between the cathode and substrate surfaces increases with the density of larger grains increasing.

Table 4.2 *Summary of typical grain size observed in planar section.*

orientation	typical grain size (nm)		
	-70V	-150V	-200V
0°	50	90	100
45°	50	-	140
90°	100	-	170

There is the possibility that the grain size is affected by the film thickness with the grains getting larger as the thickness increases (Perry, 1989) so it is necessary to examine the coatings in cross-section in order to study the grain growth and see if the grain size changes with thickness. The remainder of this section presents bright and dark field images from cross-sectional specimens before summarising the observations.

Figure 4.13 shows a typical cross-sectional specimen which has been thinned to produce electron transparent areas. This image, which is for the -70V parallel sample coating, shows both halves of the cross-section with the glue line running across the centre. On either side of the glue line is the coating. At the top and bottom of the image is the substrate. Between the coating and the substrate is the narrow interface region.

Figures 4.13-4.19 are bright and dark field pairs of the -70V and -200V samples in cross-section. The -70V parallel coating (figures 4.13 and 4.14) looks as if it is highly faulted, with lots of structural defects within the grains. This faulting is probably a result of the high stress which results from deposition at low substrate bias (Hatto, private communication; McKenzie et

Figure 4.14 *Parallel sample deposited at -70V.*

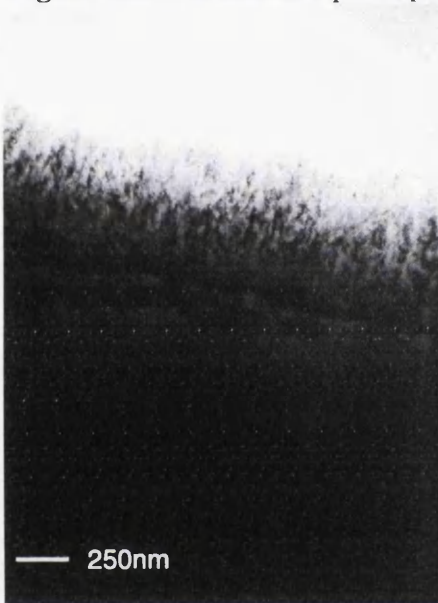

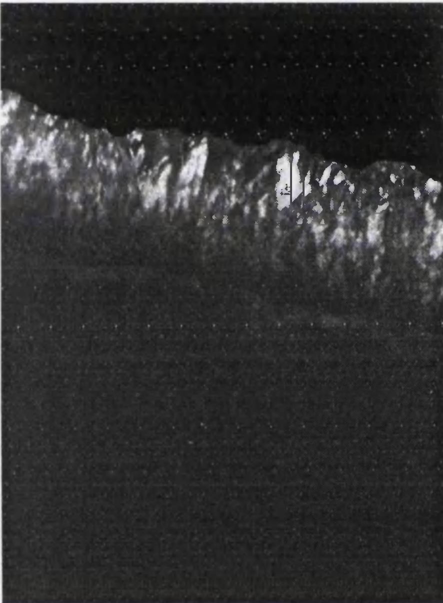

Figure 4.15 *45° sample deposited at -70V.*

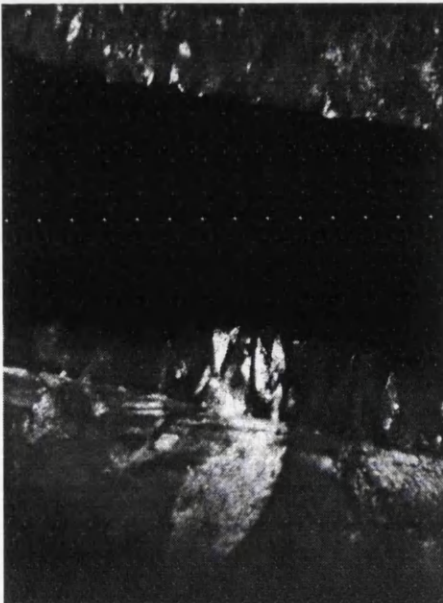

Figure 4.16 *Perpendicular sample deposited at -70V.*

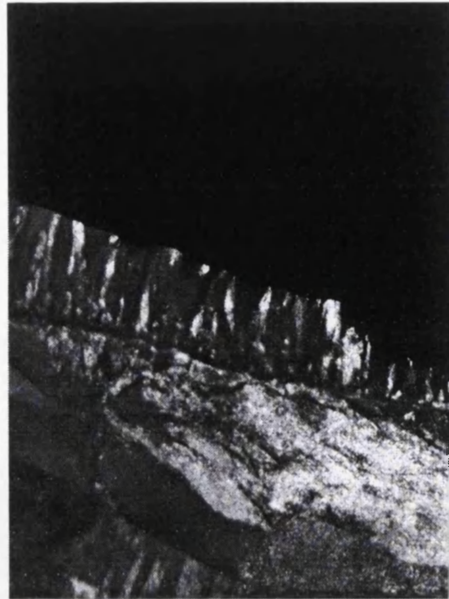

Figure 4.17 *Parallel sample deposited at -200V.*

Figure 4.18 *45° sample deposited at -200V.*

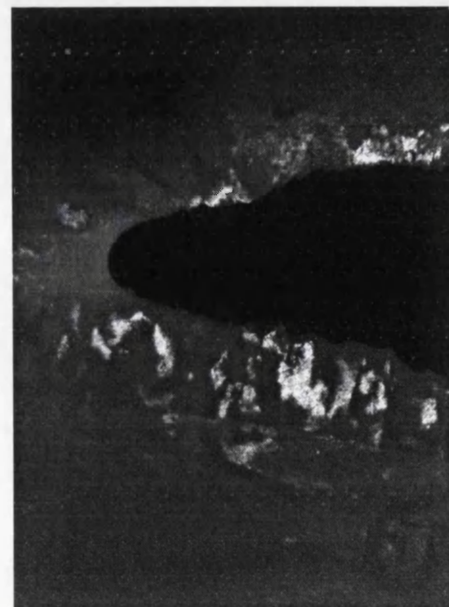

Figure 4.19 *Perpendicular sample deposited at -200V.*

al, 1996). The grain growth is columnar with grains typically about 50nm wide, matching the size observed in planar section in figure 4.5.

The coating in the 45° sample in figure 4.15 has a very similar structure to the coating on the parallel sample. The grain growth and size is similar and again the coating looks highly faulted.

The perpendicular sample (figure 4.16) is different from the parallel and 45° samples. The coating appears much less faulted and the columnar grains are about 100nm wide.

Figure 4.17 is an image of the -200V parallel specimen. The coating has fewer defects than the -70V parallel coating with the grains growing in columns which are about 80nm wide. The 45° sample in figure 4.18 is similar to the parallel sample with a typical column width of roughly 110nm. Figure 4.19 shows the perpendicular sample which is different since the column width is about 140nm.

All of the coatings can be seen to exhibit columnar growth which is characteristic of arc deposited coatings (Håkansson, 1991). The widths of the columns match the grain sizes observed in the planar sections with the width increasing as the substrate bias becomes more negative and as the angle between the substrate surface and the cathode surface increases. These observations from the cross-sectional specimens corroborate the trends in grain size with orientation and substrate bias noted when examining the samples in planar section above. The grains in the coatings are densely packed with no evidence of voids. The -70V perpendicular coating contains fewer defects than the other -70V coatings. The number of defects in the coatings decreases as the substrate bias becomes more negative.

The thickness of coating deposited on each sample can be determined from cross-sectional images. However, care has to be taken that the measurement is made in a region such as that observed in figure 4.13 where the ion milling has

not removed any of the coating. The coating thicknesses measured are summarised in table 4.3. The values in the table appear anomalous in that the two sets do not follow the same trend. Further work is required to confirm that this is not the result of an artefact created at some point in the preparation process. While one would expect the thickness of the coating to decrease as the angle of orientation increases, the situation is more complex because the substrates are rotating. The relative thicknesses depend upon the relative times that the substrates are in line of sight of the cathode as well as their orientation. The 90° sample always maintains the same orientation to the cathode although the relative distance changes but the 0° and 45° samples both go out of line of sight of the cathode. The situation is further complicated by the fact that the ion trajectories are determined by both the gas pressure and the electric field within the chamber resulting from the substrate bias. Further light is thrown on the effect of these parameters in chapter 5 and further discussion is left until that point.

Table 4.3 *CrN coating thickness.*

substrate bias (V)	orientation	coating thickness (nm)
-70	0°	397±10
-70	45°	191±15
-70	90°	216±15
-200	0°	377±10
-200	45°	472±15
-200	90°	265±25

The cross-sectional images can also be used to study the surface roughness of the coatings and in principle, it is possible to compare the surface topography seen in the SEM images in section 4.3 with the coating surface visible in the cross-sections. However, some of the coatings shown above have partly been eroded by the ion milling process such as the coating in the -70V 45° sample

(figure 4.15) so that no observations can be made about the surface structure. The -70V parallel coating which has not been eroded in the region shown in figures 4.13 and 4.14, has a surface depth variation of the order of 30nm on a lateral scale of about 100nm. This is consistent with the lateral surface structure on a scale of the order of 100nm for the separation of the pits observed in figure 4.1 for the same sample. The substrate surface in this sample is also locally non-flat with typical lateral variations of the order of 100nm and depth variations of about 30nm. However, the coating surface is not a replica of the underlying substrate surface. Nor is the surface finish of the coating simply a result of the grain size in the coating.

The substrates in figures 4.13-4.19 contain grains which are up to 1μm in size and are therefore several orders of magnitude larger than the grains in the coating. However, there are smaller grains near the substrate surface where the structure has been modified by the polishing and/or sputter cleaning process. They are of the same order of magnitude as the 50nm grains observed in the planar section in figure 4.12 showing that these grains were characteristic of the surface region of the substrate rather than the bulk substrate. These smaller grains could have been formed during the sputter cleaning process as a result of recrystallisation or annealing of the mechanical damage introduced by the polishing process.

The substrate surfaces in the perpendicular samples are smoother than that of the 0° and 45° samples, suggesting that the final substrate surface roughness is affected by the sputter cleaning process. The amount by which the substrate surfaces are modified by the sputter cleaning process depends upon the angle of orientation.

Examination of the interface region shows that it is non-flat and of non-uniform thickness. The interface regions in the perpendicular samples are narrower as well as flatter than in the other samples. If the cross-sectional images above are studied carefully then two regions or layers of contrast can be seen at the interface in some of the images e.g., figures 4.14 and 4.16.

These layers are seen more clearly if the interface is studied at a higher magnification as for the -70V perpendicular sample in figure 4.20. The two layers of different contrast at the interface are clearly delineated in the dark field image indicating different diffraction conditions and hence different crystallographic structures or orientations. The layer closest to the substrate is of the order of 7nm wide in this image. The next layer has a similar width of about 10nm. Both of these layers are crystalline whereas amorphous layers have been observed in other systems.

Several conclusions can be drawn from this study of the grain size and growth. There is a grading of grain size in the coating as the angle of orientation between the cathode and substrate surface increases with an increasing number of larger grains. The grain size increases as the substrate bias increases, with the characteristic grain size for a given orientation roughly doubling for a change of substrate bias from -70V to -200V. The coating surface roughness is similar to the substrate surface roughness but does not follow it exactly, nor is the surface finish of the coating simply a result of the grain size within the coating. The substrate surface is smoother for the perpendicular samples than for the 45° and parallel samples. The near surface regions of the substrates contain grains which are several orders of magnitude smaller than the grains in the bulk substrate. These smaller grains are thought to be a result of the combined effect of the polishing and sputter cleaning processes applied to the substrate. The interface region is made up of two layers: these are non-uniform in width but the uniformity increases as the angle between the substrate surface and the cathode increases. The identification of these interface layers is addressed in the next section which examines the composition and crystallographic structures of the samples.

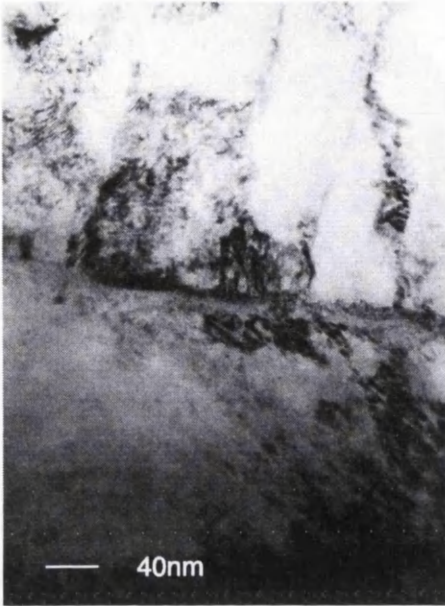

Figure 4.20 *Perpendicular sample deposited at -70V.*

4.5 Chemical composition and crystallographic structure of the samples

This section examines the elemental distribution in the different crystallographic regions observed in the previous section. EDX and EELS were employed to study the chemical composition of the samples. EELS was also used to give some information on the chemical environment of the atoms and hence the crystallographic structure.

Figure 4.21 shows an EELS line trace across a grain boundary in a planar specimen deposited at -150V. The error bars shown in this figure are typical of all the line profiles presented in this thesis and therefore error bars will not be shown on the others. It can be seen that there is no sharp change in composition at the grain boundary although the composition is not uniform. This figure also shows that electron channelling, which might cause an apparent change in composition at grain boundaries, has not affected the results. The specimen preparation technique used to prepare planar specimens removes material from the substrate side of the specimen to leave electron transparent regions of coating with the result that only the top ~100nm of the coating remains in such regions. This coating is representative of the steady-state condition (i.e., the deposition process has stabilised and the coating would continue to grow in more or less the same way indefinitely). However, the figure demonstrates that the coating is substantially sub-stoichiometric with an average composition of $CrN_{0.66}$. The stoichiometry of the coatings will be addressed below.

Figures 4.22 and 4.23 are EDX and EELS line profiles, respectively taken across the interface of the parallel sample deposited at -200V. The EDX profile shows an apparent concentration of Ti of about 5% in the coating. This signal is not indicative of 5% Ti in the coating but is a result of electron scattering causing X-rays from the bulk specimen to contribute to the spectrum.

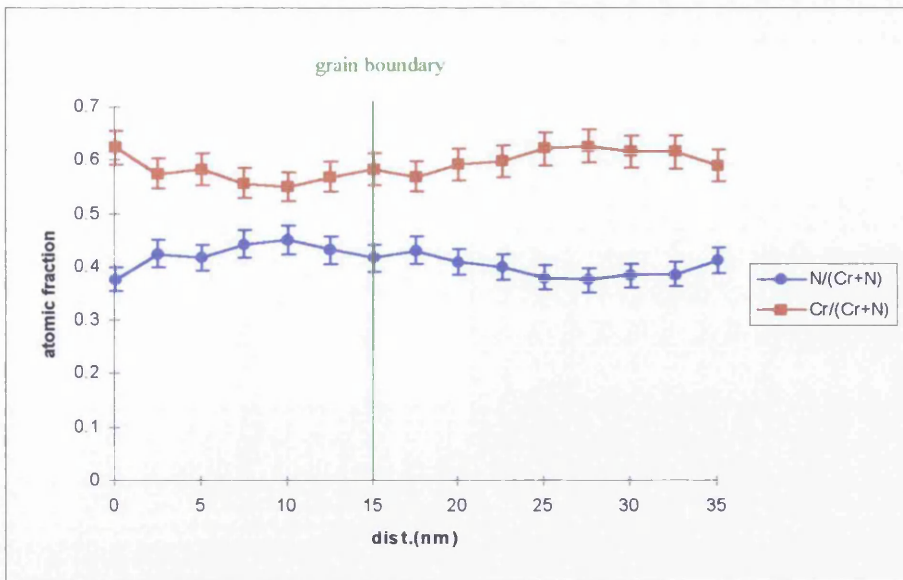

Figure 4.21 *EELS line profile across grain bounary in -150V sample.*

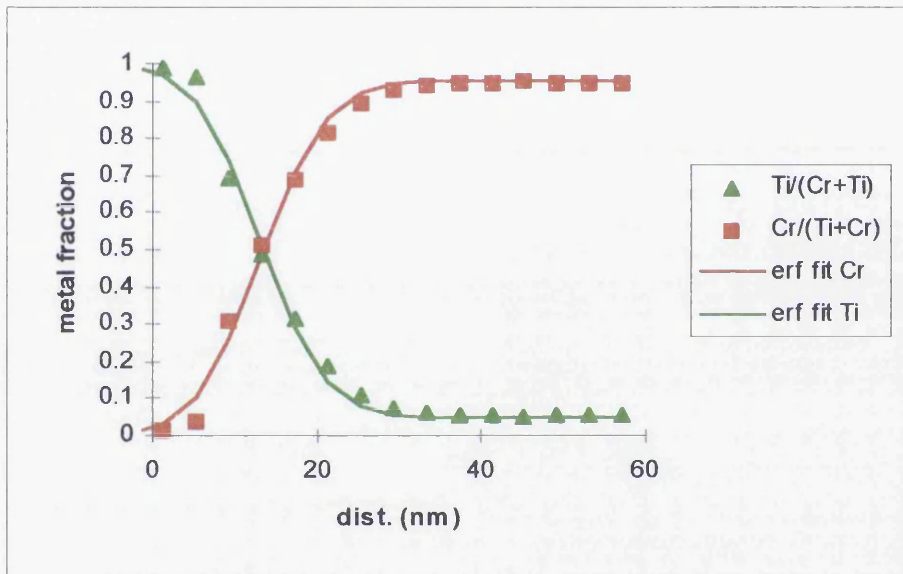

Figure 4.22 *EDX line profile of parallel -200V sample.*

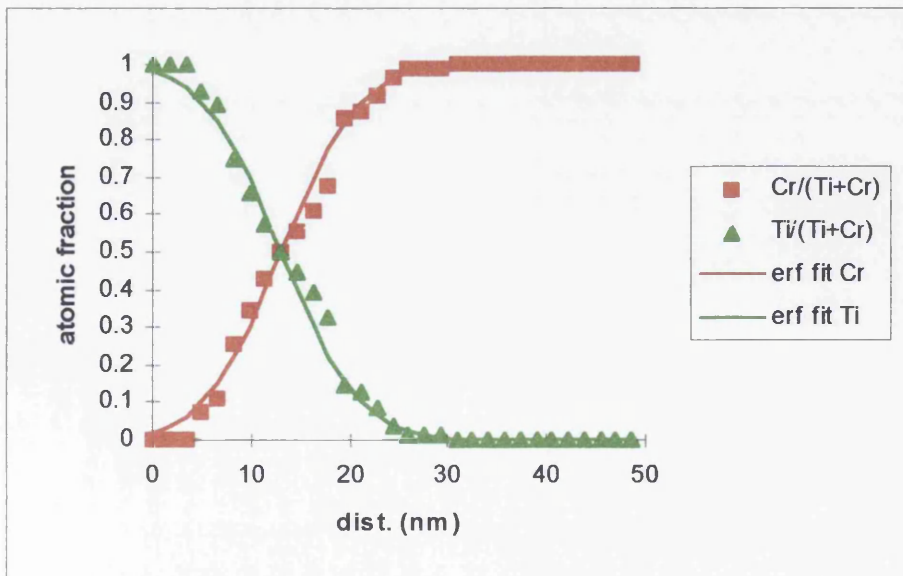

Figure 4.23 *EELS line profile of parallel -200V sample.*

The elemental traces look rather like diffusion profiles. The sputtering process is energetic and, although the system is not in equilibrium, the process is likely to be diffusion driven. An ideal diffusion couple can be described mathematically by error functions. Therefore, error functions were fitted to the data to obtain an estimate of the interface width. Resultant 10-90% metallic/ceramic interface widths of 18.6nm and 15.1nm were obtained from fitting error functions to both the EDX and the EELS data, respectively. The best fit of the error function is determined by eye and an adjustment of 0.1nm in the width makes the fit worse. However, the error in the interface widths calculated is likely to be appreciably larger than this as the function does not fit the data perfectly. More importantly these are local values and the actual metallic/ceramic interface width varies along the sample. Marked deviations from the shape of a perfect diffusion couple can be seen in both the EDX and the EELS line profiles. These discontinuities are thought to be a result of the system trying to achieve equilibrium via a diffusion mechanism during the sputter cleaning and subsequent deposition. They are unlikely to be an artefact resulting from electron channelling due to changes in the crystal structure because figure 4.21 shows no apparent change of composition crossing a grain boundary despite a large change in the diffraction contrast which corresponds to a change in the electron channelling. The presence of the discontinuities in both the EELS and the EDX data sets indicates that they are a real effect and not just a product of specimen drift because the data were collected as two separate consecutive line traces and not simultaneously.

EDX was also used to examine the concentration of Al present in the substrate. There did not appear to be any segregation of Al at the surface of the substrate as the Al concentration remained constant at ~5% of the substrate. The V concentration was not determined because the V $K\alpha$ and $K\beta$ lines overlap the Ti $K\beta$ and the Cr $K\alpha$ lines, respectively.

Figure 4.24 is the same EELS line profile as figure 4.22 but the N content has now been included. The sharp onset of the nitrogen signal indicates that the specimen was tilted correctly for analysis. Figure 4.25 shows EELS spectra on

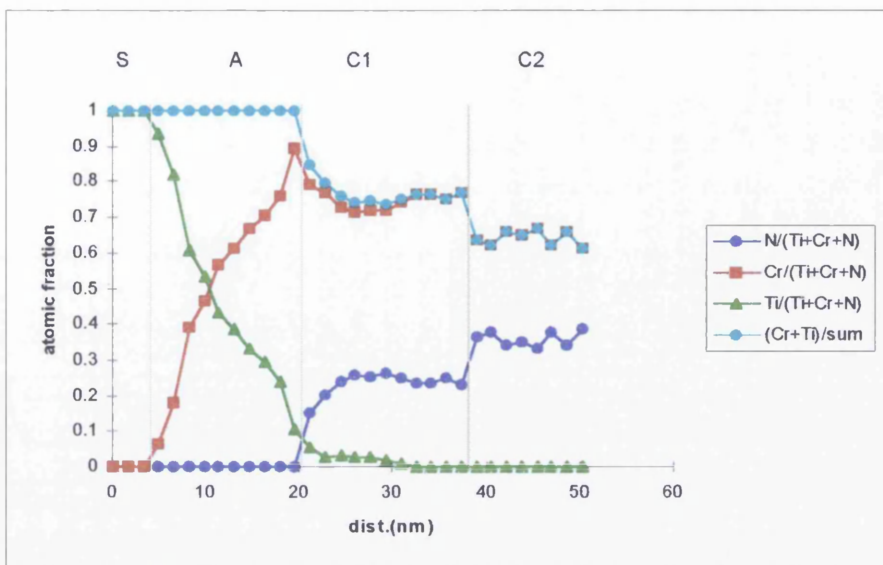

Figure 4.24 *EELS line profile of parallel -200V sample.*

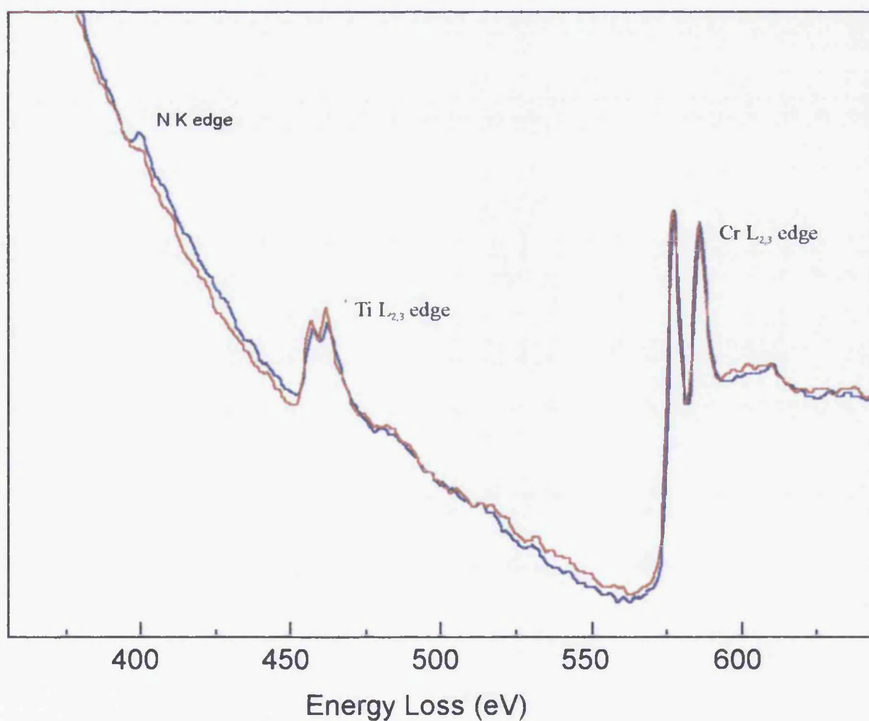

Figure 4.25 *Onset of N signal in line profile in figure 4.24.*

either side of this onset. The N signal appears over a single step corresponding to a distance of 1.6nm. The specimen thickness at this point, estimated from the EELS low-loss spectrum, is ~116nm, assuming a mean free path of 100nm. This corresponds to an error in the specimen tilt of the order of 0.8°. However, due to the uncertainty of the mean free path the error in the tilt could be larger than this. Because the error in the tilt is smallest for this data set, this line profile will be discussed first. The line profile has been split into 4 sections each of which will be discussed below; these are substrate (S), Ti:Cr alloy (A), coating 1 (C1) and coating 2 (C2).

Substrate

The first section is substrate which has not been chemically altered by the sputter cleaning or the coating processes and is therefore of little interest to this discussion. However, the Ti $L_{2,3}$ edge ELNES and the shape of the low-loss spectrum in this region will be used for comparisons with the other sections of the profile.

Ti:Cr alloy

The next region is a Ti:Cr intermixed region of graded composition. Examining the Cr-Ti phase diagram in figure 4.26, it can be seen that there is very little solubility of Cr in α-Ti. However, at higher temperatures there is solubility of Cr in β-Ti across the full range of compositions. The sputter cleaning process is known to be energetic and probably causes local migration of atoms similar to a high temperature effect. Therefore, it is quite likely that the high temperature region is the relevant part of the phase diagram. The addition of Cr to Ti should have the same effect as adding V which is a β stabiliser, stabilising the bcc β phase.

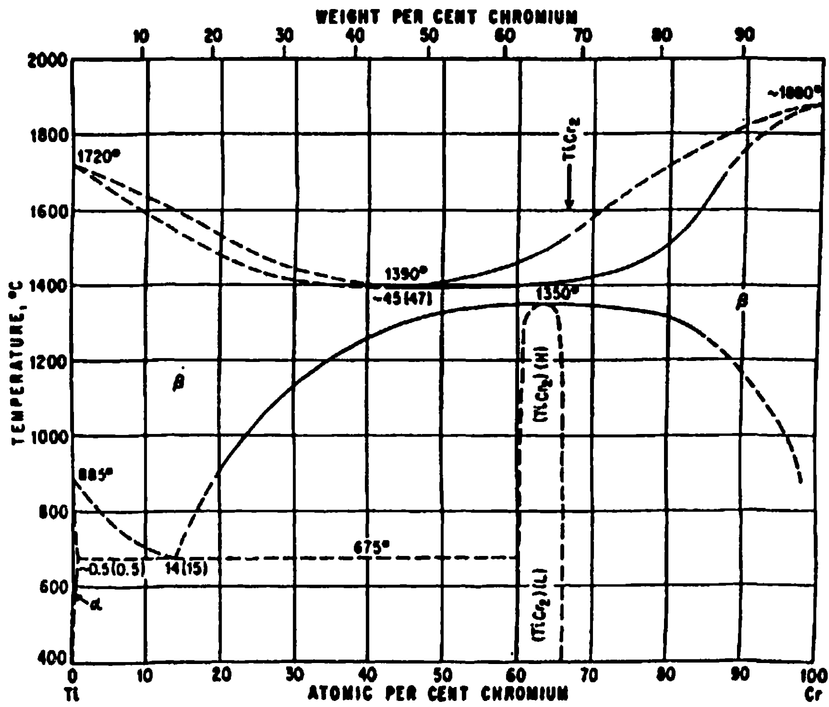

Figure 4.26 *Cr:Ti phase diagram reproduced from Hansen, M. (1958) Constitution of Binary Alloys. McGraw-Hill Book Company, New York with kind permission of The McGraw-Hill Companies.*

If low-loss spectra from this region and from pure Ti and Cr are compared, as in figure 4.27a, it can be seen that there are significant differences in the position of the first plasmons. Table 4.4 lists values for the position of the Ti and Cr plasmons quoted in the literature along with the experimental values obtained in this study. An alloy results in a single plasmon at an energy related to its composition (Williams and Edington, 1976) whereas two overlapping layers result in two distinct plasmon peaks at the correct energies. The energies of the Ti and Cr plasmons are sufficiently resolved that examination of this region of the energy loss spectrum in the Ti:Cr intermixed region should confirm whether it is an alloy or simply an artefact of specimen tilt resulting in overlapping layers. The Ti:Cr intermix plasmons are positioned between the Ti plasmon and the Cr plasmon and as the Cr content increases the plasmons shift towards a higher energy approaching the position of the Cr plasmon. Figure 4.27b shows the effect of summing the low-loss spectra from pure Ti and pure Cr compared to a spectrum collected from the point in the intermix where there are roughly equal amounts of Ti and Cr.

Table 4.4 *Position of first plasmon for Ti and Cr in energy loss spectroscopy.*

reference	Ti (eV)	Cr (eV)
present work	17.5	26.5
theoretical value, Egerton (1985)	17.8	26.8
Wehenkal et al (1974)	17.65	24.4
Misell et al (1973)	-	24.6
Robins et al (1960)	17.6	24.3

Coating 1 and 2

Figure 4.24 shows a distinct step in the coating composition going from region C1 to C2. Comparison of the N edge in spectra from regions C1 and C2 shows

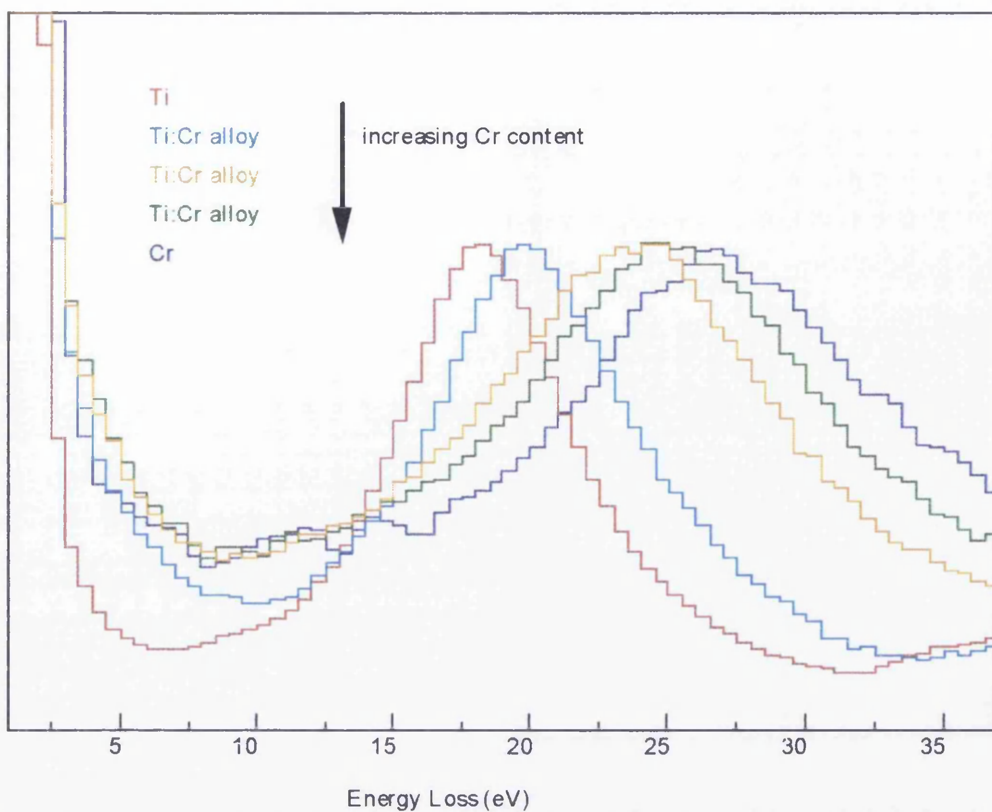

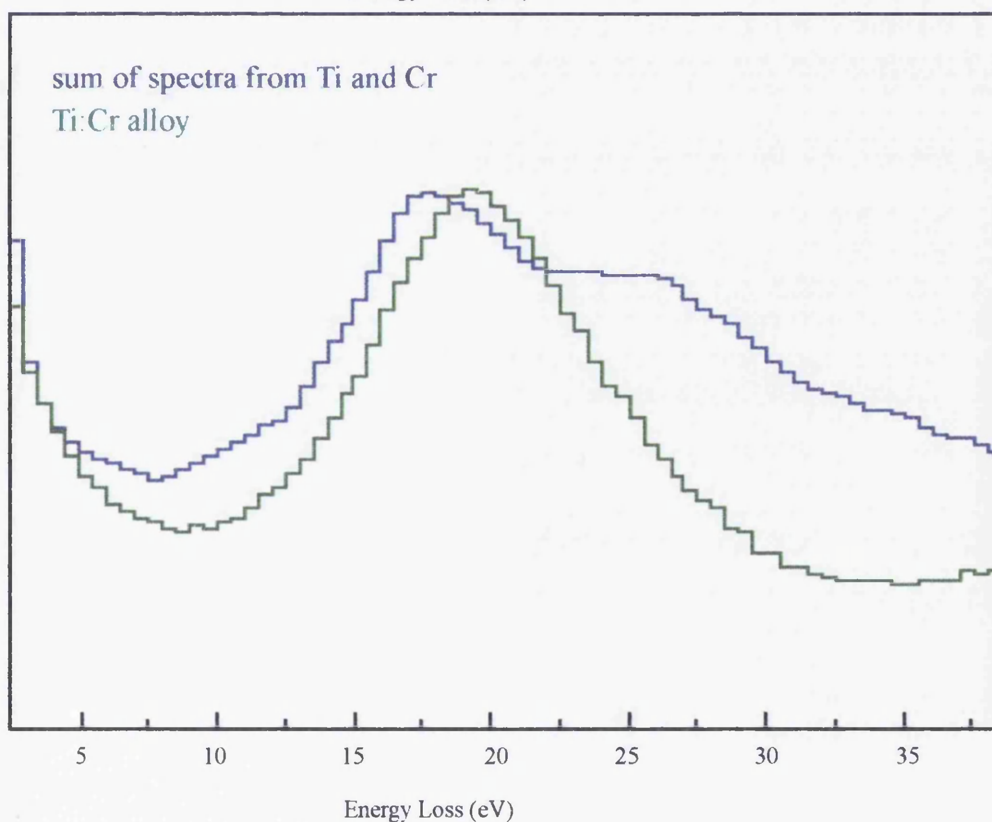

Figure 4.27a *First plasmon in electron energy loss spectra from Ti, Cr and Ti:Cr alloys of graded composition.*

4.27b *First plasmon in Ti:Cr alloy of roughly 1:1 composition and sum of first plasmons from Ti and Cr.*

a distinct change in shape of the fine structure for the two regions. If these spectra are compared with spectra from CrN and Cr_2N powder standards, as in figures 4.28 and 4.29, then it can be seen that the ELNES on the N K edge in C1 matches that of the Cr_2N powder standard indicating that they have the same structure. Analogously C2 can be said to have the same structure as the CrN standard. The structure of the Cr_2N and CrN standards were confirmed by X-ray diffraction to be the Cr_2N hexagonal and CrN face centred cubic (fcc) structures. The lattice parameters for these structures are given in table 4.9 (page 75). Diffraction work performed on this specimen to try to confirm these structures will be discussed in section 4.6.

Looking at figure 4.24 it can be seen that the Cr-N ratios in regions C1 and C2 are higher than expected for stoichiometric CrN and Cr_2N. The coating can be seen to be sub-stoichiometric and, taking the standards as stoichiometric, it has compositions of $Cr_2N_{0.6}$ and $CrN_{0.6}$ in regions C1 and C2, respectively. The composition of region C2 is likely to be the steady state composition achieved by the system as the profile appears to be level.

Figure 4.24 also shows an interpenetration of Ti into region C1 for about 12nm. This tailing is unlikely to be an artefact due to tilt as the estimated error in the orientation of the specimen for microanalysis is an order of magnitude smaller. This suggests that the Ti is substituting into the coating in region C1. Further evidence in support of such substitution is provided in figure 4.34 which is discussed below.

The other EELS line profiles are shown in figures 4.30-4.34. Initially the thicknesses of the different layers in each sample will be discussed. The accuracy with which these thicknesses are measured depends upon the plane of the interface being tilted parallel to the incident electron beam so the deviation in the tilt from this ideal condition will be estimated. The stoichiometries of the coatings will then be considered.

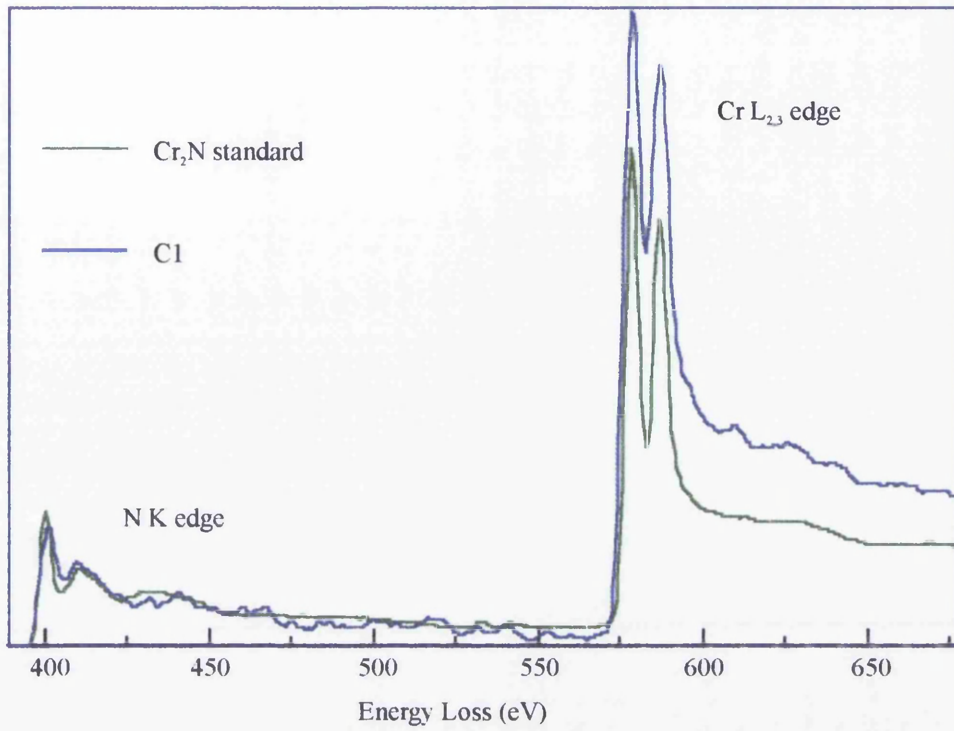

Figure 4.28 *EELS spectra from Cr_2N standard and region C1.*

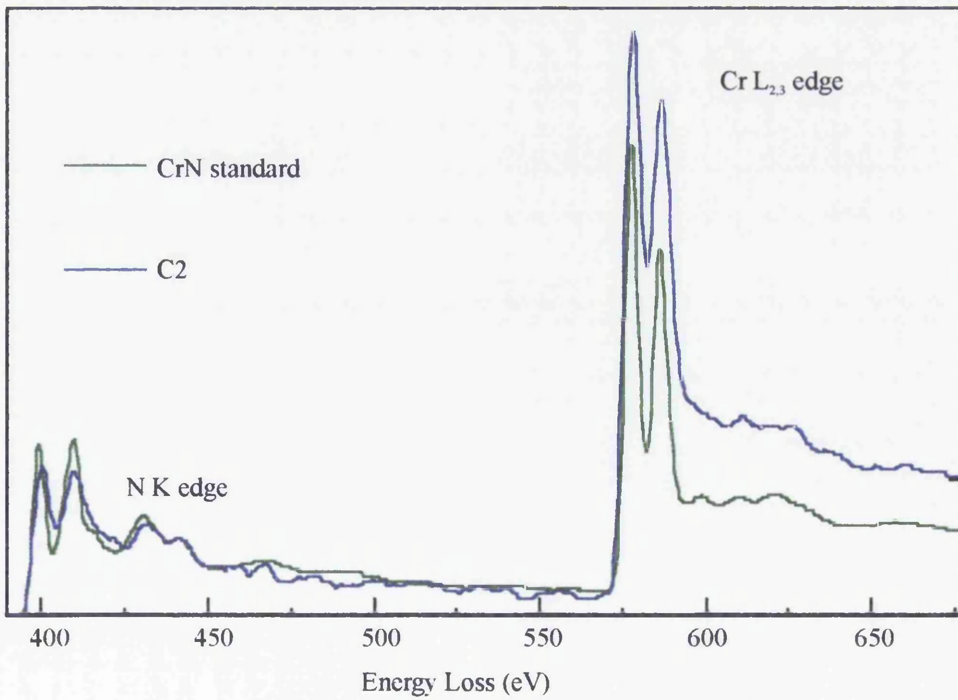

Figure 4.29 *EELS spectra from CrN standard and region C2.*

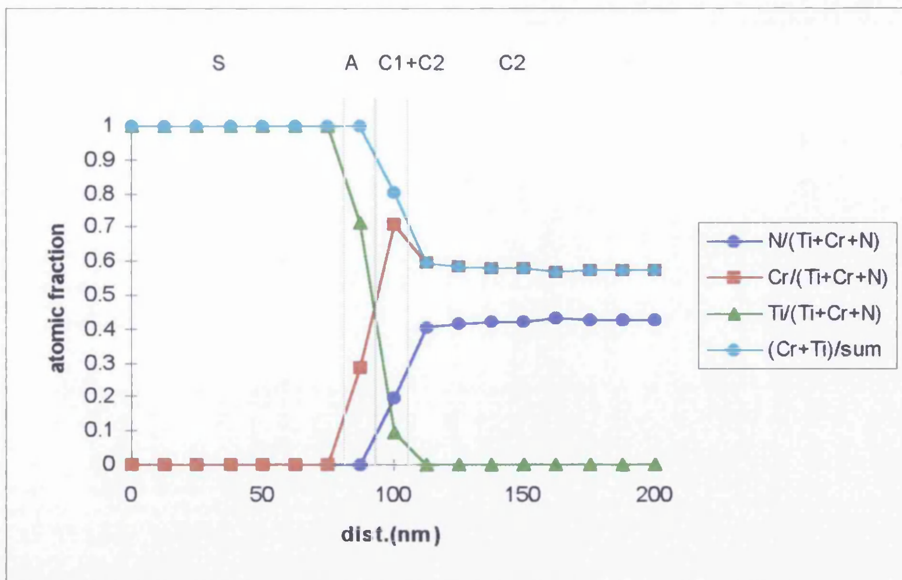

Figure 4.30 *EELS line profile of parallel -70V sample.*

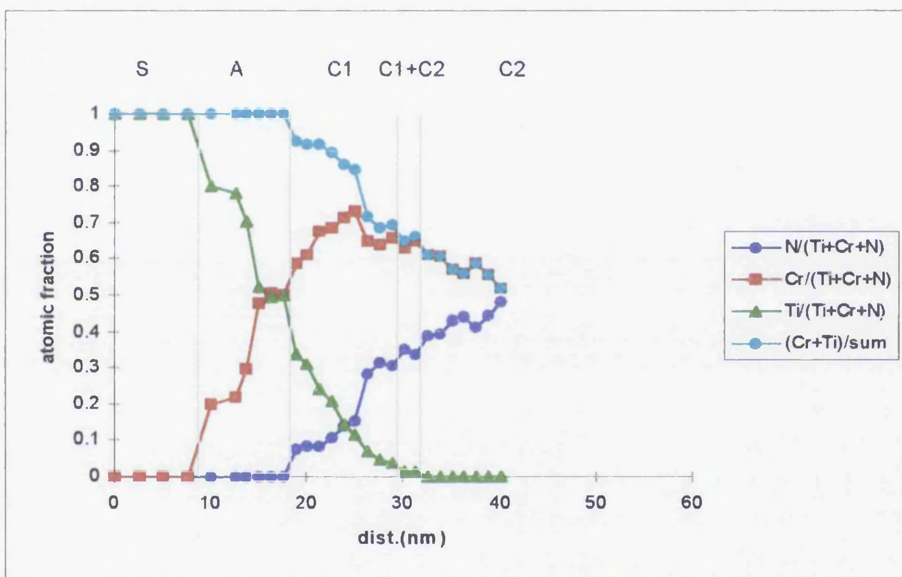

Figure 4.31 *EELS line profile of 45° -70V sample.*

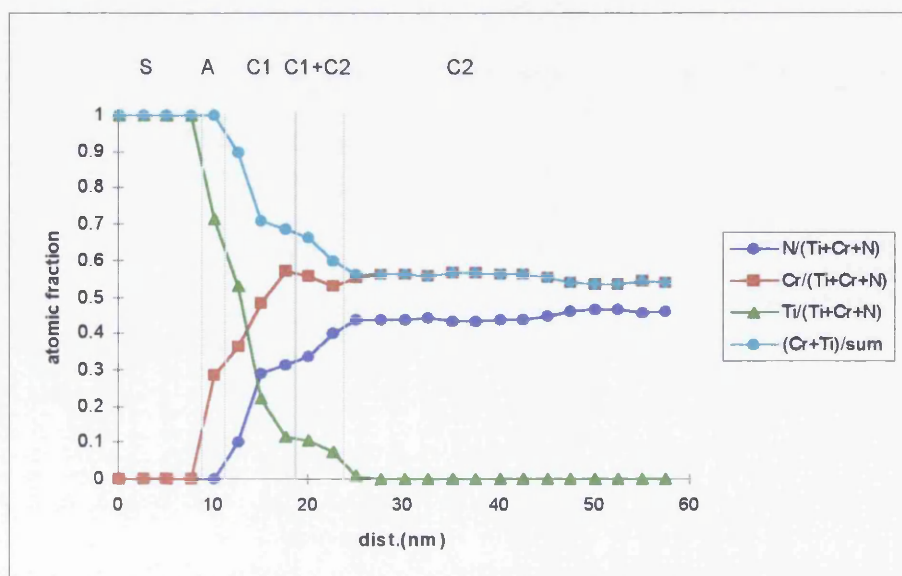

Figure 4.32 *EELS line profile of perpendicular -70V sample.*

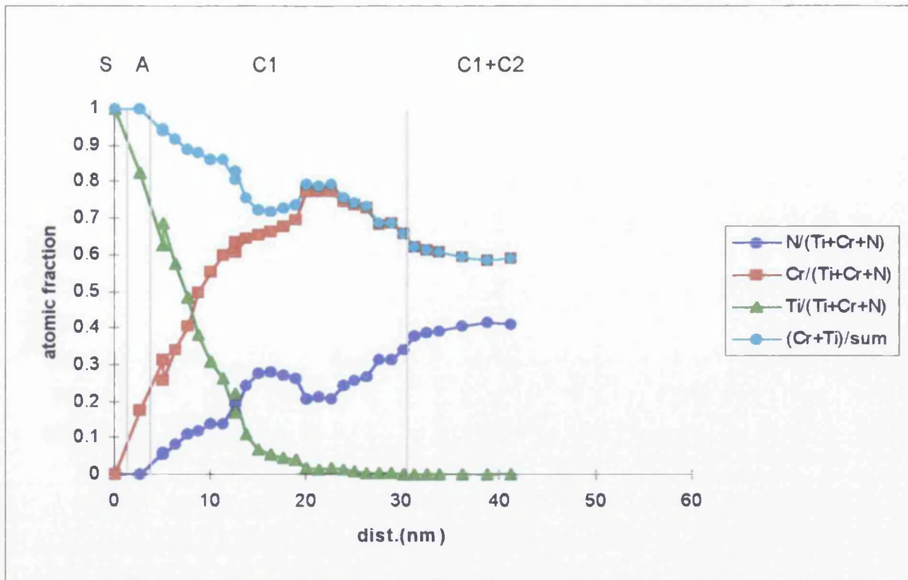

Figure 4.33 *EELS line profile of 45° -200V sample.*

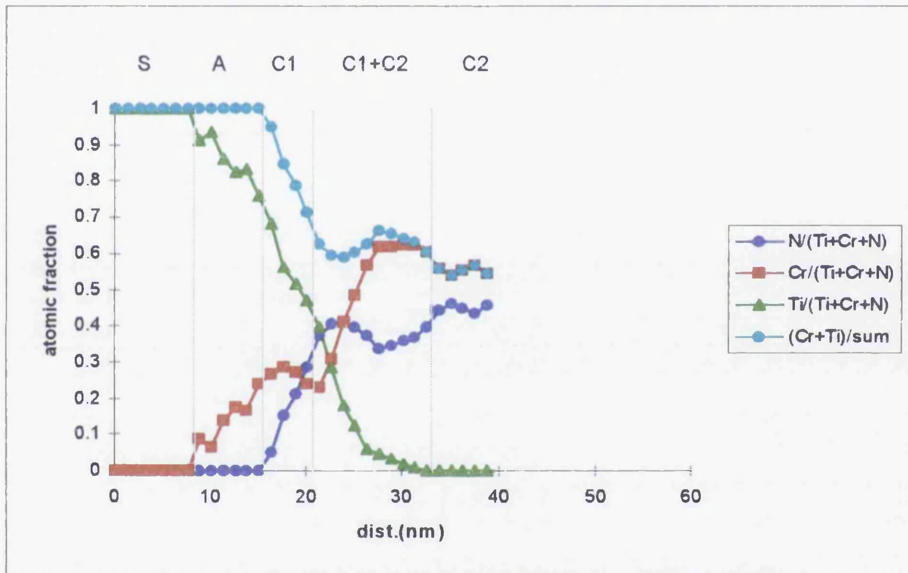

Figure 4.34 *EELS line profile of perpendicular -200V sample.*

The widths of the Ti:Cr alloy and the Cr_2N layers were measured for each sample from the EELS line profiles. The alloy width was taken to be the distance over which Cr and Ti were detectable in the EELS spectra without the presence of N. The Cr_2N layer width was calculated by taking the distance between the onset of the N signal and the point where the N K edge shape began to deviate from that of the Cr_2N structure. In all of these profiles the shape of the N K edge changed from that of the Cr_2N structure to that of the CrN structure over more than one step suggesting that the specimens were not tilted with the surface normal perpendicular to the electron beam at the time of analysis. The width over which this change in shape occurred was calculated by examining the ELNES on the N K edge. This region has been labelled C1+C2 because it is assumed to be an overlap region between C1 and C2.

Figure 4.30 is the EELS line profile for the -70V parallel sample. The Ti:Cr alloy region is 12.5nm wide. The width of C1 is assumed to be less than the step size (i.e., the distance between consecutive analysis points) of 12.5nm as it was not detected. A C1+C2 region 12.5nm wide was measured.

The composition profile for the -70V 45° sample is shown in figure 4.31. The Ti:Cr alloy is 8.75nm wide and the C1 layer 11.25nm. The C1+C2 region stretches for 2.5nm.

A line profile taken on the -70V perpendicular sample is illustrated in figure 4.32. The layer thickness are 2.5nm and 7.5nm for the alloy and C1, respectively. C1+C2 is 5nm wide.

The -200V 45° sample profile in figure 4.33 looks badly tilted as there is no sharp onset but rather a gradual increase in the N signal over at least 7.5nm. C1+C2 extends for at least 11.25nm with the line trace not extending far enough to detect region C2. The alloy has a width of 2.5nm.

The final line profile, in figure 4.34 is for the -200V perpendicular sample. The alloy is 7.5nm thick. Region C1 is 5nm wide and C1+C2 stretches for

12.5nm. The width over which the N signal increases is similar to the width of region C1+C2.

These layer thicknesses are summarised in table 4.5 below along with the step size. The uncertainty in the layer thickness as a result of the step size is also given. There will also be an error as a result of the positioning of the probe during collection of the data. This error was estimated to be about ±4nm for a step size of 12.5nm and of the order of ±0.7nm for the smaller step sizes. Drift of the specimen during acquisition of the data was not thought to significantly contribute to the uncertainty in these data sets. Other factors which might also contribute to an uncertainty in these values such as the probe size, the image resolution and image interference were also estimated to be smaller than the uncertainty resulting from the step size.

Table 4.5 *Width of Ti:Cr alloy and Cr_2N layers from EELS line profiles.*

substrate bias	orientation	step size (nm)	uncertainty due to step size (nm)	**A** Cr:Ti alloy (nm)	**C1** Cr_2N (nm)	**C1+C2** Cr_2N+CrN (nm)
-70V	0°	12.5	8.8	<12.5	-	<12.5
-70V	45°	1.25	0.9	8.75	11.25	2.5
-70V	90°	2.5	1.7	2.5	7.5	5
-200V	0°	1.62	1.1	16.2	17.82	1.62
-200V	45°	1.25	0.9	≥2.5	25	11.25
-200V	90°	1.25	0.9	7.5	5	12.5

Looking at the width of the alloy layers in table 4.5 it can be seen that for the -70V cycle the width of the alloy layer decreases as the angle between the substrate surface and the cathode surface increases. One would expect the penetration of Cr into the substrate to decrease as the orientation increases for the following reason. The energy of the ions arriving at the substrate is independent of the angle of orientation of the substrate to the cathode because

the potential difference through which the ions are accelerated is the same in each case. However, the ions are emitted from the cathode with a general forward directionality (Tuma et al, 1978) and the number of ions arriving at the substrate decreases as the angle of orientation of the substrate surface to the cathode surface increases. Also the ions are more likely to graze the surface of the substrate than to directly bombard it as the angle increases. However, it is important to remember that the width of the layer is non-uniform along the interface. Therefore, these results have to be compared with other profiles on the same samples before any firm conclusions can be drawn.

Comparison of the width of the alloy layers in the -200V samples is not so straightforward. This is possibly because of poor orientation of the 45° sample making the interpretation of the layer thicknesses difficult and giving ambiguous results.

Ignoring the -200V 45° sample, the width of the C1 layer also decreases as the orientation increases. This is the sample in which the CrN coating thickness also appeared to be somewhat anomalous.

Table 4.6 contains the estimated errors in the tilt during microanalysis for each line profile. These were obtained by calculating the specimen thickness at the point of analysis from the low-loss spectra, assuming an electron mean free path of 100nm, and using the width over which the N onset occurred to estimate the deviation in the tilt. This width along with the width of region C1+C2 is tabulated in table 4.6. Both widths are commensurate indicating that they are probably an artefact of tilt rather than a real chemical distribution.

The estimated tilt for the 45° -200V sample is probably a local rather than a global tilt effect.

These estimated tilt deviations can be used along with the thickness of the specimens calculated from the low-loss spectra to extract the layer thicknesses which would have been measured had the orientation of the specimen in the

electron beam been ideal. However, even if these calculations are done C1 is still thicker on the -200V 45° sample than on the -200V parallel one. The C1 thickness and the total coating thickness (table 4.3) for the 45° -200V sample are consistent with each other, suggesting that this sample received a thicker coating than expected. This is possibly because of its rotation during the coating process or else the other -200V specimens were prepared from parts of the samples which had been shadowed from the cathode by the clamping rings holding them in place on the copper block.

Table 4.6 *Estimated tilt errors during EELS microanalysis.*

substrate bias	orientation	step size (nm)	C1+C2 (nm)	N onset (nm)	estimated thickness (nm)	tilt error
-70V	0°	12.5	<12.5	<12.5	138	<5°
-70V	45°	1.25	2.5	>1.25	73	>1°
-70V	90°	2.5	5	5	100	3°
-200V	0°	1.62	1.62	1.62	116	0.8°
-200V	45°	1.25	11.25	>7.5	40.8	>10°
-200V	90°	1.25	12.5	7.5	95.8	4°

It was noted above that the coating in the -200V parallel sample is sub-stoichiometric in both regions C1 and C2. This observation is borne out by the line profiles in figures 4.30-4.34. The N:Cr ratios in the coatings achieved in region C1 were calculated by averaging over the points on the profile where the N:Cr ratio was relatively uniform just before the onset of region C1+C2. The N:Cr ratio in region C2 was also calculated by averaging over the uniform part of the profile after the termination of region C1+C2. These ratios are listed in table 4.7. Also listed are the standard deviations calculated in the average ratios tabulated. Only one data point was available in region C1 for the -70V 0° sample so the standard deviation was not calculated.

Table 4.7 *Nitrogen to chromium ratios in the coatings.*

substrate bias	orientation	step size (nm)	C1 N/Cr	C1 standard deviation	C2 N/Cr	C2 standard deviation
-70V	0°	12.5	0.27	-	0.73	0.01
-70V	45°	1.25	0.46	0.01	0.75	0.03
-70V	90°	2.5	0.57	0.02	0.81	0.01
-200V	0°	1.62	0.33	0.01	0.56	0.02
-200V	45°	1.25	0.46	0.04	-	-
-200V	90°	1.25	0.67	0.08	0.80	0.02

Table 4.7 shows that the N:Cr ratio of the coating does not appear to be uniform for a given substrate bias or orientation and increases with orientation. The differences in the ratios are considerably larger than the standard deviations and are therefore likely be real rather than statistical fluctuations. Such differences are unlikely to result from changes in the alignment of the microscope as data collected from a standard sample using various convergence and collection angles had a similar standard deviation to the data in table 4.7. The differences are probably a result of differences in the relative numbers of metal and nitrogen ions arriving at the substrate surface with relatively fewer metal ions reaching the substrate surface as the angle of orientation increases and therefore the nitrogen to metal ratio increases. The metal ions are emitted mainly perpendicular to the cathode surface (Tuma et al, 1978). Higher gas pressure in the chamber during deposition should influence the composition by increasing the uniformity via increased gas scattering which leads to a more uniform distribution of metal ions in the chamber as well as increasing the N:Cr ratio because of the increased number of nitrogen ions. Vyskocil and Musil (1990) note the difficulty of depositing coatings of a uniform stoichiometry on complex-shaped substrates stating that this is the reason why most industrial deposition systems usually work in a regime of saturation depositing almost stoichiometric coatings. However, increasing the

gas pressure to increase gas scattering can also have detrimental effects with a decrease in the effectiveness of the arc source (Matthews, 1985) due to cathode poisoning (Hovsepian and Popov, 1994).

However, the N:Cr ratio of the planar sample discussed earlier (page 62) was not uniform either. The minimum and maximum N:Cr ratio values observed in the line profile across the grain boundary in planar section were 0.60 and 0.76 showing the order of magnitude of fluctuations one could expect in the ratios within the coating on a single specimen.

In the literature it is stated that Cr_2N is stable from about $Cr_2N_{0.76}$ to Cr_2N (Eriksson, 1934). Considering the N:Cr ratio of the coating in region C1 for each sample, as listed in table 4.7, it is observed that the values for the parallel samples are lower than the lower limit of stability. This is probably because the system is not in thermal equilibrium.

The N:Cr ratios of the perpendicular samples in region C1 are also anomalous. These values are higher than the upper limit of stability quoted above. If figure 4.34, which shows the line profile for the -200V perpendicular sample, is examined the coating appears to be hyper-stoichiometric in part of C1. However, the graph also indicates the presence of Ti in this section. This provides further evidence for the incorporation of Ti into the Cr_2N lattice rather than the signal just being an artefact of tilt.

The N:Cr ratio in region C2 appears to level off in each case apart from in the 45° -70V profile in figure 4.31 where it increases with distance. This is the only data set which exhibits this behaviour of a continued increase in the N concentration with distance. The corresponding ADF image showed that the CrN grain in which the analysis took place was non-columnar suggesting that this was an atypical piece of specimen.

The ELNES on the N K edge has already been used to identify the crystal structure in the coating. The ELNES on the Ti and Cr $L_{2,3}$ can also be used to look at changes in composition along the line profiles.

Comparing Ti $L_{2,3}$ edges (figure 4.35) moving from pure substrate through the graded Ti:Cr alloy and into the coating there is a gradual increase in the height of the white lines relative to the rest of the edge. This suggests that the Ti is donating electrons to the other species, resulting in increased vacancies in the d-bands, transitions to which are responsible for the white lines.

The shape of the Cr $L_{2,3}$ edges also changes along the line profile. The height of the white lines relative to the rest of the edge increases as the N content increases (fig 4.36) moving from the Ti:Cr alloy into the C1 coating. This is because the metal donates electrons to the N resulting in more vacancies in the metal 3d shell. The intensities of the white lines compared to the rest of the Cr edge is greater in the nitride than in the Ti:Cr alloy. The white line intensities relative to the rest of the edge continue to increase moving from region C1 into C2.

The remainder of this section discusses briefly some EDX line profiles that were obtained from the samples before summarising the observations.

The thicknesses of the Ti:Cr alloy layers in some of the samples were estimated from EDX line profiles. Table 4.8 summarises the thicknesses obtained from these profiles estimated by drawing a tangent on the steepest part of the line profile and measuring where it cuts the mean initial and final concentration ratios. However, because the N concentration is not determined by the EDX data, it is difficult to be sure of the interpretation and so the widths in table 4.8 cannot be directly compared with those in table 4.5.

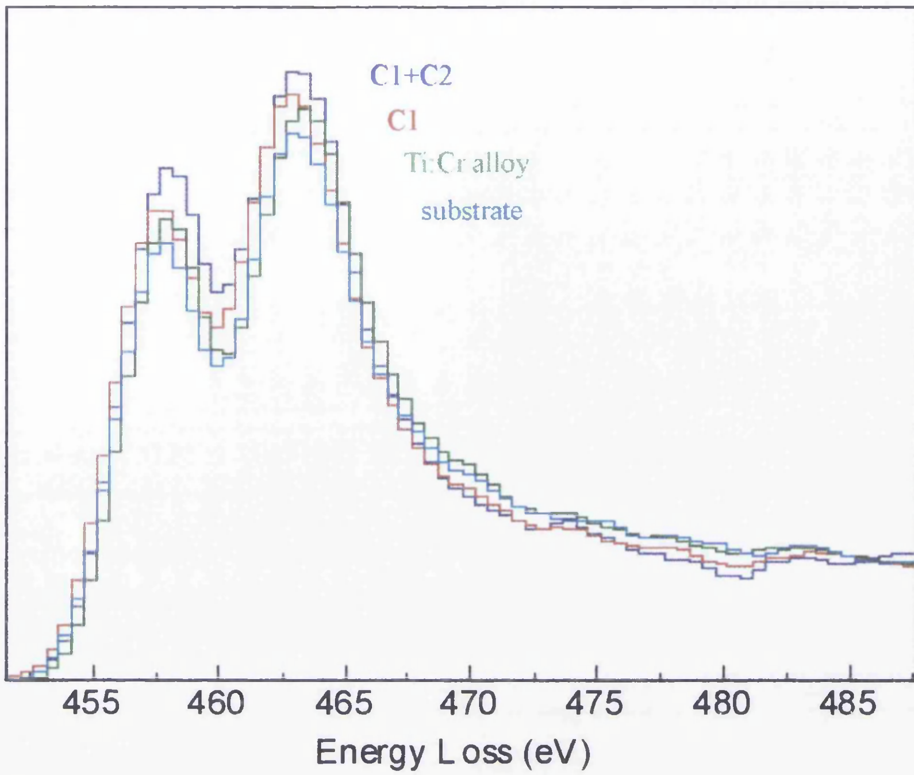

Figure 4.35 *White lines in Ti $L_{2,3}$ edge.*

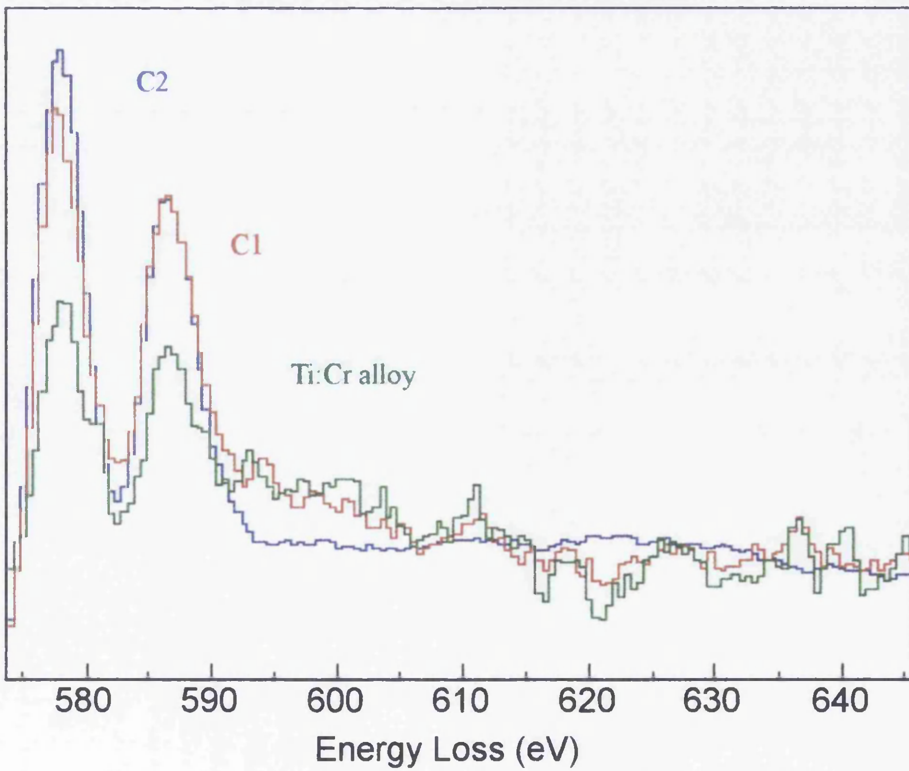

Figure 4.36 *White lines in Cr $L_{2,3}$ edge.*

Table 4.8 *Width of the Ti:Cr alloy layer from EDX line profiles.*

substrate bias	orientation to cathode	width (nm)
-70V	0°	18.4, 15.18, 16.6, 22.8, 18, 20.3
-70V	45°	-
-70V	90°	13.5
-200V	0°	19.8, 22.5, 20.1. 18.1, 22.9
-200V	45°	10.7, 16.7, 5.67
-200V	90°	-

The data in tables 4.5 and 4.8 imply that the interface width decreases as the angle of orientation between the substrate surface and the cathode increases. However, it must be remembered that the interface width is non-uniform. The substrate bias does not appear to have affected the width of the Ti:Cr layer noticeably. This is because the substrate bias is a coating parameter and the Ti:Cr layer is a result of the sputter cleaning process.

In summary, the thicknesses of the interface layers measured via EELS and EDX line profiles are comparable to the thicknesses observed in the bright and dark field images in section 4.4. The width of the interface decreases as the angle between the substrate surface and the cathode increases. Chemical analysis has identified the interface layers as a layer of Ti:Cr alloy of graded composition and a layer of sub-stoichiometric Cr_2N. The structure of the Cr_2N layer was determined by the ELNES on the N K edge in the EELS data. The different structures of the two interface layers which are both fine grained are highlighted by the contrast in the bright and dark field imaging. However, the actual structure of the Ti:Cr alloy has not yet been determined. The next section looks at a more formal study of the crystallographic structures present using diffraction techniques. One of these coated samples and the uncoated sample are studied.

4.6 Diffraction

Table 4.9 lists the possible lattice structures and their lattice parameters which might be expected in the substrate, coating and interfacial region. CrN has the rock salt structure. Blix (1926) suggested a close packed hexagonal array for the Cr atoms in Cr_2N with lattice parameters a=2.747Å and c=4.439Å and the N atoms as interstitials. However, Eriksson (1934) determined the structure of the Cr_2N lattice to have an ordered array of N best described by a larger hexagonal unit cell with lattice parameters a=4.8113Å and c=4.4841Å.

Table 4.9 *Lattice parameters of materials of interest.*

material	lattice	a (Å)	c (Å)	reference
α-Ti(6%Al,4%V)	hcp	2.927	4.668	Ward-Close (1982)
β-Ti(6%Al,4%V)	bcc	3.232	-	Ward-Close (1982)
α-Ti	hcp	2.95	4.68	Edington (1975)
Cr	bcc	2.88	-	Edington (1975)
CrN	fcc	4.149	-	Goldschmidt (1967)
CrN	fcc	4.140	-	Pinsker and Abrosimova (1958)
Cr_2N	hcp	4.805	4.479	Goldschmidt (1967)
Cr_2N	hcp	4.8113	4.4841	Eriksson (1934)

Figure 4.37 shows diffraction patterns calculated by the computer program Diffract for some of the expected crystallographic structures listed in table 4.9. These were used in the interpretation of the experimental diffraction patterns.

Examination of phase changes across the interface is a difficult problem in view of

i) the small grain size

ii) the narrow layer widths

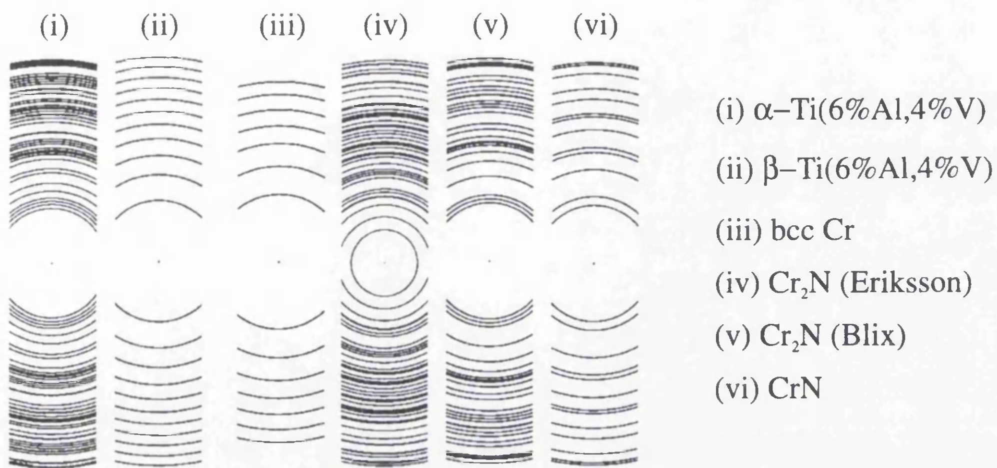

Figure 4.37 *Ring patterns calculated using Diffract.*

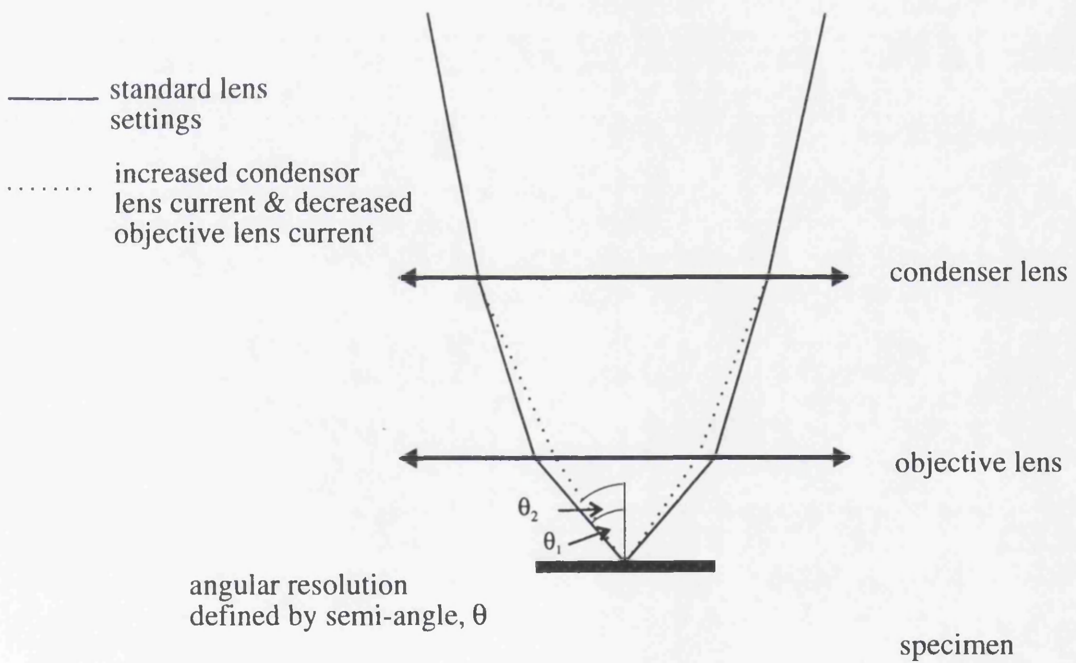

Figure 4.38 *Changing the angular resolution.*

iii) the non-planar nature of the interface and

iv) the similarity of the ring patterns

Therefore, two approaches were used

i) single crystal patterns and

ii) patterns averaged over an area

The standard selected area diffraction technique proved useful in giving average diffraction patterns from planar specimens. By selecting an area right on the edge of the specimen, it proved possible to get information on the surface layer. The single crystal approach required a small probe with the associated large convergence angle e.g., 1nm diameter probe implies 5mrad angular diameter. This worked quite well in the coating and the substrate but less well in the interface layers where the grain size was very small.

An alternative method to obtain average diffraction patterns from small areas was thus required. This was implemented by modifying the optics of the standard high resolution scanning mode of the Philips CM20 microscope. Figure 4.38 shows the standard optics plus the weakening of the objective lens current and the strengthening of the second condenser lens to get a bigger probe diameter but a smaller convergence angle. It is possible to get a 3nm probe with an angular diameter of ~1.5mrad. The probe diameter allows the individual layers to be resolved while the angular resolution allows the (110), (111) and (200) rings to be separated in the cubic diffraction patterns. Such a probe can either be stopped at a point on the specimen or scanned across a well defined rectangular area whose orientation and dimensions can be controlled by the scanning unit.

In practice, it is essential to use a cross-grating specimen when setting up the mode in order to ensure that

i) the scan rocking points are set correctly to give the same magnification in orthogonal directions and

ii) the diffraction stigmator is correctly set to give round rings from a stress free specimen

In practice, one can only approximate each condition.

Several attempts were made to use diffraction techniques on the cross-section specimen from the -200V parallel sample discussed in the previous section. This was done to try and determine the crystallographic structures and lattice parameters of the different layers observed in bright and dark field imaging and in the chemical analysis. A planar specimen from the sample which had been sputter cleaned with Cr but not coated (table 4.1), was also investigated.

In spite of the proximity of the rings for the possible structures making this experiment difficult some results were obtained.

The objective lens current was weakened from 4600 to 4000mA and the image focus was corrected using the second condenser lens. The polycrystalline diffraction pattern from the PaAu coating on the cross-grating was used to calibrate the camera length of the microscope and to correct astigmatism in the diffraction lens. Such astigmatism makes the diffraction pattern elliptical. A similar ellipticity can also be caused by stress in the coating. Therefore, the cross-grating provides a useful check on the astigmatism both in imaging and in diffraction modes before examining the cross-section specimen.

Initially this experiment was performed by averaging the diffraction pattern over an area of specimen which was defined by making the region of specimen scanned rectangular. The size of this rectangle was optimised to scan over as large a region as possible within a single layer. It was hoped that using this technique, a diffraction pattern averaging over sufficient grains to obtain a polycrystalline ring pattern could be obtained. However, due to the non-flat interface and the narrow width of the interface regions limiting the area scanned ring patterns could not be obtained. The experiment was also performed with a stationary probe but, due to the small size and random

orientation of the grains in the interface layers, it was difficult to obtain single crystal spot patterns.

Figure 4.39 shows a set of diffraction patterns obtained by averaging over an area of specimen. The first pattern (figure 4.39a) is from a relatively large region of coating. This pattern is characteristic of an {022} texture normal to the substrate surface. Figure 4.40 shows the pattern overlaid with a simulated {022} texture pattern. An attempt was made to identify the orientation of the interface relative to the diffraction pattern by defocusing the illumination and recording a shadow image but unfortunately this was overexposed. However, the orientation determined from the sketch recorded in the laboratory book is shown. X-ray diffraction data from other samples of CrN not discussed in this thesis gave {002} texturing for deposition on Si and {022} texturing for deposition on steel (Aharonov et al, 1993).

The pattern (figure 4.39b) obtained averaging over a smaller region of coating nearer to the interface also fits to the CrN ring pattern with unaccounted arcs/spots fitting to the Cr_2N ring pattern. The spots in the pattern were not indexed.

Two different diffraction patterns shown in figures 4.39c and 4.39d were obtained from the interface region. The α-Ti(6%Al, 4%V) and β-Ti(6%Al, 4%V) ring patterns do not fit these diffraction patterns so it can be categorically stated that they are not from the substrate. The Cr_2N (Eriksson, 1934) pattern does fit but this may just be because there are lots of rings. The ring like nature of the diffraction pattern from this region shows that the grain size is very small here compared to the grain size in the coating and in the substrate.

The substrate diffraction pattern (figure 4.39e) was not indexed because the spacing between the spots varied in different parts of the pattern. It looks as if the crystal was off orientation and some higher order reflections were picked up.

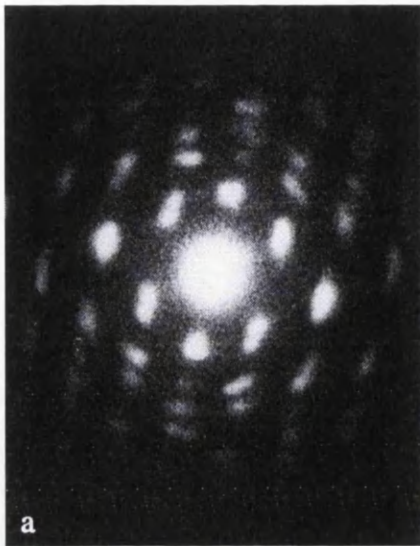

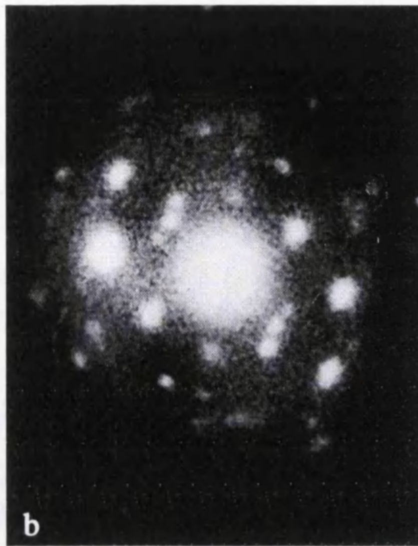

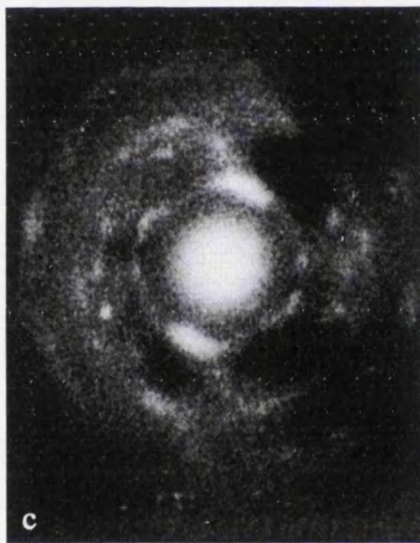

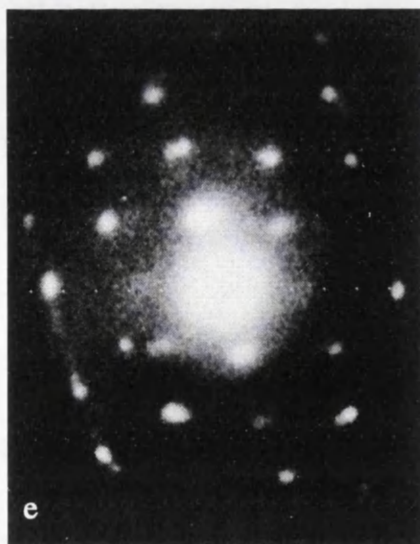

a larger region of coating away from interface
b coating
c interface
d base of interface region
e substrate

Figure 4.39 *Line scan diffraction sequence across interface..*

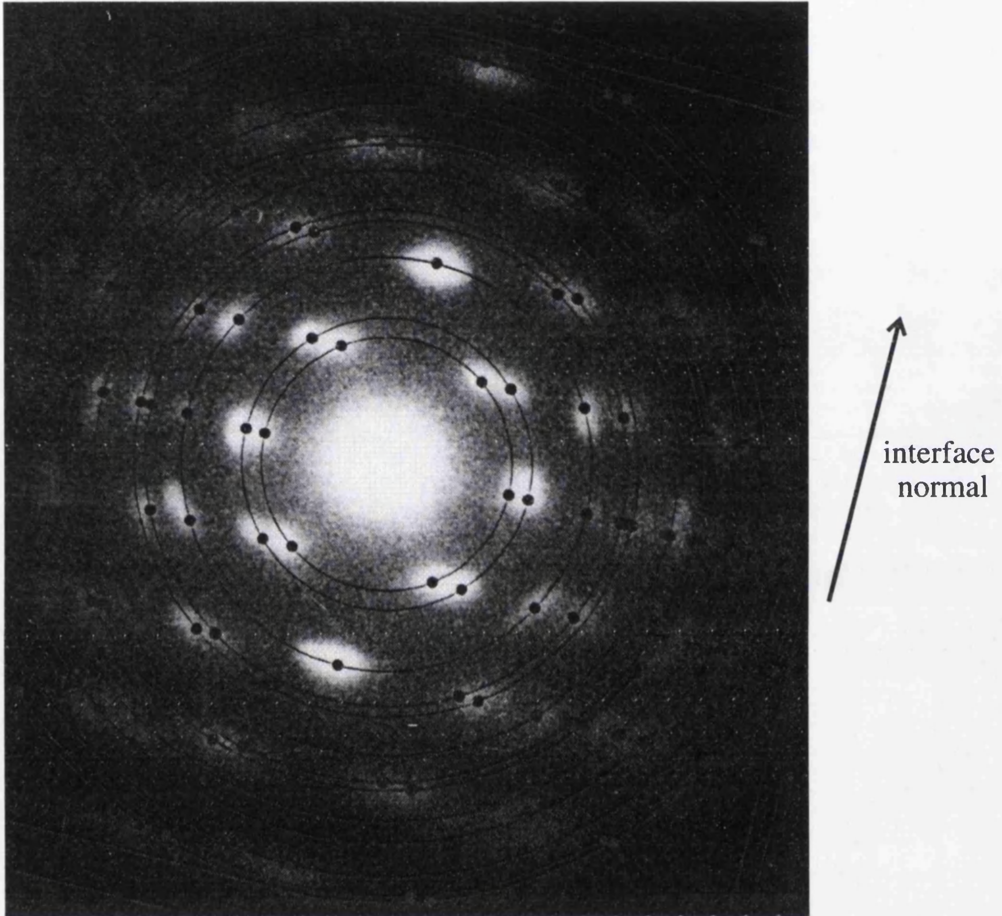

Figure 4.40 *Diffraction pattern obtained scanning over region of coating. Superimposed is a {022} texture pattern.*

The above diffraction sequence has given some evidence for the presence of the Cr_2N phase. However, it has not established the presence of bcc Ti:Cr at the interface.

A planar specimen of the same material which was sputter cleaned but not coated was examined by taking diffraction patterns from single grains and from selected areas, averaging over lots of grains. As the thickness of the specimen increases any bcc patterns from the surface will quickly be masked or confused by the addition of hcp patterns from the bulk substrate. Therefore, thin regions near the edge of the hole were used. In addition to β-(Ti:Cr), there is also the possibility that there will be some β-Ti(6%Al, 4%V) present at the surface as the substrate retains a small quantity of β-phase.

Most of the selected area diffraction patterns, such as the one shown in figure 4.41a, contained more than one phase. One incomplete diffraction pattern shown in figure 4.41b was obtained from the very edge of the specimen where it is likely that only the alloy layer was present. These rings were indexed as a bcc pattern with a lattice parameter of 2.97±0.06Å. This value is in between the value expected for either pure β-Ti(6%Al,4%V) or pure bcc Cr given in table 4.9. This suggests a bcc alloy with a Cr-Ti ratio of 0.257±0.005. The rings in this pattern are also present in the pattern in figure 4.41a. The other rings in figure 4.41a indexed as hcp Ti(6%Al,4%V).

Diffraction patterns from individual grains were also taken. Figure 4.42a shows an example of a hexagonal diffraction pattern obtained. Most of the single grain diffraction patterns indexed as hcp Ti(6%Al,4%V) patterns giving average lattice parameters of a=2.96±0.06Å and c=4.65±0.09Å. One diffraction pattern, shown in figure 4.42b indexed as bcc Ti(6%Al,4%V) with a lattice parameter 3.22±0.06Å.

In summary, there is some diffraction evidence for the presence of CrN, Cr_2N, α-Ti(6%Al,4%V) and β-Ti(6%Al,4%V). There is also some evidence for the

presence of a bcc Ti:Cr alloy. The main difficulty with the diffraction experiments was obtaining the required angular resolution to unambiguously differentiate between patterns while maintaining sufficient spatial resolution to clearly differentiate between the layers in imaging mode.

4.7 Conclusions

All of the coatings studied in this chapter have exhibited growth of sub-stoichiometric CrN on an interfacial region consisting of a metal alloy of graded composition followed by a sub-stoichiometric Cr_2N layer. The CrN coating grows with a columnar structure. Differences in the surface finish of the coating, grain size and width of the interfacial region have been observed for different deposition parameters. The surface structure of the coating is also influenced by the angle of the substrate during deposition. Deposition with the cathode surface parallel to and at 45° to the substrate surface results in a similar surface structure. However, deposition with the substrate surface perpendicular to the cathode surface gives a smoother coating. The substrate bias also affects the grain size and therefore growth with the grain size increasing as the substrate bias becomes more negative. There is also an increase in the grain size as the orientation of the substrate to the cathode increases.

The initial growth of sub-stoichiometric Cr_2N is probably a result of switching from sputter cleaning to coating with the change in composition between regions C1 and C2 likely to be due to variations in the partial pressure of the nitrogen gas as the system is changed from sputter cleaning to deposition. After sputter cleaning is complete, the substrate bias is reduced and nitrogen gas is introduced into the chamber. This is usually done manually and involves adjusting the pressure to the correct level while the substrate bias is varied to ensure stability. This typically takes between 30s and 2 minutes to perform. The deposition times for the coatings studied in this chapter were about 13-14

minutes. The Cr_2N accounts for roughly 5% of the total coating so it is not unreasonable to assume that it is a result of the changeover. During this changeover process, the cathode becomes poisoned i.e., the surface changes from being metal to nitride as N_2 gas is introduced into the chamber. Such poisoning causes a decrease in the emission rate of Cr. Thus, the emission of Cr is initially higher and there is less gas in the chamber so there is not enough N_2 gas to form CrN and the coating grows as sub-stoichiometric Cr_2N. As the gas pressure increases and the rate of Cr evaporation decreases, deposition of CrN becomes possible and the crystallographic structure changes. The coating then grows as columnar sub-stoichiometric CrN.

The compositions of the coatings are not uniform with the relative amount of Cr decreasing as the angle between the substrate and the cathode increases. There are also fluctuations of the composition within a given sample. Incorporation of Ti into the coatings was also observed. The mechanism for this is not clear but it is possibly a result of diffusion during the deposition.

The presence of a chromium-titanium alloy at the interface was observed. This is important because it is known that the presence of a $TiCr_2$ phase in β alloys of Ti can cause embrittlement (Polmear, 1981). The presence of this alloy suggests that there is some deposition of chromium during the sputter cleaning process with a small amount of evidence indicating that the Ti(6%Al, 4%V) has transformed to the β phase on the addition of Cr.

However, it is impossible to tell from this study whether the sputter cleaning process eroded any of the substrate because there is no way of determining the original substrate surface. The next chapter examines the effect of the sputter cleaning process in more detail using special substrates with clearly defined substrate surface positions.

CHAPTER 5

Investigation of the sputter cleaning process

5.1 Introduction

The sputter cleaning process is a conditioning pre-treatment which prepares the surface of the substrate for deposition. In practice, it is found to be necessary for good adhesion of the coating to the substrate.

It has been observed by others (Hatto et al, 1996) that the Ti sputtering of a Si wafer resulted in an amorphous layer at the coating/substrate interface. The layer consisted of a Si and Ti intermix of graded composition. This was found to have non-uniform thickness if the substrate surface was parallel to the cathode surface during the sputter cleaning process but uniform thickness if the surfaces were perpendicular to each other. If the sputtering process was continued a layer of α-Ti was also deposited. The uniformity of this layer also depended upon the relative orientations of the substrate and the cathode to each other. Similarly, an amorphous region of Fe and Ti was found at the interface of TiN on ASP steel after Ti sputter cleaning (Hatto et al, 1996). Crystalline regions at the interface have been observed in some systems. For example, Håkansson (1991) noted the presence of recrystallised zones at the interface between TiN and stainless steel.

All of the above observations confirm that the sputter cleaning process deposits material from the cathode. The nature of the resulting interfacial region depends upon the mutual solubility of the materials involved; Jiang et al (1995) note that formation of an amorphous phase in ion implantation was closely related to the structure and solubility range of compounds. If the materials are not soluble in each other then the interface region is amorphous; otherwise it is crystalline. If the sputter cleaning process is continued then a layer of the sputtering element is deposited on top of the graded intermix region.

In the last chapter, the Cr sputter cleaning of Ti(6%Al, 4%V) and the subsequent deposition of CrN resulted in a region of Ti:Cr alloy at the substrate/coating interface. However, it was impossible to tell whether the process was etching away any of the substrate because there was no way of determining the original position of the substrate surface. This chapter investigates the nature of the sputter cleaning process more closely by studying the sputter cleaning of two different substrates. Substrates were specially designed to allow the original substrate surface position to be determined.

Section 5.2 describes the samples examined in this chapter. It explains how the substrates were prepared and how the original substrate surface position can be determined. Section 5.3 considers the Cr sputter cleaning of a layer of Ti. The Ti sputter cleaning of TiN followed by deposition of TiN is investigated in section 5.4. Section 5.5 discusses the observations which are made in the chapter and the conclusions which can be drawn.

5.2 Description of samples

There are two substrates used for the samples discussed in this chapter. These were prepared on Si wafers. The sputter cleaning and deposition parameters

used in the preparation of these substrates are summarised in table 5.1a. The parameters for the subsequent sputter cleaning and deposition cycles to which the substrates were subjected are listed in table 5.1b.

Table 5.1a *Summary of sputter cleaning and deposition parameters for preparation of substrates on Si wafers.*

substrate to be deposited	angle of Si wafer to cathode	sputter cleaning cycle		coating cycle for deposition of substrate		
		ion	Amp hours	substrate bias (V)	coating	Amp hours
Ti	90°	Ti	10	-150	Ti	48
TiN	90°	Ti	10	-70	TiN	0.37
					NbN	0.5
					TiN	2.23
					NbN	0.5
					TiN	4.48

Table 5.1b *Sputter cleaning and coating parameters for treatment of substrates.*

substrate	motion of substrate	angle of orientation to cathode	sputter cleaning cycle		coating cycle	
			ion	Amp hours	substrate bias (V)	Amp hours
Ti	rotating	0°	Cr	10	-	-
TiN	stationary	0°,45°,90°	Ti	33	-250	2
TiN	rotating	0°,45°,90°	Ti	35	-250	6

The first attempt at this experiment was based on the premise that the original thickness of a layer of Ti on Si could be determined if a part of the wafer were capped with another element, namely Hf, without further sputter cleaning and was subsequently cross-sectioned. To this end a stationary Si wafer was sputter cleaned with Ti. A layer of Ti was deposited on the wafer at -150V in the presence of Ar with the surface of the wafer perpendicular to the cathode surface. The wafer was cleaved and part of it sputter cleaned with Cr for 17Ah while in rotation. Both pieces of the wafer were then capped with Hf to prevent erosion of the Ti and/or Cr during the ion milling process in the specimen preparation. A comparison of the pieces of wafers in both samples should allow determination of the quantity of Ti remaining as well as the amount of Cr layers.

However, the exact position of the original substrate surface could not be determined because the layer of Ti deposited was of non-uniform thickness. Therefore, the design was modified for the second substrate in such a way that the position could be determined from the re-cleaned sample alone. This was done by putting a known thickness of material between two marker layers and following the second marker layer by exactly twice the thickness of material. By the time this experiment came to be done, Multi-Arc were very concerned about the process of recoating an existing TiN coating which was unsuccessful unless the old coating was stripped off. Hence TiN was used as the substrate. It was sputter cleaned and a subsequent TiN layer deposited. The TiN substrate was prepared as follows. After sputter cleaning with Ti, a thin layer of TiN ~7nm wide was deposited onto a stationary Si wafer. The Si wafer surface was perpendicular to the cathode surface. This was followed by ~12nm of NbN as a marker layer, ~42nm of TiN and a second marker layer of NbN. A third layer of TiN twice as thick as the second was deposited by coating for twice as long. In this way the original surface position is clearly defined and can be identified by comparing the relative widths of the second and third TiN layers. Figure 5.1 shows a schematic diagram and a cross-sectional TEM image of these layers. An amorphous layer can be seen at the interface between the Si wafer and the first TiN layer. This is a Si:Ti intermix as observed by Hatto et al (1996).

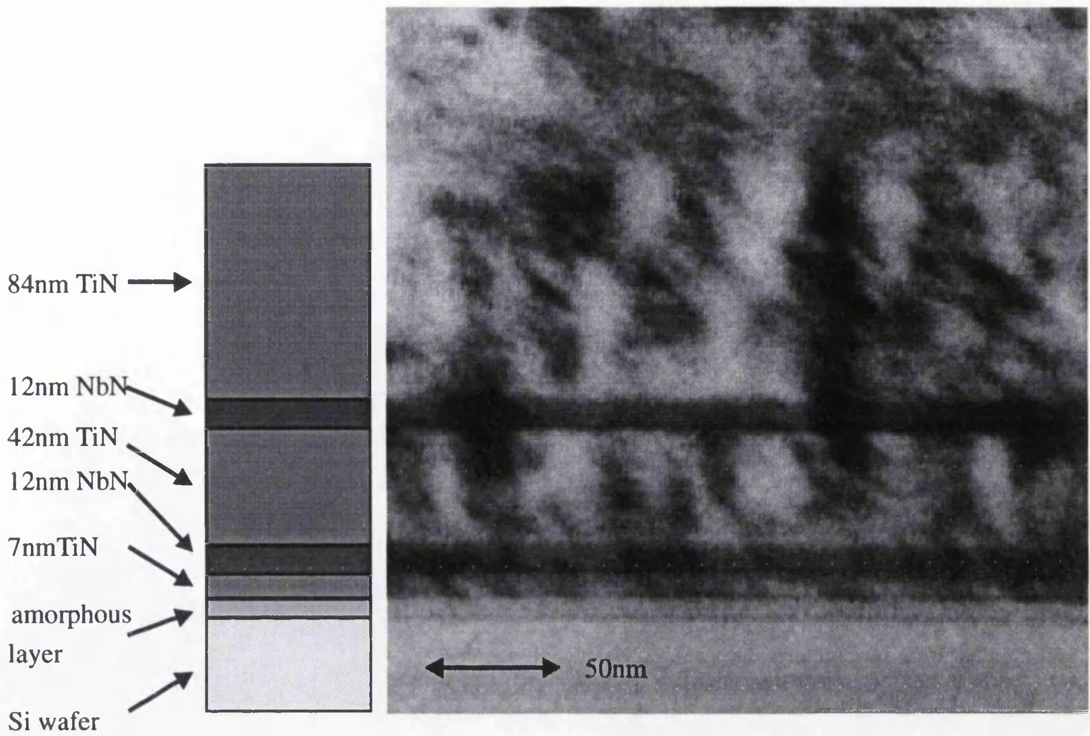

Figure 5.1 *Special substrate to allow determination of original substrate surface.*

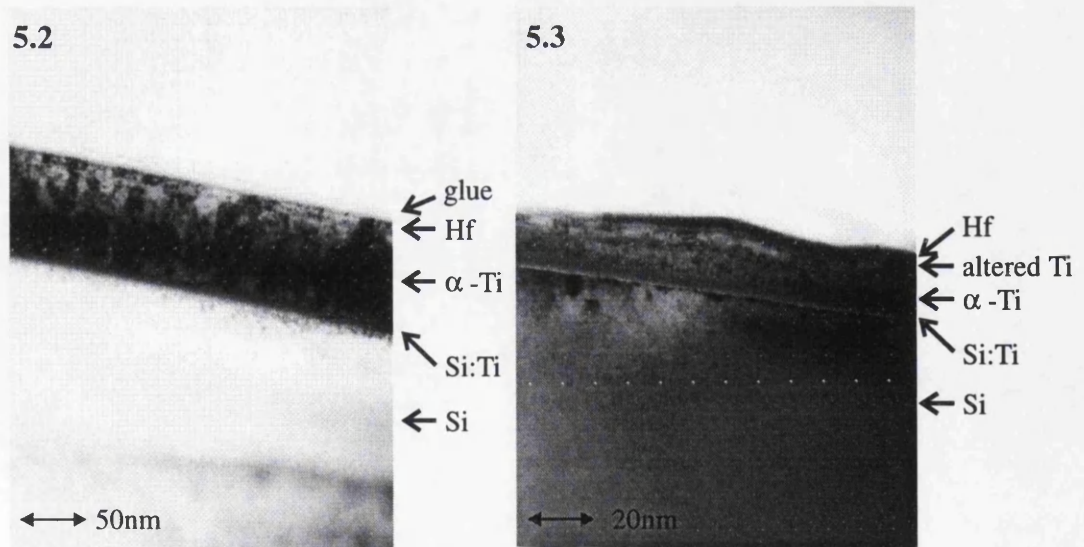

Figure 5.2 *Bright field image of Ti layer deposited on Si wafer and capped with Hf.*

Figure 5.3 *As in figure 5.2 but Cr sputter cleaned prior to capping with Hf.*

Pieces of the wafer were then used as substrates for further sputter cleaning and deposition in two separate sets. The first set were held stationary in the chamber with their surfaces at 0°, 45° and 90° to the cathode surface using the copper block described in section 2.2. They were sputter cleaned with Ti for 33 Amp hours and then coated with TiN for 2 Amp hours. The second set of three were sputter cleaned with Ti for 35 Amp hours and coated with TiN for 6 Amp hours. The copper block was rotating around its own axis and the axis of the chamber for the preparation of the second set of samples.

The pieces of wafer used as substrates were quite small, being 15mm square and therefore, the specimens were prepared from the middle of the samples. This was to minimise any effects resulting from shielding of the sample surface by the clamping rings holding them in place on the copper block.

Cross-sectional specimens were prepared from the above samples to study the interface region and allow the thickness of the various layers to be measured. However, because of the problem with the specimen preparation it proved possible to make successful cross-sections for only 2 out of the 3 of the TiN substrates recoated in rotation despite a number of attempts. It is not clear why these proved so difficult, since the overall coatings were actually thinner than the stationary ones which were relatively successful. Perhaps there was higher stress due to higher instantaneous deposition rates. The problem in preparing specimens was caused by preferential thinning of the Si in the ion milling stage causing the Si to thin away while the coating remained electron opaque. As thinning continued the coating fell out because of lack of mechanical support. This problem was overcome to a certain extent by reducing the thinning angle during ion milling as much as possible. The thinning time required per sample was thus considerably increased but some successful specimens were produced.

5.3 Cr sputter cleaning of Ti

This experiment was designed to model the sputter cleaning of Ti(6%Al,4%V) substrates with Cr ions.

In practice, interpretation of the results was not as simple as anticipated because the layer of Ti deposited was non-uniform. Nevertheless, some conclusions can be drawn by comparing the thickness of the layers along the cross-section in both specimens.

Figure 5.2 is a bright field image of the Ti layer capped with Hf. There are three layers on top of the Si substrate. The first is a Si:Ti amorphous layer about 10nm thick followed by the α-Ti layer. The third layer is the Hf cap. In this image, the sum thickness of the Si:Ti, Ti and Hf layers is 82±1nm. The Ti layer is 66±1nm thick and appears to be of more or less uniform thickness. Although it was locally uniform, the thickness of this layer varied from region to region of the specimen. Values of 108±2, 115±2, 120±2, 130±2, 160±2 and 180±2nm were measured for the sum thickness of the Si:Ti, Ti and Hf layers at various positions on this sample.

The bright field image shown in figure 5.3 is from the sample which was Cr sputter cleaned. Four different layers can be seen on top of the Si wafer. The first is the amorphous Si:Ti layer which is followed by the unaltered α-Ti layer. The third layer is the region of the Ti which has been affected by the sputter cleaning. The final layer is the Hf cap. It can be seen that the thickness of the Ti layer is locally non-uniform on this sample. The unaltered Ti layer thickness ranges from 6±2nm to 11±2nm. The altered Ti region is 4±2nm thick. There are lateral variations in the surface of the sample over about 30nm with depth variations of about 5nm. This image is typical of the sample although the actual layer widths varied from region to region.

The above values for the thickness measurements suggest that the Cr sputter cleaning removed a substantial amount of the Ti layer with an average erosion rate of about 6nm per Amp hour. EDX and EELS confirmed that there was also deposition of material during the sputter cleaning process. Cr was detected over about 15nm in an EELS line profile although the spectra were too noisy to quantify.

Four EDX maps from the sputtered specimen are shown in figure 5.4. The energy windows with which the maps were collected are given in table 5.2. From the table it can be seen that the energy window used to collect the characteristic X-rays from the Si K peak will also collect X-rays from the Hf M peaks. This manifests itself in the apparent presence of Si on both sides of the Ti layer in figure 5.4. The maps clearly show a non-planar layer of about 20nm which contains Cr as well as a region of Ti which contains no Cr.

Table 5.2 *Energy windows used to collect the X-ray maps in figure 5.4.*

element	peak type	peak energy (keV)	energy window (keV)
Si	Kα	1.7	0.34
Ti	Kα	4.5	0.5
Cr	Kα	5.4	0.42
Hf	Lα, Lβ	7.9, 9.2	1.96
Hf	Mα, Mβ	1.6, 1.7	-

Figure 5.5 is an EDX line profile taken on a sputtered sample. This graph shows the number of counts in the windows listed in table 5.2 for the Cr Kα, Ti Kα and the Hf L peaks. The profile shows incorporation of Cr into the Ti layer over about 30nm.

In summary, although the layer of Ti deposited was non-uniform the Ti:Cr layer was always found to be considerably narrower. The surface of the Ti:Cr

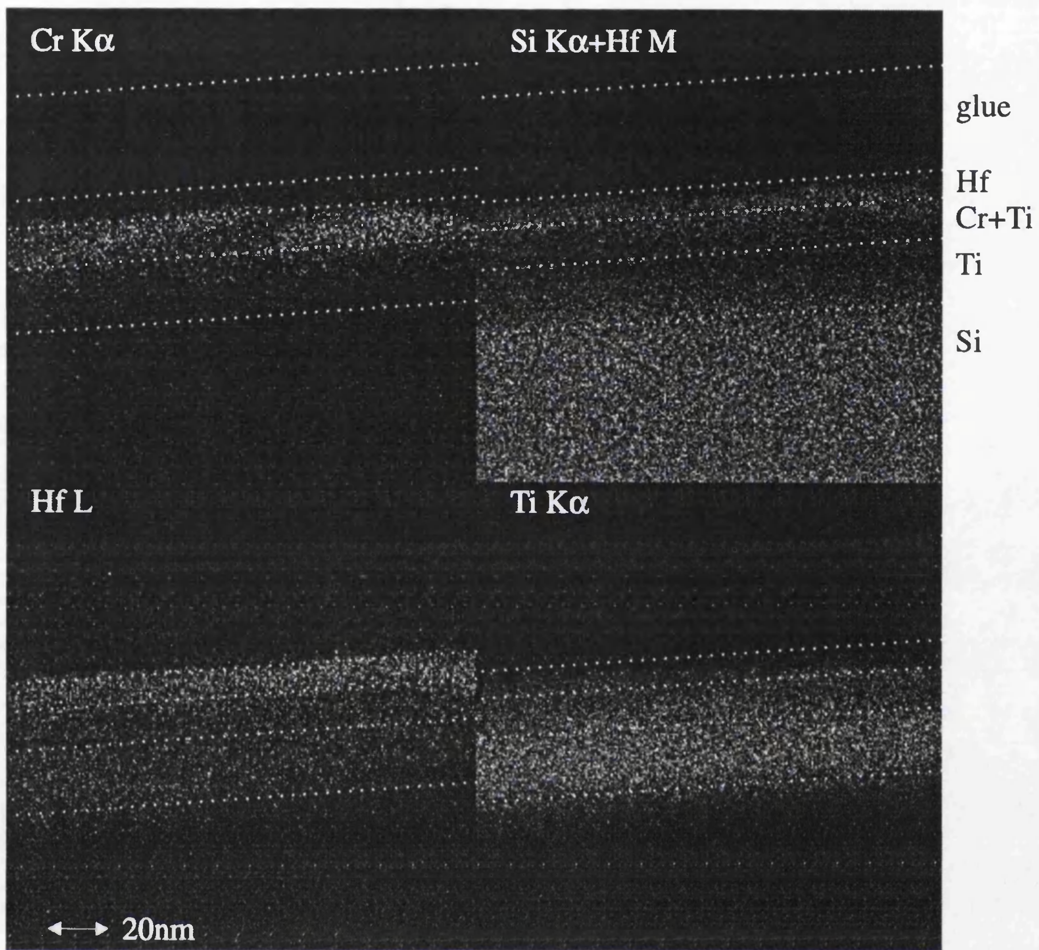

Figure 5.4 *X-ray maps of Cr sputter cleaned sample*

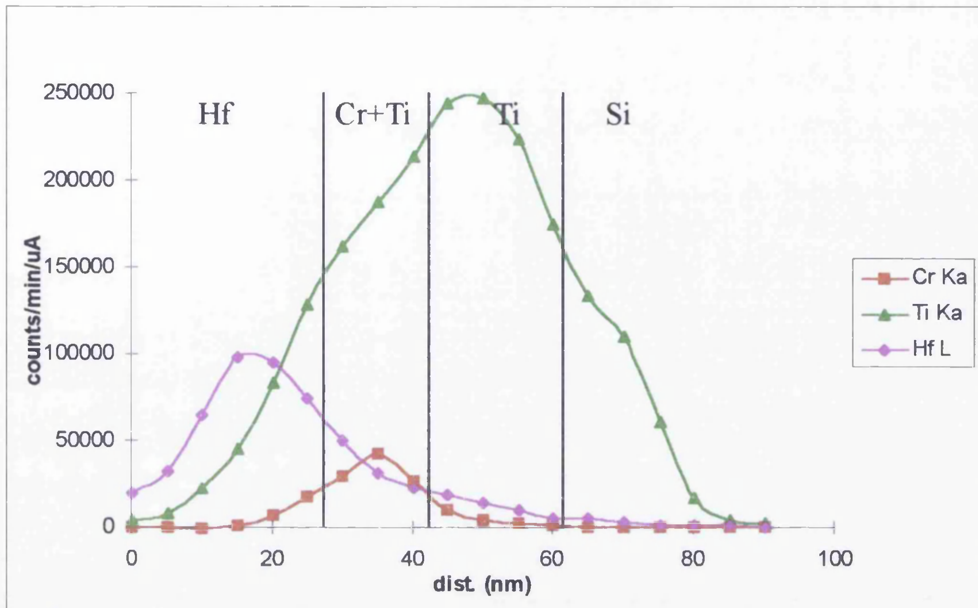

Figure 5.5 *EDX line profile of Cr sputtered sample of Ti.*

layer is locally more non-uniform than that of the Ti layer. Therefore, the net material transfer appears to be removal of Ti by the sputter cleaning process although there is also penetration of Cr into the Ti for a distance of the order of 5-30nm. The next section investigates the material transfer during the Ti sputter cleaning of TiN and subsequent recoating.

5.4 Ti sputter cleaning of TiN and subsequent redeposition of TiN

This section investigates the Ti sputter cleaning of TiN and the subsequent redeposition of TiN. This study is of relevance to the recoating of tools with TiN, an important aspect of the coating business. The thickness and composition of the layers observed in the samples for different substrate orientations and movements within the chamber are addressed first. EELS was used to identify the elements in the different layers observed.

Figure 5.6 shows a bright field CTEM image of a cross-section through the TiN sample where the substrate surface was parallel to the cathode surface (0°). The substrate with the marker layers can be clearly seen. The boxed region corresponds to the image in figure 5.1. A comparison of the layer widths in the substrate shows that the sputter cleaning process did not remove a significant amount of the 84nm TiN layer. Two layers were deposited on top of the substrate, the first of which was identified by EELS to be a layer of Ti deposited during the sputter cleaning. The width of this layer ranged from 550nm to 600nm. The error on these measurements was ±15nm. The notation (550-600)±15nm will be used throughout this chapter with the same meaning. The second layer was (74-89)±9nm of TiN deposited during the coating cycle.

The stationary 45° sample is shown in figure 5.7. It is necessary to compare images from adjacent or nearby regions of the specimen in order to identify the

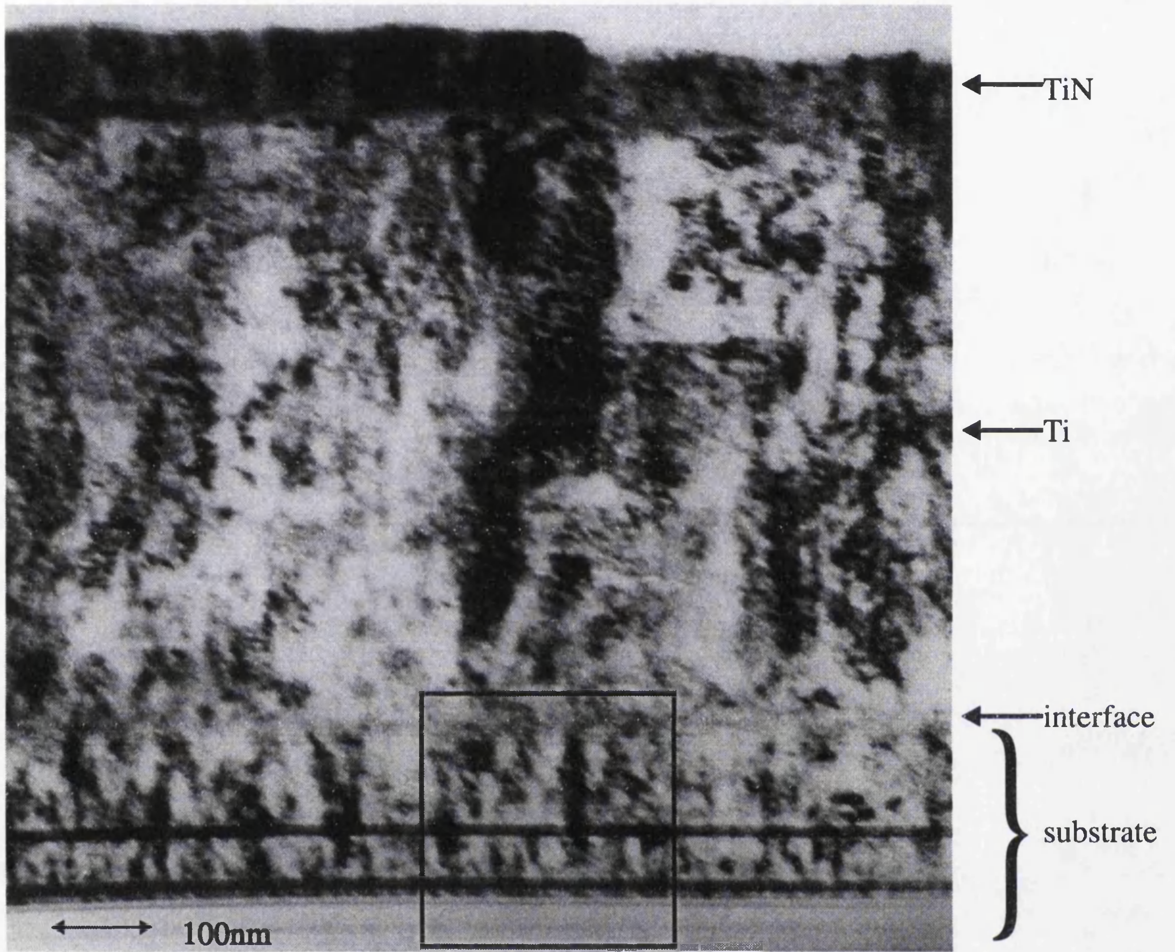

Figure 5.6 *CTEM image of 0° sample.*
The boxed region corresponds to figure 5.1.

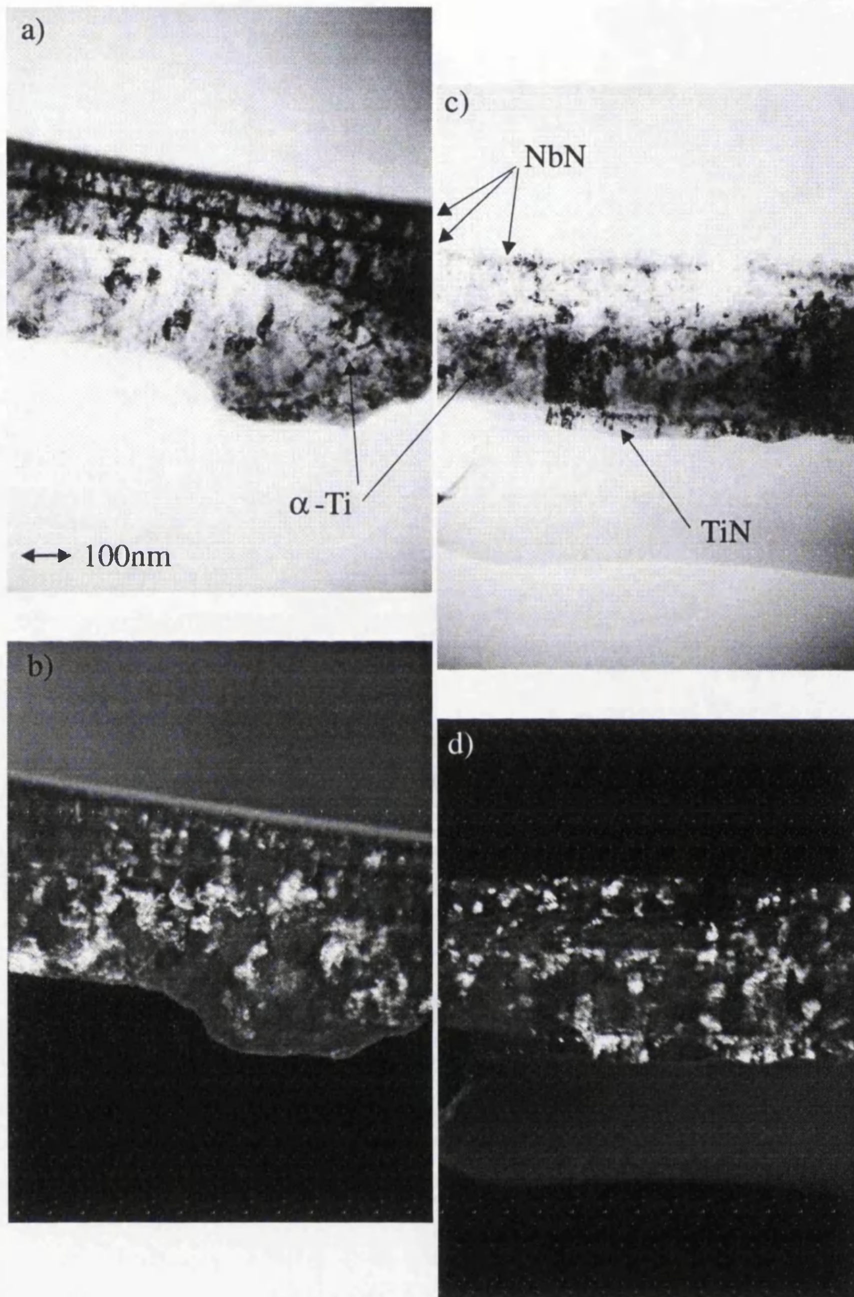

Figure 5.7 *Stationary 45° sample of TiN.*

position of the original substrate surface. This is because of the way the specimen thinned in the ion mill. Figures 5.7a-b are a bright and dark field pair showing the substrate with the marker layers and part of another layer deposited on top. This layer was identified to be Ti by EELS. The sputter cleaning process did not remove a measurable amount of TiN. Figures 5.7c-d are a bright and dark field pair showing part of the substrate with one marker layer just visible, the Ti layer and another layer which was identified as TiN. The two sets of images have been aligned using the second NbN marker layer. The thickness of the Ti and TiN recoat layers were measured to be (180-209)±15nm and (30-45)±4nm, respectively.

Figure 5.8 shows a bright and dark field pair of the stationary perpendicular sample. Again the sputter cleaning process did not appear to remove a significant quantity of TiN from the substrate. There is only one layer on top of the substrate in this sample. This was identified by EELS to be a layer of TiN of (30-36)±4nm thickness. However, a region of approximately 5±2nm was found in the EELS line profile across the TiN substrate/TiN recoat interface in which the N content dropped although it did not reach zero. This chemical profile is shown in figure 5.9.

Figures 5.10a-b show the substrate and part of a layer of Ti on the parallel rotating sample. Again, because of way the specimen thinned, it is necessary to compare nearby parts of the cross-section to get the full picture. Figures 5.10c-d are a bright and dark field pair showing the TiN recoat layer. The layer thicknesses were measured to be (158-177)±5nm and (47-61)±5nm for the Ti and TiN layers, respectively.

Figures 5.11a-b show the perpendicular rotating sample. Part of the TiN recoat layer can be seen in figure 5.11a. This layer was measured from figure 5.11b to be 139±10nm thick by subtracting the substrate thickness from the sum thickness. As with the perpendicular stationary sample, a region of about 10±4nm was observed in the EELS line profile in which the N content dropped

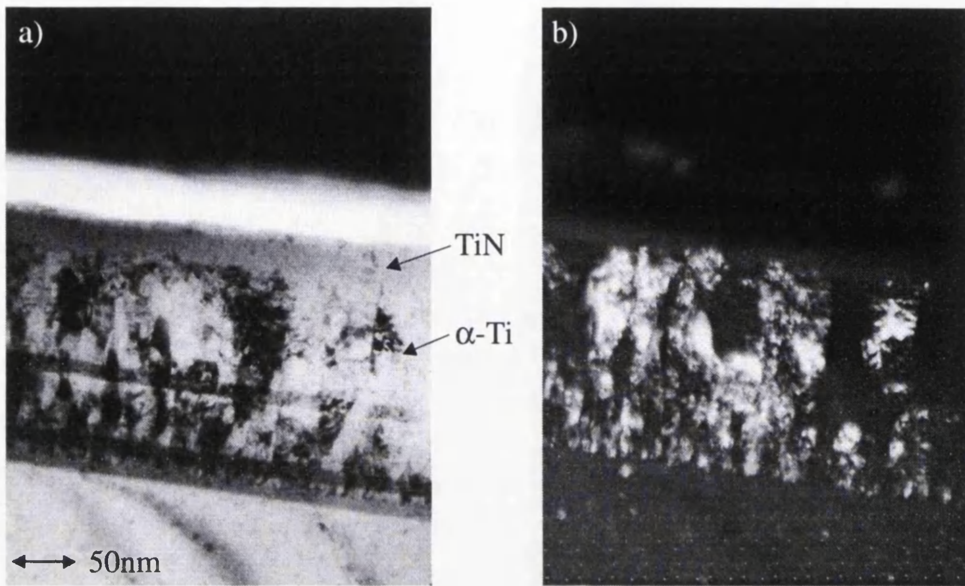

Figure 5.8 *Stationary perpendicular sample of TiN.*

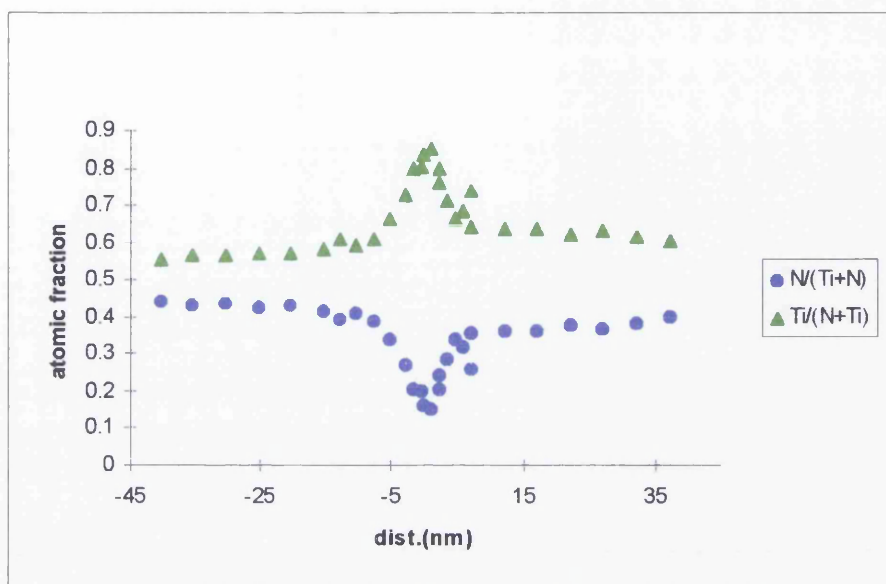

Figure 5.9 *EELS profile for stationary perpendicular sample of TiN.*

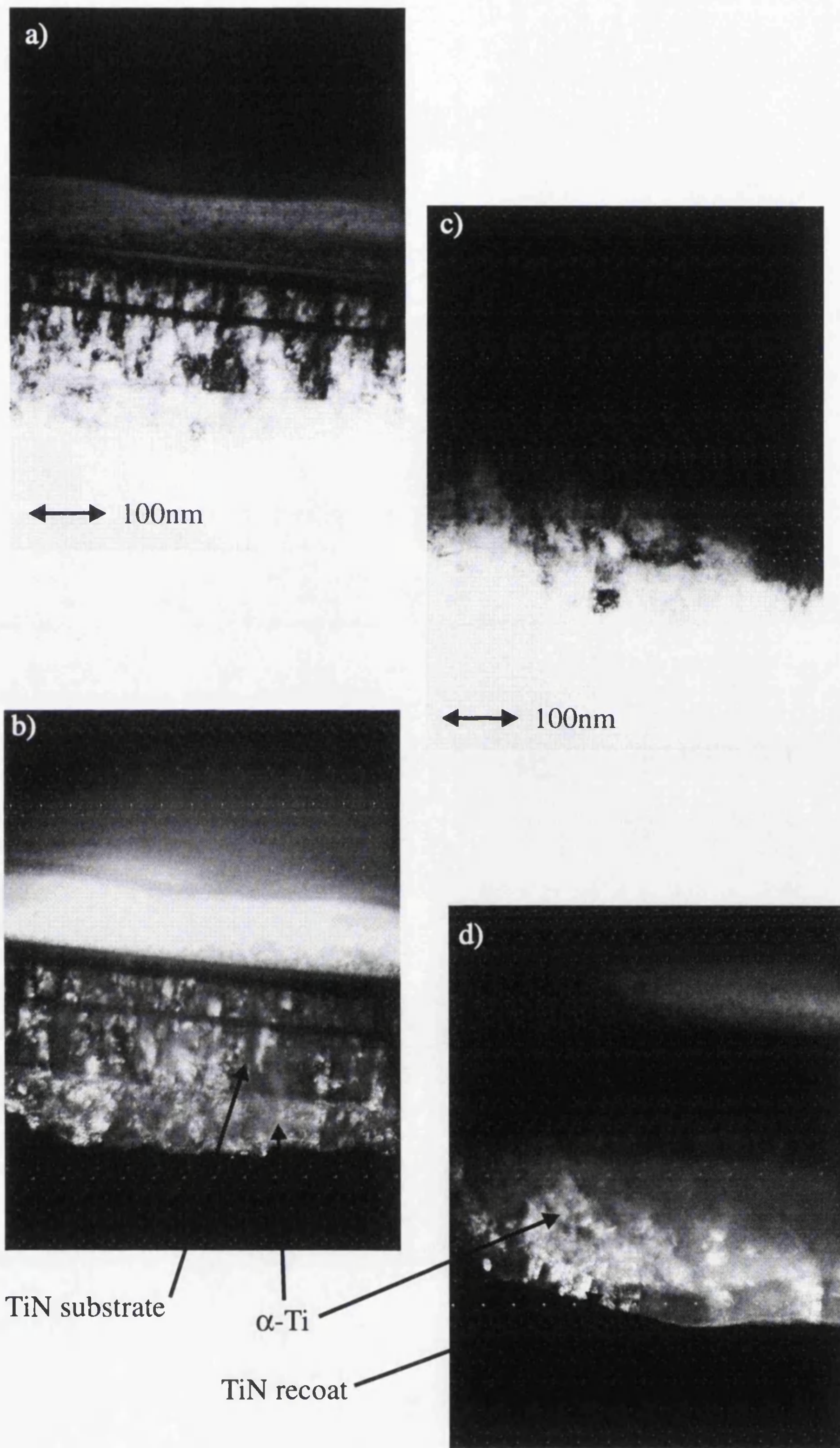

Figure 5.10 *Rotating parallel sample of TiN.*

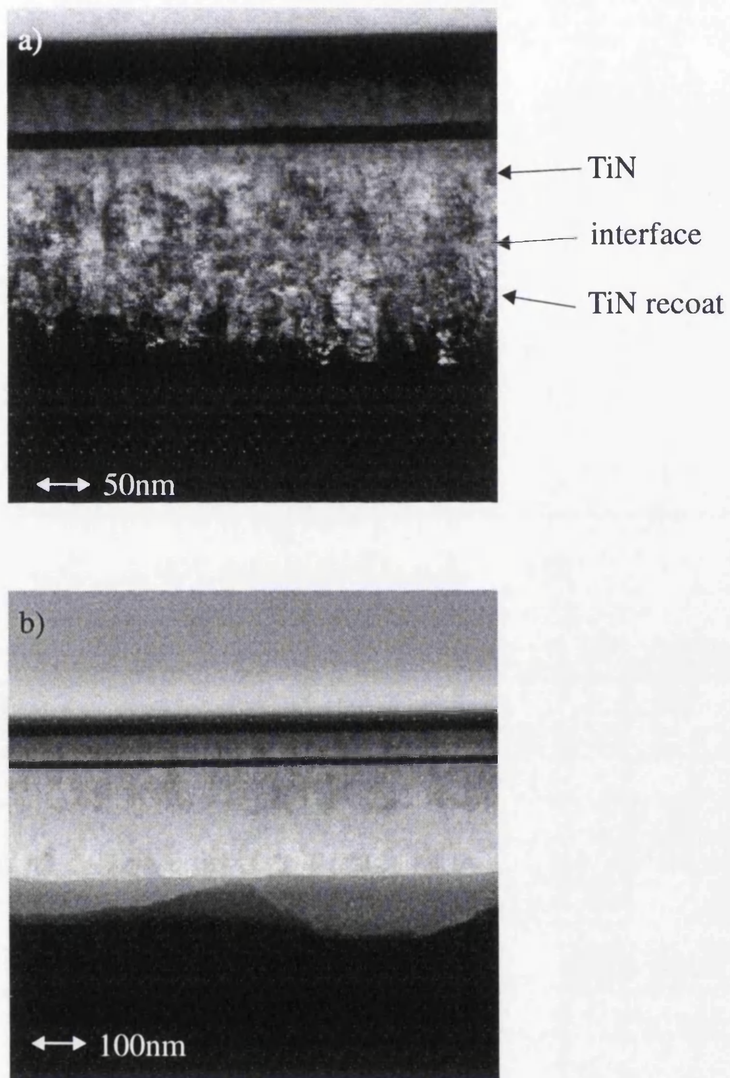

Figure 5.11 *STEM images of 90° rotating sample of TiN.*

although again it did not quite reach zero. Figures 5.12 is an EELS line profile on this sample across the TiN/TiN recoat interface.

A summary of the layer thicknesses for the different samples is presented in table 5.3. The trends in thickness as a function of orientation for the stationary and rotating samples are discussed below.

Table 5.3 *Layer thicknesses after Ti sputter clean and TiN recoat.*

substrate motion	substrate orientation relative to cathode surface	TiN removed (nm)	Ti deposited (nm)	TiN deposited (nm)
stationary	0°	0±5	(550-600)±15	(74-89)±9
stationary	45°	0±5	(180-209)±15	(30-45)±4
stationary	90°	0±5	5±2	(30-36)±4
rotating	0°	0±5	(158-177)±5	(47-61)±5
rotating	45°	-	-	-
rotating	90°	0±5	10±4	139±10

It is clear that the effects of the sputter cleaning and subsequent recoating are not independent of the angle of orientation of the substrate to the cathode. The effect of the orientation is similar to that observed in sections 4.4 and 4.5 for CrN coatings on Ti(6%Al, 4%V). In the case of the 0° and 45° stationary samples, significant amounts of Ti have been deposited. The 90° sample showed very little Ti deposition, as one would expect from the ion trajectories in the chamber. The shape of the EELS line profile for this sample exhibits a diffusion like distribution of Ti in the TiN at the surface showing that there was deposition of a small amount of Ti. Either Ti was implanted in the substrate

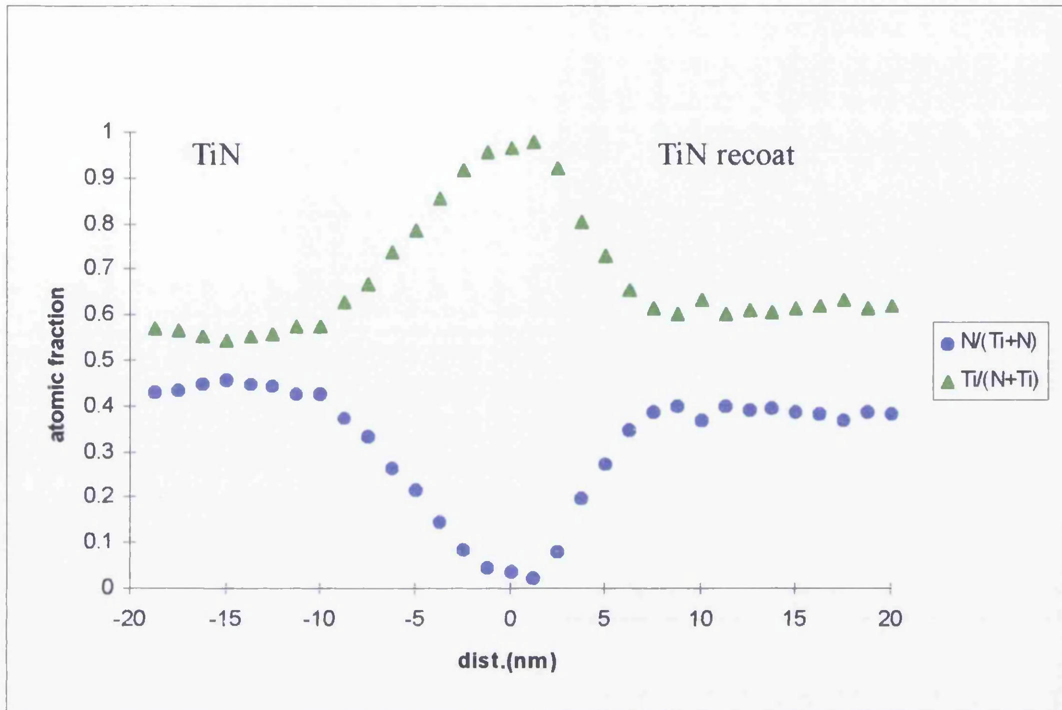

Figure 5.12 *EELS line profiles for rotating perpendicular sample of TiN.*

surface and subsequently diffused further into the substrate or a thin layer of Ti was deposited into which N diffused.

All three stationary samples received an appreciable coating of TiN. The reason for this is scattering by the N_2 gas in the deposition cycle leads to a more even distribution of coating. The stationary 0° sample received a factor of about 7 times more Ti than TiN. The main reason for this was that the sputter cleaning cycle was continued for 33 Amp hours whereas the coating cycle only lasted 2 Amp hours. This means that the effective deposition rate is higher during the TiN deposition than during the Ti sputter cleaning. A similar ratio of about 7 is obtained for the 45° sample. The situation is different for the 90° sample where there was very little Ti deposited.

The rotating samples follow a similar trend. There are significant differences in the amount of Ti deposited during the sputter cleaning process. The 90° sample received very little Ti whereas the 0° sample received a significant amount. Again the differences in the quantities of TiN deposited are much less than of Ti. However, in this case the 90° sample received more TiN than the 0° sample. This is because, due to the rotation, the 0° sample was out of the line of sight of the cathode for part of the process while the 90° sample was always in line of sight of the cathode. The coating cycle continued for 6 Amp hours to compensate for the rotation of the substrates. Comparing the thicknesses of the TiN layers for the stationary and rotating samples it can be seen that in the case of the 90° sample there was overcompensation and the TiN layer was thicker than on the stationary 90° sample. However, the 0° rotating sample received less coating than the 0° stationary sample because it was out of line of sight of the cathode and even with gas scattering did not receive so much TiN. This shows that the fact that the sample is going out of line of sight of the cathode has the greater effect.

The explanation for the difference in deposition rates for the Ti sputter cleaning cycle and the TiN coating cycle is as follows. At the higher bias voltage used for sputter cleaning, it is likely that some of the Ti deposited is re-sputtered, so

that the effective deposition rate is lowered. During TiN deposition, the combination of the lower bias voltage and the increased binding energies of the surface atoms should considerably reduce this re-sputtering increasing the effective deposition rate. However, the N_2 gas poisons the cathode reducing the Ti flux and hence lowering the effective deposition rate. Gas scattering in the chamber during the coating cycle further reduces the effective deposition rate for parallel samples by more evenly distributing the coating. Overall the decrease in the re-sputtering seems to be the biggest effect leading to a higher deposition rate for TiN deposition.

Removal of any significant amount of the original TiN coating by the sputter cleaning process was not observed in any of the samples studied. This is because the nitrided surface has good stability. This is evidenced by the poisoning of the cathode which occurs subsequent to the introduction of N_2 gas into the chamber.

5.5 Conclusions

The Cr sputter cleaning of Ti results in a net removal of material although there is also deposition of Cr. The Cr is incorporated into the Ti over a distance of about 15-30nm. The system studied is only a model of the Cr sputtering of Ti(6%Al, 4%V) and there may be differences between the properties of this Ti layer, which is columnar with significant internal stress and the Ti(6%Al, 4%V), which is a complex two phase material. The grain size in the Ti(6%Al, 4%V) is much larger than in the Ti layer and also there is the presence of the β-phase which has a different structure. This could result in the Cr sputter cleaning having different effects on the two materials. However, given the nature of the process and the similarity in crystallographic structures, such differences are not expected to be substantial.

Ti sputter cleaning of TiN did not appear to remove a measurable amount of material from the substrate because of the stability of the TiN surface. There was a net deposition of Ti, the quantity of which was strongly dependent upon the orientation of the substrate surface to the cathode ranging from 5±2nm to (550-600)±15nm for perpendicular and parallel substrates. The quantity of TiN deposited in the subsequent coating cycle was also dependent upon the orientation of the substrate in the chamber varying from (30-36)±4nm to (74-89)±9nm. The rotation of the samples during the cycles influenced the relative thicknesses of the Ti and TiN layers deposited at different orientations.

It is clear that the thicknesses of the layers deposited during the sputter cleaning and subsequent recoating cycles are a result of the combined effect of the orientation and the rotation of the substrate in the chamber. Under normal commercial deposition conditions, these effects will be minimised for two reasons. Firstly, several cathodes situated at different positions in the coating chamber are used so that the flux distribution is much more uniform within the chamber. Secondly, the tools rotate around both their own axis and the axis of the chamber thus reducing the effect of orientation. However, the tools being coated often have complex shapes and so it is inevitable that some parts will be in line of sight of the cathodes for longer than others resulting in an uneven distribution of coating. This uneven distribution of coatings on non-planar substrate surfaces is a limitation of the coating technique (Rother, 1988). It is also possible to increase the uniformity of the coating by increasing the gas pressure in the chamber (Matthews 1985) but the reduced evaporation rate from the cathode makes it more desirable to use multiple cathode sources and rotation of the substrate.

The inability of the Ti sputter cleaning to remove TiN from the substrate means that some other way must be found to remove the old coating in order to prevent the coatings from building up and affecting the tolerance in the dimensions. In practice, the TiN is either removed by stripping it off and the tool treated as an original coating problem or the surface is cleaned by radiant heating rather than sputter cleaning.

This chapter has examined the nature and net direction of material transfer at the substrate during the sputter cleaning process. Different net directions of material transfer were observed for different systems. However, only the coatings themselves were considered. The sputter cleaning process also results in metal droplets being incorporated into the coating. These droplets constitute a significant fraction of the mass loss from the cathode. The exact percentage which is lost as droplets depends upon the cathode material among other things (Daalder, 1976). The nature of these droplets are the subject of the next chapter although the quantity of deposited material that they constitute is not determined.

CHAPTER 6

Deposition of droplets

6.1 Introduction

Droplets form a non-negligible percentage of the mass emitted from the cathode and are one of the features of coatings deposited by cathodic arc evaporation. Much research has gone into the suppression/control of droplet emission. The emission rate of droplets from the cathode depends upon several parameters such as: the arc current (Daalder, 1976), the melting point of the cathode (Daalder, 1976) and the partial pressure of the reactive gas (Bergman, 1988). The reactive gas poisons the cathode by nitriding the cathode surface, and thus reducing the effective evaporation rate of Ti and suppressing the formation of droplets. Therefore, the highest emission rate of droplets will occur before poisoning of the cathode takes place i.e., during the sputter cleaning process and the initial part of the coating process.

Droplets vary in size being up to about 50μm in diameter (Daalder, 1976). Their presence is detrimental to the quality of the coating and is a serious problem in some applications. They also spoil the aesthetic appearance of the coating.

Although a lot of research has been done on the mechanism and control of droplet formation at the cathode, there has been very little microanalysis performed on droplets. Some research was done on Ti droplets in TiN films by Ljungcrantz et al (1994) at Linköping. All of the droplets studied by Ljungcrantz et al were totally surrounded by coating and therefore, must have been deposited during the coating process.

This chapter presents results from Ti and Cr droplets. Section 6.2 describes the samples studied. The distribution and shape of Ti droplets on a TiN coating are studied for different orientations and rotations in section 6.3. Section 6.4 looks at the growth of the CrN coating around Cr droplets. Microanalytical results are presented in section 6.5, where EELS and EDX were used to analyse the Cr droplets and the surrounding material. The conclusions which can be drawn from these investigations are given in section 6.6.

6.2 Description of samples

All of the samples studied in this chapter were examined previously in chapters 4 or 5. The sputter cleaning and coating parameters which are of relevance to this chapter are listed in table 6.1.

Table 6.1 *Summary of samples studied in this chapter.*

substrate	sputter cleaning ion	orientation	motion	substrate bias (V)	coating
TiN	Ti	0°, 45°, 90°	stationary	-150	TiN
TiN	Ti	0°, 45°, 90°	rotating	-150	TiN
Ti(6%Al, 4%V)	Cr	10°	rotating	-200	CrN
Ti(6%Al, 4%V)	Cr	45°	rotating	-200	CrN

SEM specimens from the TiN re-coated samples studied in chapter 5 were used to investigate the effect of orientation and rotation on the distribution and shape of the droplets.

Microanalysis was performed on droplets from two samples of CrN on Ti(6%Al, 4%V) discussed in chapter 4. The Ti(6%Al, 4%V) substrate was sputter cleaned with Cr prior to being coated with CrN. Droplets were studied in a planar specimen of CrN deposited at -150V substrate bias and at 10° to the cathode i.e., effectively parallel. The second specimen was a cross-section from CrN deposited at -200V and 45°. Selected area diffraction performed on some of these droplets resulted in single crystal diffraction patterns which indexed as bcc Cr.

6.3 Distribution and shape of droplets

This study of Ti droplets on TiN coatings should determine the effect of the orientation and rotation of the substrate on the distribution and shape of the droplets. Daalder (1976) made similar studies using highly polished stainless steel substrates but pointed out that different substrates could affect the shape of the droplets.

Figures 6.1 and 6.2 are SEM images of the surfaces of the TiN re-coated samples. It should be noted that there is no correlation between the way the samples were mounted in the chamber and the way in which they are shown in figures 6.1 and 6.2. The samples in figure 6.1 were flat in the electron beam whereas those in figure 6.2 were tilted 30°. Figure 6.1a shows the droplet distribution on the surface of the stationary parallel coating. There is a wide distribution of droplet sizes with the largest droplets being about 15μm in diameter. The smallest droplets which can be resolved from the image are

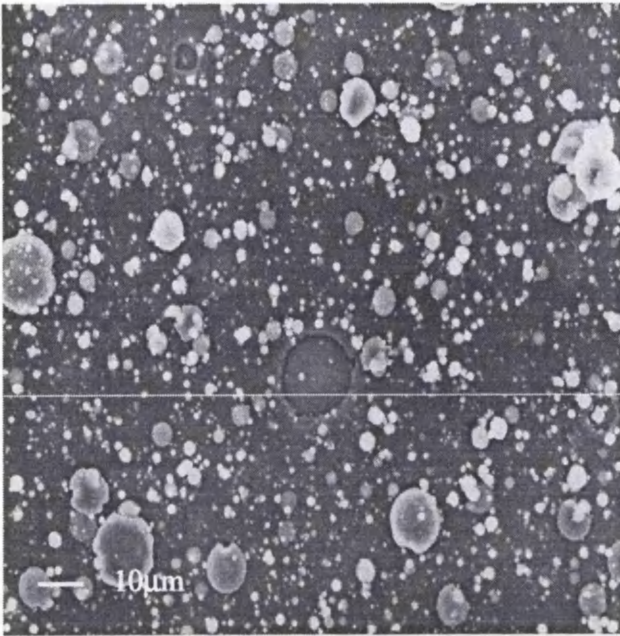

Figure 6.1a *Stationary parallel TiN coating.*

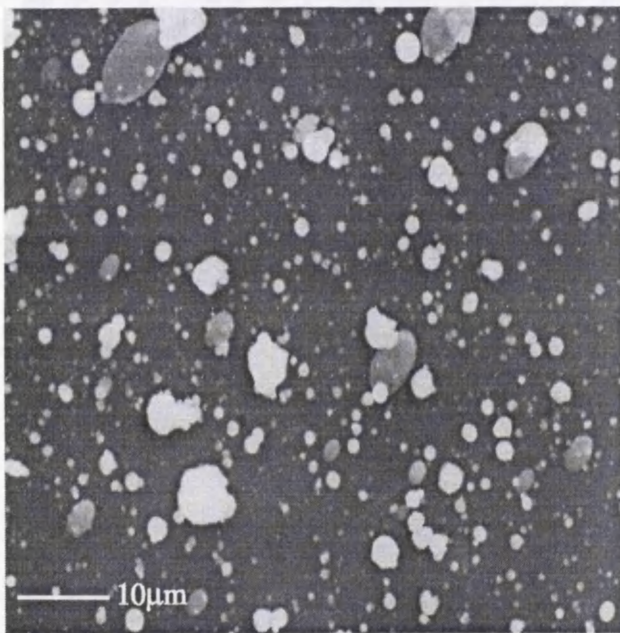

Figure 6.1b *Stationary 45° TiN coating.*

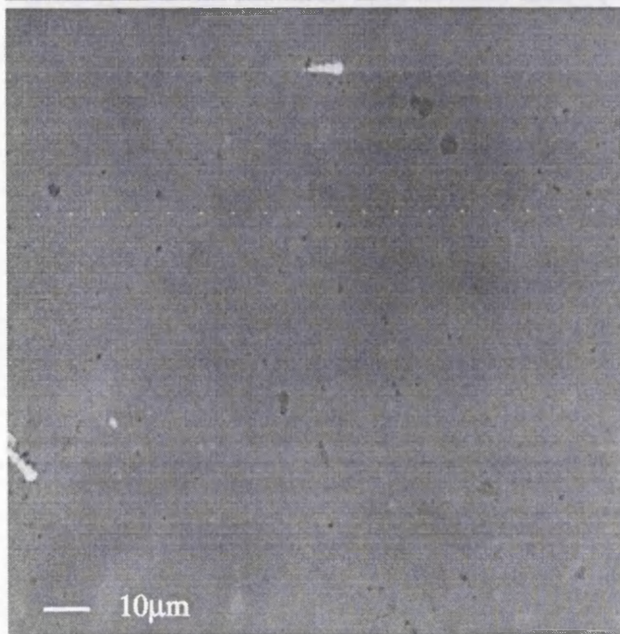

Figure 6.1c *Stationary perpendicular TiN coating.*

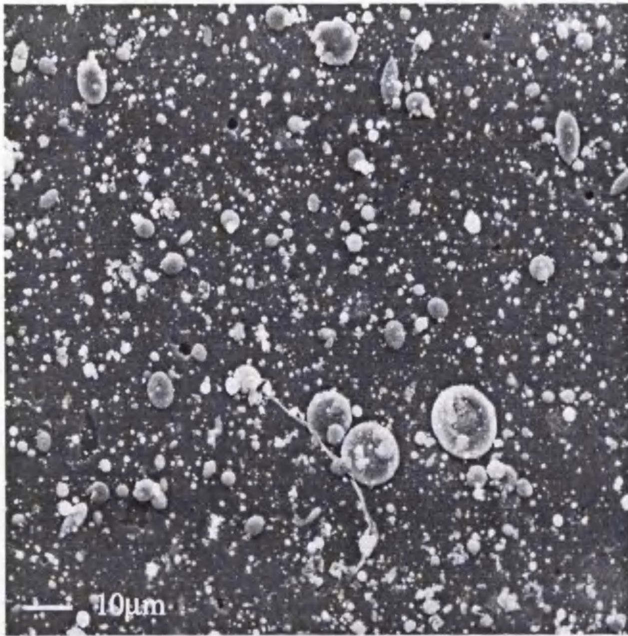

Figure 6.2a *Rotating parallel TiN coating. Sample tilted 30° in beam.*

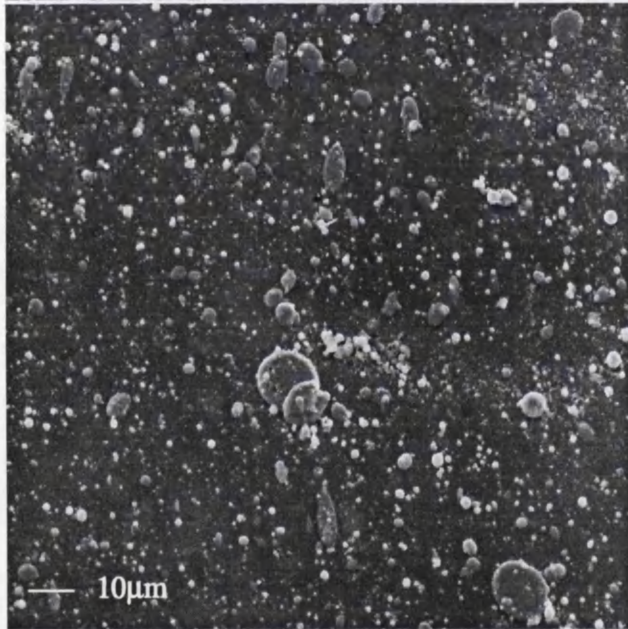

Figure 6.2b *Rotating 45° TiN coating. Sample tilted 30° in beam.*

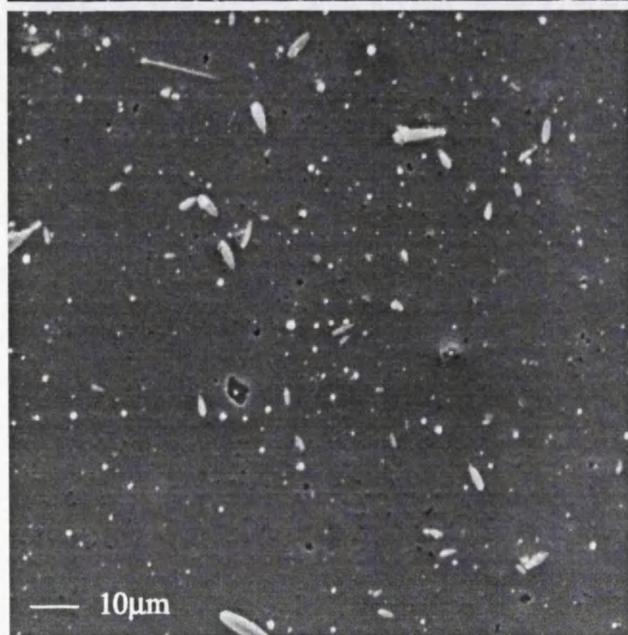

Figure 6.2c *Rotating perpendicular TiN coating. Sample tilted 30° in beam.*

250nm in diameter. Studies at higher magnifications are required to determine the smallest droplet size. Most of the droplets are spherical in shape indicating that they probably arrived at the surface in the solid state. However, the larger droplets are less regular and look as if they were still molten when they hit the surface. Some craters where droplets have not adhered to the surface show up as round dark areas.

The 45° stationary sample which is shown in figure 6.1b has fewer droplets on its surface. The larger droplets on this sample are ellipsoidal with their major axes aligned along the same direction. These droplets arrived at the substrate in a molten state and streaked out along their direction of motion.

The perpendicular stationary sample is shown in figure 6.1c. There are very few droplets on this surface. The largest of these are only about 4μm in diameter. The contrast apparent in the image is probably from drying marks on the substrate surface from the cleaning agent which was applied to the sample before examining it in the SEM.

The coating surface shown in figure 6.2a is for the rotating parallel sample. The surface is generously covered with droplets to the extent that droplets have landed on top of other droplets. The largest droplets are about 15μm in diameter. Most of the droplets are spherical although there are a few ellipsoidal droplets present. Some of the largest droplets on the image appear to have toroidal regions at their rims where they are thicker. This suggests that they arrived at the surface while still molten and that their shape is a result of the impact.

Figure 6.2b shows the coating on the rotating 45° sample. The number of droplets per unit area on this coating is similar to that of the rotating parallel sample. The ellipsoidal droplets on this sample and that of the rotating parallel sample are generally aligned along one direction.

Figure 6.2c shows the surface of the coating on the sample which was rotating perpendicular to the cathode surface. The number of droplets per unit area is substantially fewer. There is a fine scattering of small spherical droplets. The larger droplets are all ellipsoidal but their aspect ratio is different from the ellipsoidal droplets in figures 6.2a and 6.2b. They are much more elongated and are not aligned in any particular direction.

Several conclusions can be drawn from the above observations. The number of droplets deposited on the stationary coatings decreased as the angle of orientation between the substrate surface and the cathode increased. There were very few droplets on the surface of the perpendicular sample. A similar trend in the distribution of droplets was observed with the rotating samples although the perpendicular sample received more droplets. The distribution of droplets with orientation and rotation are similar to the distributions of Ti and TiN observed in chapter 5.

A fairly wide distribution of droplet sizes was observed with droplets up to 15μm in diameter. The average size of the droplets on the rotating samples was smaller. This is probably a result of differences in the arc current at the cathode rather than a result of the rotation. The smallest droplets which could be resolved from the images in this chapter were about 250nm in diameter.

Most of the smaller droplets deposited were spherical. This suggests that they solidified before they reached the substrate. Some of the larger round droplets looked thicker at their rims while others were ellipsoidal. These made contact with the surface while they were still in a molten state and streaked out along their direction of travel. This explains why they were aligned on the stationary 45° sample but randomly arranged on the rotating perpendicular sample. Most of the ellipsoidal droplets on the rotating 0° and 45° samples were aligned indicating that most of the droplets are deposited when the substrate is in line of sight of the cathode. Similar variations in droplet shapes with different orientations of the substrate surface to the cathode surface were observed by Daalder (1976) for stainless steel substrates.

6.4 Growth of the coating around droplets

The growth of the CrN coating around the Cr droplets was studied by imaging droplets in a planar specimen and in a cross-sectional specimen.

Figure 6.3 shows pairs of bright and dark field images taken from the planar specimen at two different magnifications. The interface between the droplet and the coating is clearly delineated. Columnar growth of the coating around the droplet in a different direction from the bulk coating has occurred. This columnar growth of the coating radially out from the droplet surface was observed around several other droplets in this specimen.

Figures 6.4 & 6.5 show droplets in the cross-sectional specimen. There are voids under the droplets where the droplets prevented the substrate from receiving coating by shadowing it. These voids lead to poorer adhesion between the droplets and the coating. Ljungcrantz et al (1994) also observed voids under Ti droplets embedded in TiN coating. The droplets in figures 6.4 and 6.5 are not sitting on top of coating material and therefore must have been deposited either during the sputter cleaning process or early on in the coating cycle.

In summary, columnar growth of the coating around several droplets was observed with the coating growing radially out from the droplet surface. Some of the droplets observed showed no evidence of this columnar growth of CrN from their surfaces possibly because they were in poor contact with the substrate which resulted in them charging up as soon as ions arrived and hence subsequent ions arriving were repelled.

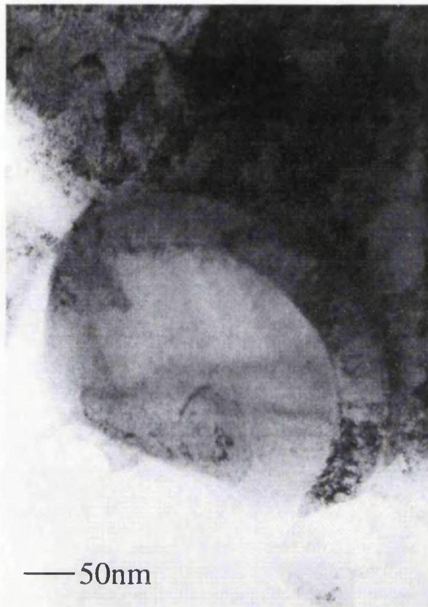

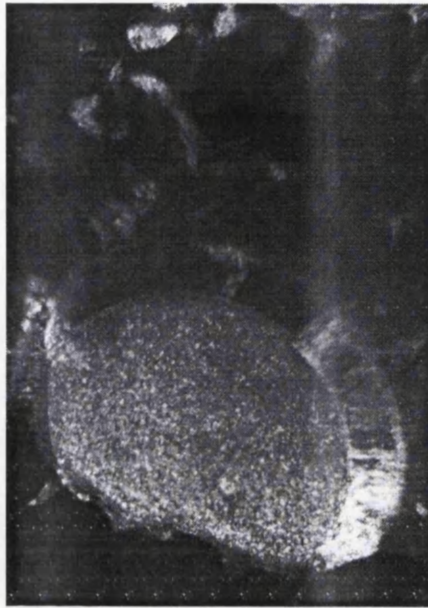
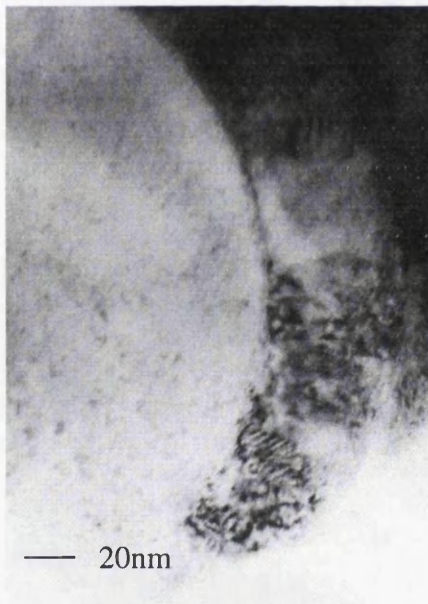

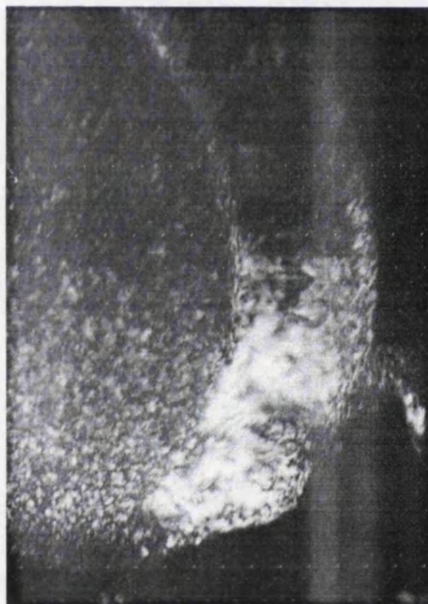

Figure 6.3 *Cr droplets in a planar specimen of CrN on Ti(6%Al, 4%V).*

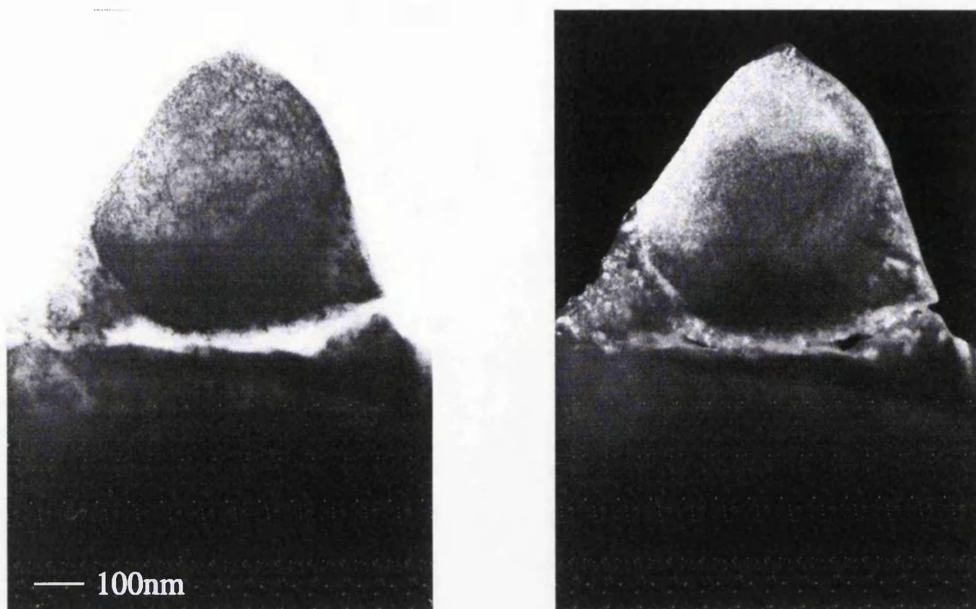

Figure 6.4 *Cr droplet in cross-sectional specimen of CrN on Ti(6%Al, 4%V).*

Figure 6.5 *Cr droplet in cross-sectional specimen of CrN on Ti(6%Al, 4%V).*

6.5 Composition of the droplets and surrounding material

Three droplets are discussed in this section, namely a coated planar droplet, an uncoated planar droplet and a coated droplet in cross-section. The planar droplets were from the CrN sample deposited at -200V and 10°. The cross-section was from the 45° -200V CrN sample. Microanalysis was performed on droplets and across droplet/coating interfaces to investigate the chemical composition of the droplets. X-ray mapping was used to give an overview of the chemical composition of the sample. The contrast for each X-ray map in this chapter has been adjusted individually to highlight the distribution of the element within the given map. This means that no conclusions can be drawn about the ratio of elements in the area mapped simply by comparing the intensity of the different elemental maps. The mapping technique was too time consuming to give adequate counts per pixel for the detection of small features or low elemental concentrations and therefore, EDX point analyses in the form of line profiles were also performed on the samples. The bremsstrahlung intensity in the EDX spectra was used as an indication of the mass-thickness of the specimen using an energy window in the 10-15keV range. EELS line profiles were also taken where the specimens were not too thick so that the presence of N could be detected.

Coated planar droplet

Figure 6.6a is an image of a droplet in a planar specimen. The coating around the droplet is columnar but growing radially out from the droplet. This radial growth continues for about 120±5nm. Figures 6.6b-c are corresponding Cr Kα and Ti Kα X-ray maps where the maps have been rotated and chopped in order to align them in the same direction as the electron image in figure 6.6a. The Cr

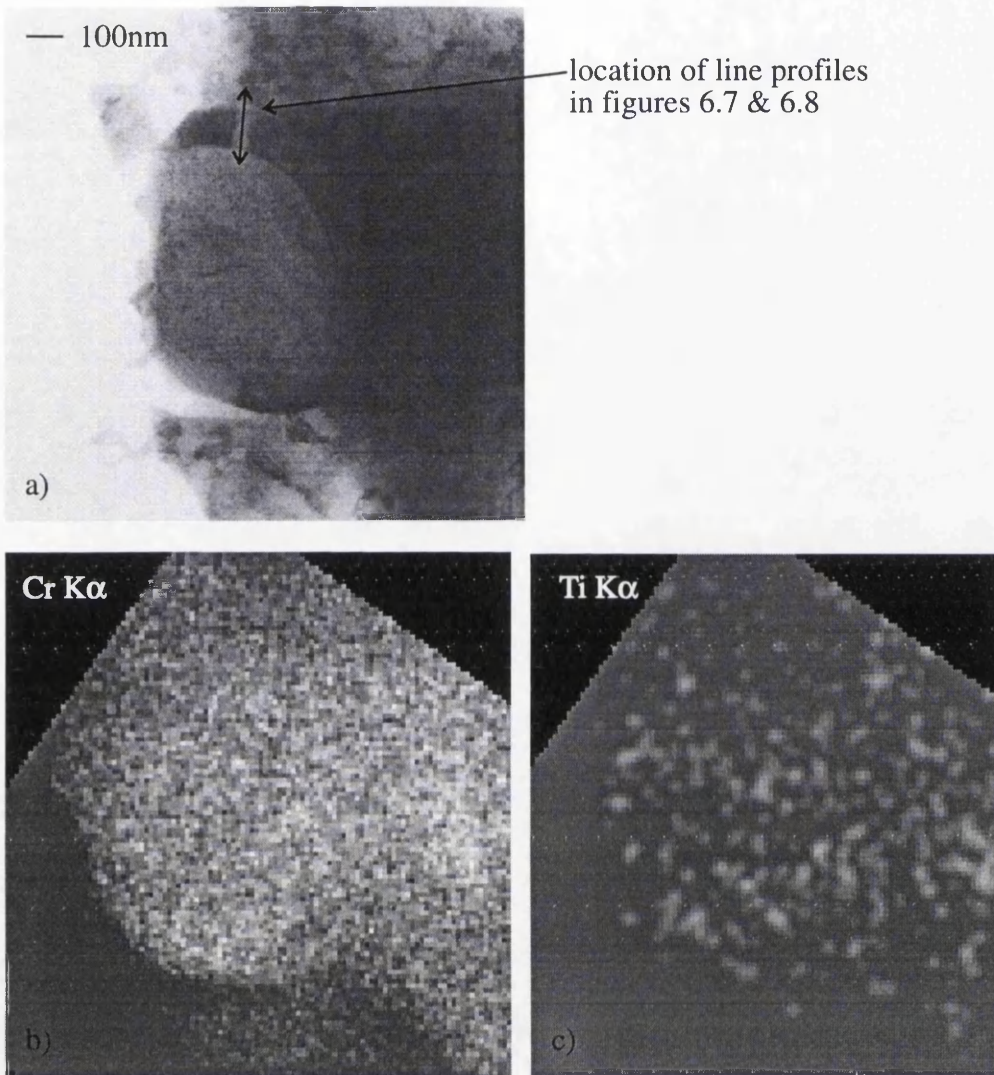

Figure 6.6 *Cr droplet in planar specimen of CrN on Ti(6%Al, 4%V).*

a) Bright field image

b) & c) Cr & Ti X-ray maps.

map shows that the droplet contains Cr. The intensity in the Ti map is a result of the background counts in the Ti window.

Figure 6.7 is an EDX line profile across the droplet/coating interface at the position marked on figure 6.6a. The EDX and the EELS line profile data on this droplet were both collected by scanning over a region about 15nm^2 because problems with contamination made it impossible to collect data from points. The number of counts per second per μA of incident beam current in the energy windows set on the spectra are plotted rather than the atomic fractions in this case. These numbers are related to the number of atoms of each species because the k_{ab} value for Cr and Ti is effectively unity. The bremsstrahlung trace follows the shape of the Cr trace showing that the changes in mass-thickness are a result of changes in the quantity of Cr present. A dip in the Cr counts and in the mass thickness at the droplet/coating interface is evidence for a void. X-rays emanating from the bulk substrate as a result of electron scattering causes a small Ti peak to appear in all of the X-ray spectra. However, a rise in the amount of Ti can be seen at the droplet/coating interface. This Ti feature was too small and/or the signal too weak to be resolved by the X-ray mapping.

Figure 6.8 shows the EELS line profile from the same position on the specimen. The absence of Ti in the droplet shows that the small amount of Ti observed with the EDX spectra and map was a result of scattering rather than the presence of some remaining substrate. There is a greater concentration of Ti at the droplet/coating interface examined in the profile than in the surrounding material.

EELS can also be used to give some information on the crystallographic structure of materials. The ELNES on the N K edges from the EELS spectra were compared with those of CrN and Cr_2N standard samples. These comparisons showed that the coating on the droplet initially grew as Cr_2N. The stoichiometry of the CrN in the radial coating appears to be different from that

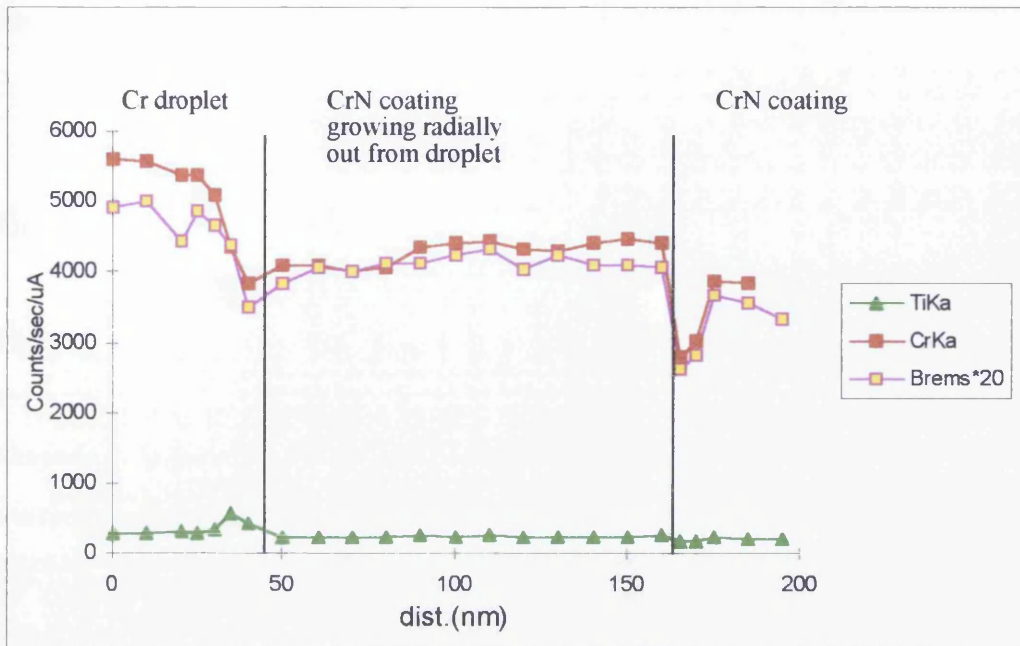

Figure 6.7 *EDX line profile across region in figure 6.6.*

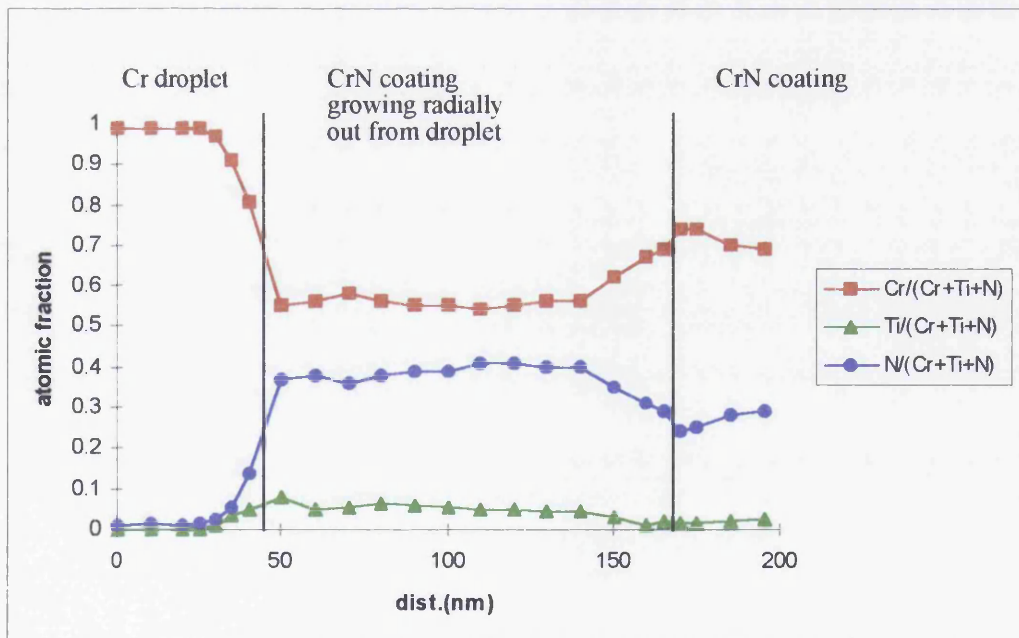

Figure 6.8 *EELS line profile across region in figure 6.6.*

of the surrounding coating. This is probably because there is an overlap of CrN and Cr_2N coating.

Uncoated planar droplet

Figure 6.9a is an electron image of another droplet in planar section. There is no columnar growth of coating out from the droplet in this image. A crescent shaped region of different contrast can be seen next to the droplet. The corresponding Cr Kα X-ray map in figures 6.9b shows that the droplet contains Cr. From the Ti Kα map it may be concluded that the Cr droplet apparent in the Cr Kα map is partly sitting on top of Ti rich region.

Figure 6.10 is the EDX line profile taken across the droplet/coating interface at the position marked on figure 6.9a. The bremsstrahlung trace follows the shape of the sum of the Cr and the Ti traces. The shape of the traces in the profile suggest a mesa like structure of Ti on the substrate partly covered with a Cr droplet.

The corresponding EELS line profile is shown in figure 6.11 although part of the droplet was too thick for EELS analysis. This profile shows that there is no N in this Ti mesa. Both the EELS and the EDX profiles show the presence of some Cr in this Ti mesa. Figure 6.12 is a schematic diagram of this droplet. The bremsstrahlung was used to calculate the mass-thickness.

The X-ray maps and the line profiles imply that part of the substrate was protected from being etched away by the sputter cleaning process resulting in a Ti mesa like structure. This part of the substrate did not receive any CrN in the subsequent coating cycle because the droplet was shadowing it. The droplet must have arrived prior to the coating cycle. However, this droplet did not get coated with CrN in the coating cycle possibly because it was in poor contact with the substrate and consequently charged up as soon as ions arrived on it.

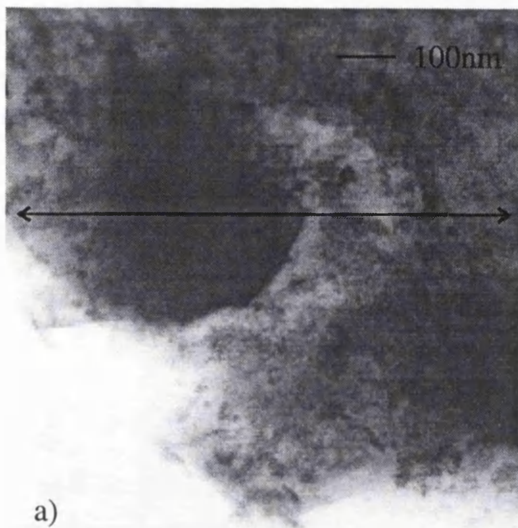

location of line profiles in figures 6.10 & 6.11

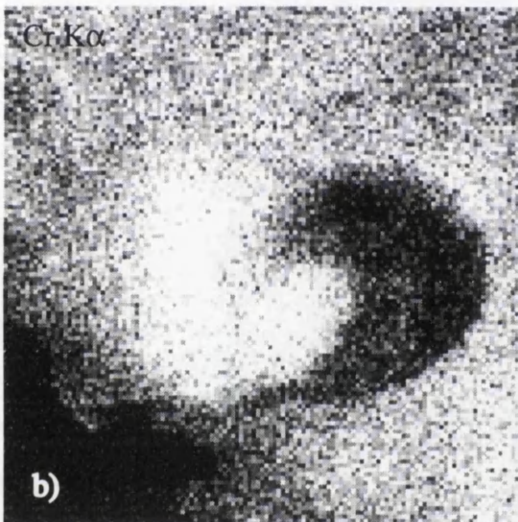

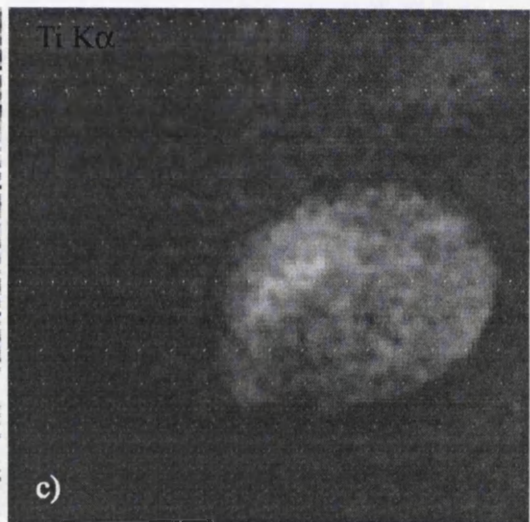

Figure 6.9 *Cr droplet in planar specimen of CrN on Ti(6%Al, 4%V).*

a) Bright field image

b) & c) Cr & Ti X-ray maps

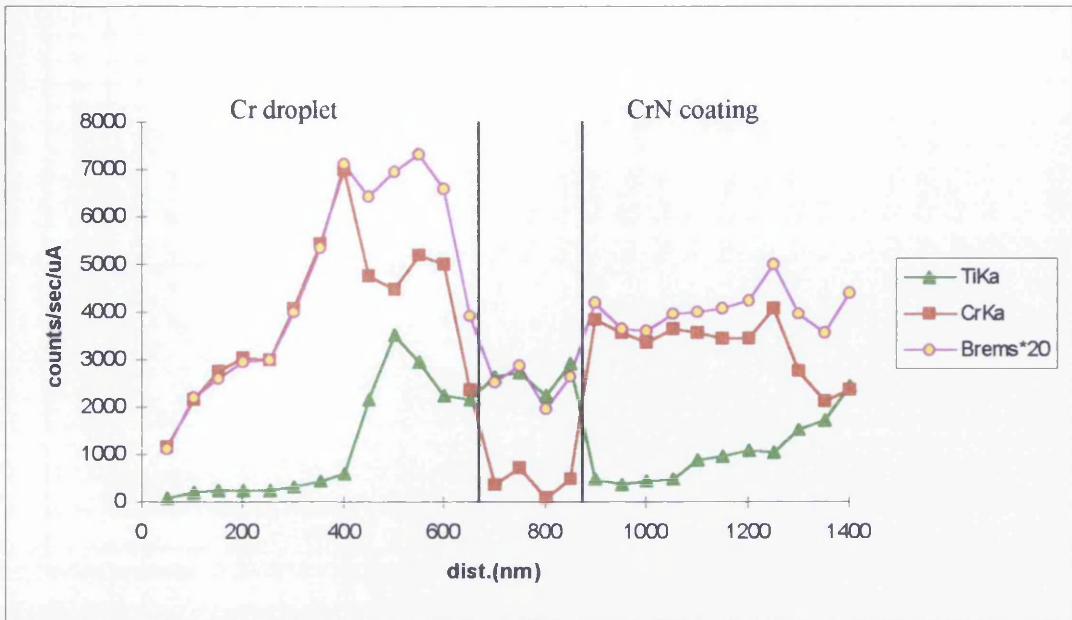

Figure 6.10 *EDX line profile across region in figure 6.9.*

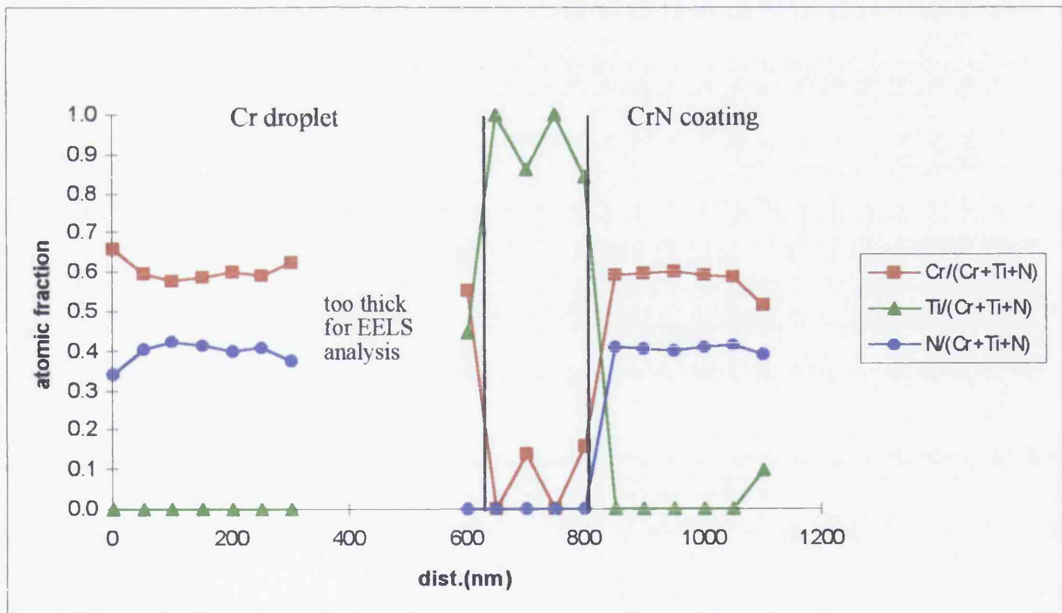

Figure 6.11 *EELS line profile across region in figure 6.9.*

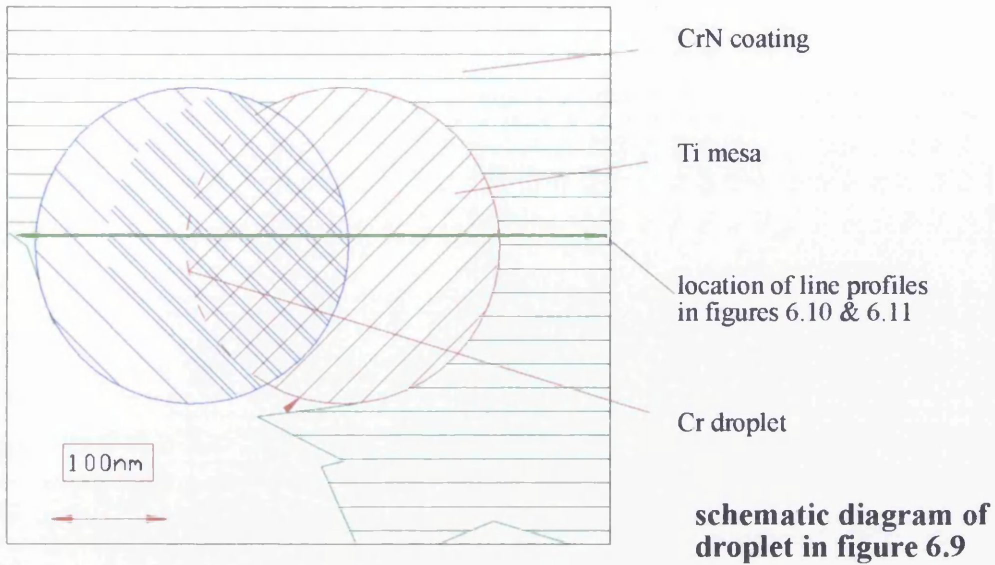

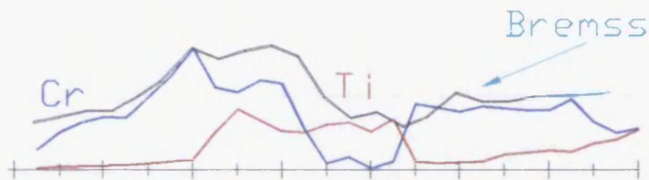

X-ray line profiles as in figure 6.10

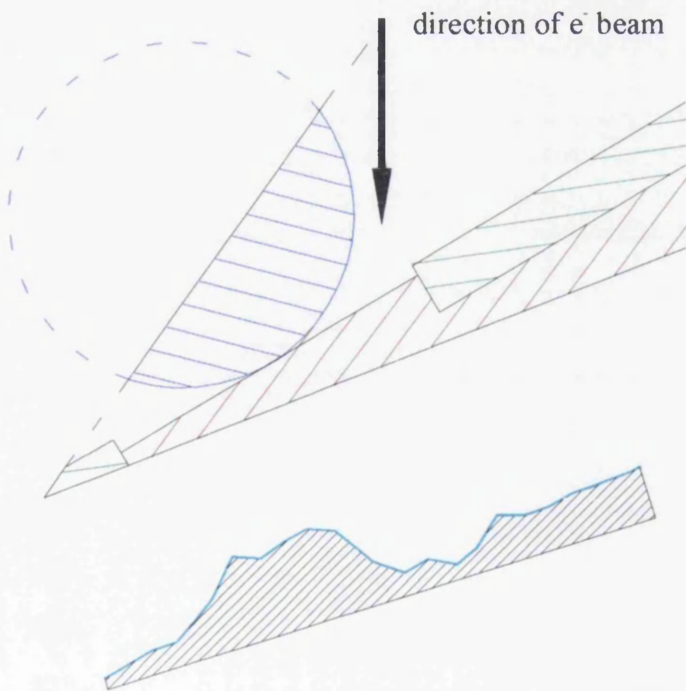

schematic of ion milled specimen

mass-thickness represented by X-ray Bremsstrahlung profile

Figure 6.12 *Schematic diagram of mesa droplet and surrounding material..*

Further ions were prevented from landing on the surface by the repulsive electric force.

Possible evidence for another mesa can be seen in figure 6.5, which shows a droplet in cross-section. The substrate surface under the droplet is higher than that of the surrounding substrate suggesting that the droplet protected the substrate under it from erosion. The height of the mesa suggests an erosion rate of about 1nm per Amp hour, which rate is smaller than that observed for Cr sputter cleaning of Ti. However, this rate was calculated assuming that the droplet arrived at the onset of the sputter cleaning process and therefore is a lower limit rather than an average value.

Coated droplet in cross-section

Figures 6.13a-b are bright field and ADF images of a droplet in cross-section. Figures 6.13c-f are Cr Kα and Ti Kα X-ray maps taken from the two boxed regions in figure 6.13a. A layer of Ti surrounding the droplet can be clearly seen in the Ti map in figure 6.13d. However, no such layer is apparent in the Ti map on the other side of the droplet in figure 6.13f. This suggests that the Cr sputter cleaning process deposited Ti onto the side of the droplet facing the cathode. The other side of the droplet did not receive a coating of Ti because the droplet shadowed its surface on this side from the cathode.

To summarise, EELS and EDX confirmed that the droplets consist of Cr and originated at the cathode. The thin layer of Ti observed on some of the droplets was etched from the substrate surface and subsequently redeposited during the sputter cleaning process. Some of the droplets were coated with sub-stoichiometric Cr_2N followed by sub-stoichiometric CrN.

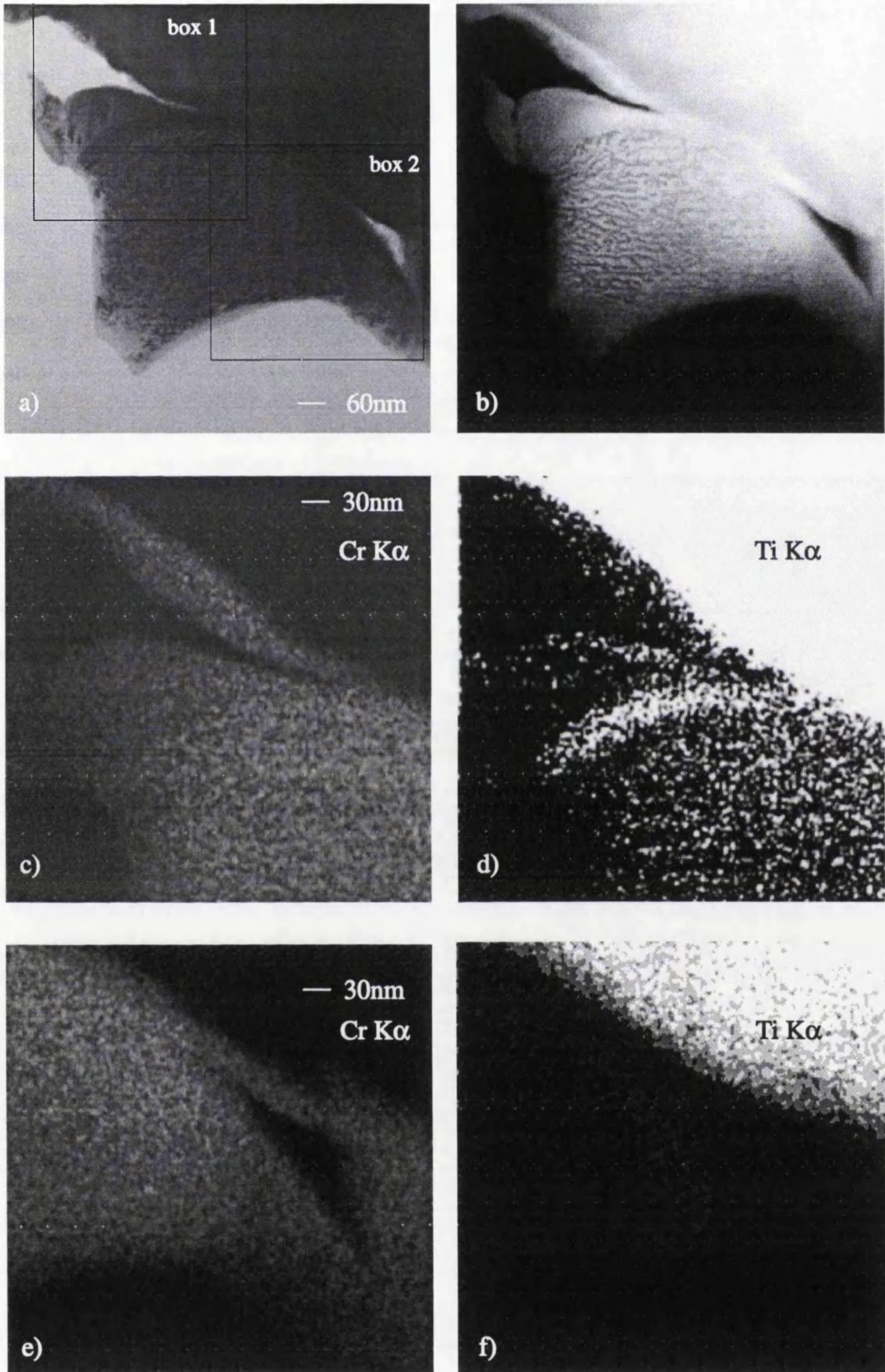

Figure 6.13 *Cr droplet in cross-sectional specimen of CrN on Ti(6%Al, 4%V)..*
a) bright feld image, b)ADF image
c) & d) Cr & Ti X-ray maps from region in box 1
e) & f) Cr & Ti X-ray maps from region in box 2.

6.6 Conclusions

There are several conclusions which can be drawn from the studies in this chapter. The number and sizes of droplets found on the samples depended upon the orientation and rotation of the substrate. The number of droplets decreased from a generous covering to very few as the angle between the substrate and cathode surfaces increased from 0° to 90°. The larger droplets smeared out along their direction of motion on arrival at the substrate but the smaller droplets solidified before reaching the substrate and therefore retained their spherical shapes.

The Cr droplets analysed in this chapter all appear to have arrived at the substrate during the sputter cleaning process. All of the droplets studied by Ljungcrantz et al (1994) had been deposited during the coating cycle as they were totally embedded in the TiN coating. The coatings that Ljungcrantz et al used were at least 3.5μm thick and therefore droplets deposited during the coating process were less likely to fall out because there was more coating to hold them in place.

In the case of Cr droplets on the Ti(6%Al, 4%V) substrate a thin layer of Ti partly covering some of these droplets was observed. This Ti was etched from the substrate by the energetic Cr ions bombarding the surface. Two droplets appeared to be sitting on a Ti mesa. These observations are further evidence for erosion of the Ti(6%Al, 4%V) substrate by Cr ions. The last chapter showed that the sputter cleaning of Ti with Cr ions resulted in the removal of a significant quantity of Ti. This chapter shows that the model in the last chapter was feasible although the erosion rates are possibly different.

During the coating cycle some of the droplets get coated with sub-stoichiometric Cr_2N followed by sub-stoichiometric CrN. This coating grows radially out from the droplets in columns. The growth direction in this radial

coating is different from that in the rest of the sample, where it is normal to the substrate surface. That is, the growth direction is always normal to the substrate surface regardless of the orientation or shape of the surface. This effect was also observed in the last two chapters where the coatings were deposited with different orientations to the substrate but the grain growth was always normal to the substrate surface. This leads to defects in the coating where the two coatings growing in the different directions meet.

The droplets shadow the substrate from the cathode. Consequently there are voids under the droplets and regions near the droplet which do not receive any coating.

The presence of droplets in coatings means that the resultant surface roughness is about three orders of magnitude greater than the intrinsic surface roughness of the coating. These droplets spoil the aesthetic appearance of the coating. Moreover, they lead to growth defects in the coating. These defects are caused by coatings with different growth directions meeting and also by the shadowing effect of the droplets.

CHAPTER 7

Conclusions and further work

The aim of this work was to study the microstructure and microchemistry of arc evaporated nitride coatings with emphasis on investigation of the interface region between the substrate and the coating. This interface region governs the adhesion of the coating which is crucial to its functional performance. In this chapter the observations and conclusions from the preceding chapters are reviewed and discussed in terms of the study as a whole. Finally some ideas are given for possible further work.

7.1 Effect of the sputter cleaning process on the substrate

Three different substrates were investigated, namely Ti(6%Al, 4%V), Ti and TiN. The Ti(6%Al, 4%V) and Ti substrates were sputter cleaned with Cr ions whereas Ti ions were used to clean the TiN substrates.

Ti(6%Al, 4%V) substrate

The polishing and Cr sputter cleaning of Ti(6%Al, 4%V) resulted in modification of the microstructure at the substrate surface. The grain sizes in the electron transparent region of the bulk substrate were typically of the order of 0.2-10μm but lots of smaller grains were found near the surface of the substrate with sizes in the range 10-100nm. Diffraction work performed on samples in section 4.6 showed that a lot of these small grains at the substrate surface were β-Ti(6%Al, 4%V). It is not clear whether these small β grains were a result of the polishing or the sputter cleaning process or a combination of both.

The microchemistry of the substrate was affected by the sputter cleaning process with Cr being incorporated in the substrate up to depths of about 20nm which resulted in an interface layer of graded composition. Examination of low-loss spectra from EELS data verified that this layer was an actual alloy of Cr and Ti. Inspection of the Ti-Cr phase diagram shows that there is complete solid solution of Cr in β-Ti at high temperatures and a small amount of diffraction evidence was obtained which showed that this alloy did have the bcc structure of the β-phase.

Investigation in chapter 6 of Cr droplets deposited on the Ti(6%Al, 4%V) substrate revealed that some of them were partly coated with a thin layer of Ti of the order of 15nm wide. This suggested that the sputter cleaning process was etching the substrate surface as well as implanting Cr ions. Further evidence for this was supplied by two droplets apparently sitting on mesa structures of the substrate where the droplets had protected the underlying substrate while the surrounding substrate was being etched. One of these droplets, which was in a cross-sectional specimen, suggested that the sputter cleaning had etched at an average rate of at least 1nm per Amp hour from the rotating substrate.

Ti substrate

Cr sputter cleaning of Ti in rotation gave similar results to those above, with removal of material from the substrate on an estimated scale of about 6nm per Amp hour and incorporation of Cr into the substrate over depths of about 10-30nm. The net material transfer during the sputter cleaning process was removal of material from the substrate.

TiN substrate

Chapter 5 also investigated Ti sputter cleaning of the TiN substrate which gave quite different results to those observed for the materials discussed above. The process did not remove a measurable amount of the TiN substrate but there was deposition of a layer of Ti, the width of which strongly depended upon the orientation of the substrate surface to the cathode surface. The interface between the Ti and the TiN substrate was about 10nm wide and of graded composition suggesting that either Ti had been implanted into the substrate or N had diffused out.

Discussion

The effect of the sputter cleaning process depended upon the materials that were being investigated. There was significant etching of the Ti(6%Al, 4%V) and Ti substrates but little if any of the TiN substrate. This difference is probably a result of differences in the surface stabilities of the materials involved but could also be a result of the different sputtering ions involved. The energy of the ion on arrival at the substrate is known to affect the nature of the process (Dorodnov, 1978) and this depends upon the element involved as well as the substrate bias. With Cr cathodes there is a greater percentage of

ions with multiple charges than with Ti cathodes, and furthermore the multiply charged Cr ions are more energetic than the Ti ions (Lunev et al, 1977).

A crystalline layer of graded composition was observed at each of the substrate surfaces studied above. These are unlike the amorphous interface regions observed with other substrate/coating systems. Amorphous regions were observed for Ti on Si (Hatto et al, 1996; this work), C on Si (Gerstner et al, 1995) and for Ti on Fe (Hatto et al, 1996). The nature of the resultant interface is dependent upon the mutual solubility of the substrate and the sputtering ion. If the materials have complete solid solutions then a crystalline interface can form but if the materials can only form discrete phases then the interface region is amorphous. However if sufficient energy is input to the system this amorphous region could recrystallise. This is possibly why Håkansson (1991) observed the presence of a recrystallised region after sputter cleaning steel with Ti. Yamada et al (1980) and Takagi (1984) noted that in the deposition of Si by ionised cluster beams that the crystallinity of the films depended upon the acceleration voltage.

Although the interface region was non-uniform its width decreased as the angle of orientation of the substrate surface to the cathode increased. The uniformity of the interface also increased as the angle increased. Similar observations were made by Hatto et al (1996) for Ti sputter cleaning of Si.

The presence of a graded interface region is known to improve the adhesion of the coating to the substrate (see e.g. Münz et al, 1989; Hovsepyan et al, 1991; Gerstner et al 1995). Gerstner et al noted that, with C coatings deposited on Si, mechanical failure occurred in the substrate prior to delamination of the coating and suggested that this might be due to mechanical damage resulting from the implantation of C during the sputter cleaning process. In the case of Cr sputtering of Ti(6%Al, 4%V) prior to deposition of CrN a similar problem could potentially occur with the formation of the $TiCr_2$ phase that is known to cause embrittlement (Polmear, 1981) and could thus lead to mechanical failure.

The deposition of Ti on TiN substrates during the sputter cleaning process explains the lack of success in recoating TiN tools unless the old coating is first stripped off.

7.2 Microstructure and microchemistry of the coatings

CrN coating

Deposition of CrN on Ti(6%Al,4%V) resulted in the initial deposition of a layer of fine grained sub-stoichiometric Cr_2N whose structure was confirmed to be hexagonal by examination of the ELNES on the N K edge in the EELS spectra. Conclusive diffraction evidence was not obtained from this layer because its narrowness and non-uniformity made it difficult to isolate its diffraction pattern. The presence of this layer, which was also confirmed by bright and dark field imaging and EELS compositional line profiles, is probably a result of the changeover between the sputter cleaning and the deposition cycles as confirmed by the relative thickness and time scale over which it was deposited.

Formation of the sub-stoichiometric Cr_2N was followed by columnar growth of sub-stoichiometric CrN the structure of which was confirmed to be fcc using the ELNES on the N K edge. The compositions of the coatings were not uniform, showing fluctuations within a given sample and variations between different samples. The relative amount of Cr in the coating appeared to decrease marginally as the angle of orientation between the substrate and the cathode surfaces increased. This change in Cr concentration could be due to the general forward directionality of the metal ions (Tuma et al, 1978); this forward directionality is decreased by gas scattering when there is N_2 gas

present in the chamber but may not be totally removed. However another explanation for the different compositions observed could be the different deposition rates experienced by substrates at different orientations and distances from the cathode.

The grain size in the coating was found to increase as the substrate bias increased with the average size roughly doubling for an increase in the substrate bias from -70V to -200V. More faults were observed in the coatings deposited at the lower bias. There is generally a decrease in internal stress as the substrate bias is increased (Martin et al, 1991) and this may be explained by the presence of larger grains with fewer faults. The higher energies resulting from the increased bias may cause more annealing of the coating as it is deposited. The average grain size also increased as the orientation between the substrate and the cathode increased but this effect was much less pronounced than that of the substrate bias.

The overall thickness of the coating was influenced by the orientation and rotation of the substrate in the chamber with a general trend of decreasing width as the angle of the substrate surface to the cathode surface increased. The thickness of the sub-stoichiometric Cr_2N layer followed the same trends as the overall coating thickness.

The presence of Cr droplets led to defects in the coatings. Shadowing of the substrate by the droplets resulted in voids. Growth defects were also observed where coating that grew radially out from some of the droplets met the coating that grew normal to the substrate surface.

The coating studied in section 4.6 showed {022} texturing normal to the substrate surface. X-ray diffraction data from other samples of CrN not discussed in this thesis gave {002} texturing for deposition on Si and {022} texturing for deposition on steel.

TiN coating

The effect of orientation and rotation on the thickness of coating deposited was more clearly seen with the TiN samples studied in section 5.4 where the thickness of TiN deposited decreased as the angle between the substrate and the cathode surfaces increased. The effect was not as pronounced as in the case of Ti deposition during the sputter cleaning process because gas scattering led to a more even distribution of TiN with orientation.

The deposition of material in the form of droplets also showed a strong dependence upon the orientation of the substrate to the cathode with the number of droplets deposited decreasing as the angle of orientation increased. The droplets were up to about 15μm in diameter and the larger droplets arrived at the substrate while still in a molten state.

These droplets not only spoil the aesthetic appearance of the coating but also causes the surface roughness to be about three orders of magnitude greater than the intrinsic surface roughness of the coating when deposited on a flat plane.

Discussion

The orientation and rotation of the substrate, the substrate bias and the gas pressure in the chamber have been shown to influence the microstructure and microchemistry of the coating. The non-uniformity of the coatings deposited by cathodic arc evaporation on non-planar substrates is one of the limitations of the coating technique. In practice this problem is overcome to a certain extent by the use of several cathodes, situated at various positions around the chamber, and by double rotation.

7.3 Analytical electron microscopy

The usefulness of analytical electron microscopy techniques for studying hard coatings has been displayed. Bright and dark field imaging, EELS, EDX and diffraction techniques were all employed in the investigations in this thesis.

In analysis of EELS data, the use of edges from standard compounds to remove the background from edges in similar compounds was demonstrated in section 3.2.2. This technique was particularly useful when the background contained ELNES from a preceding edge. The ability to scale the edge in the standard compound using the lattice parameters extended the range of compounds which the edge in the standard compound could be used for. The usefulness of ELNES is anticipated to increase in the next few years but other parts of the EELS spectra are still useful in analysis. For example, the first plasmons in the low-loss spectra were used to verify the presence of an alloy in section 4.5.

7.4 Possibilities for further work

There are clearly some experiments which should be done for completion of the above studies, such as investigation of recoating with TiN at 45° in rotation.

The diffraction work presented in this thesis is very incomplete and a much more thorough diffraction study of all or at least some of the samples studied is desirable. It is hoped that some of this work will be completed in the near future. The results obtained using the non-standard mode of the Philips CM20 in section 4.6 improved as the use of this mode was practised and it is anticipated that it should be possible to obtain isolated diffraction patterns from the Ti:Cr and sub-stoichiometric Cr_2N interface layers. Diffraction

experiments such as those described in section 4.6 would also allow the texture in the CrN coatings to be examined in more detail to see how it is affected by changes in the orientation and substrate bias during deposition.

The effect of the sputter cleaning process has been shown to depend upon the sputtering ion and the substrate material. This study could be extended to look at a wider range of substrate materials and sputtering ions. Following on from this work the Cr sputter cleaning of TiN could be investigated to see if etching of the substrate occurs.

In more general terms, there are clearly other process parameters which could influence the properties of both the interface region and the coating. These should be investigated more fully in order to establish the criteria for reproducible interface regions.

The effect of the changeover from the sputter cleaning to the deposition process is clearly important and should be studied in more detail.

The rate of arrival of the ions (or rate of deposition of the coating) at the substrate could also play an important role in influencing the interface and the coating properties, and should thus be investigated.

This work has looked at the influence of various process parameters on the microstructure and microchemistry of nitride coatings and the interface regions between the coating and the substrates. In order to correlate the effects observed with the properties of the coatings some mechanical testing of the coatings should be done which would quantitatively examine the adhesion, wear etc. of the coatings.

APPENDIX A1

Specimen preparation

A1.1 Planar specimens

This technique was developed by Scott (private communication) but is given in detail below as it is not published.

A piece of sample with a coated surface area of about 5mm by 10mm was cut from the sample using an Isomet low speed diamond saw. The sample was waxed onto a glass slide with the coating side down and back-thinned by hand to a thickness of 100μm using SiC paper. The final thinning was done with 600 grade SiC paper and the sample was then polished using 3μm diamond paste on a hand polisher to remove any deep scratches.

3mm diameter discs could be cut from the sample using a metal punch but it was found that the stress in the coating was sufficient to bow the thin metal foil so to provide extra mechanical support 3mm copper slot grids were glued to the substrate side of the sample using 'Devcon 5 minute epoxy'. Excess glue was removed using a scalpel after a few hours and the remainder was left overnight to harden. The 3mm discs were removed by cutting them out of the sample

using a scalpel, and cleaned in a reflux condenser for about an hour using inhibisol to remove any wax.

The specimen was mounted on a stub using bees wax with the substrate side up and dimpled using a Gatan model 656 dimple grinder. Dimpling was done at maximum rotation speed using a grinding weight of 40g and a felt polishing wheel with 3μm diamond paste.

The depth of the dimple, d which can be estimated using equation A1.1,

$$d \approx \frac{r^2}{D} \quad \text{(A1.1)}$$

where r is the radius of the dimple and D is the diameter of the wheel, was used to monitor the thickness of the specimen at the centre of the dimple. Dimpling was continued until the thickness at the centre of the specimen reached ~30μm.

The specimen and the stub were placed in an extraction thimble in the reflux condenser and cleaned in inhibisol for about an hour to remove the specimen from the stub and clean off all the wax.

The specimen was ion beam thinned from the substrate side with Ar gas in a Gatan 600 series duomill. A glass cover slip waxed on the underside of the specimen support plate on the stage prevented redeposition of the sputtered material onto the coating. The specimen was cooled using liquid nitrogen to reduce damage from the ion beam. The ion beam was set at 14° to the specimen with an ion current of 0.75mA and 5kV. The specimen was set to rotate with a constant speed during thinning. An automatic terminator with its sensitivity set at a maximum was used to stop the thinning process as soon as a hole was detected in the specimen. If further thinning of the specimen was required it was done at 6°.

A1.2 Cross-sectional specimens

The preparation technique used for the cross-sectional specimens is essentially the same as that described by Scott et al (1996). Modifications to the technique required for preparation of the specimens examined in this thesis are outlined below.

Scott et al (1996) suggested the use of a Si indicator strip to monitor the thickness of the specimen during mechanical thinning of opaque materials. This technique was unsuccessful for preparation of CrN coated Ti(6%Al, 4%V) specimens because the ion beam preferentially thinned the Si strip. Successful specimens were obtained using the technique described by Scott et al without the use of an indicator strip. The specimen thickness prior to dimpling was measured with a micrometer, and during dimpling using the gauge on the dimple grinder. Even with ion milling times of up to ~60hours successful specimens were obtained. If necessary the specimen was thinned at an angle of 6° after perforation.

For the TiN samples on the Si substrates there were serious problems with preferential thinning leading to the formation of bridges of opaque coating while the Si thinned away on either side. If the ion milling was continued the bridges snapped and fell out due to lack of mechanical support. This problem was overcome by ion milling for the first two hours at 8° and then reducing the angle to 6° for the remainder of the time. The specimen was turned every ½ hour because the specimen stage used only permitted thinning from one side.

A1.3 Preparation of specimens from standard powders

The CrN and Cr_2N powder standard specimens were prepared by crushing some powder in propan-2-ol with a pestle and mortar and pipetting a few drops of the colloid onto a grid containing a holey carbon film. It was found that it was necessary to crush the Cr_2N powder for several minutes otherwise most of the electron transparent regions were found to consist of CrN. This showed that there was contamination of the Cr_2N making it more difficult to break than the CrN which was more brittle.

LIST OF REFERENCES

Ahn, C.C. and Krivanek, O.L. (1983) EELS Atlas. A joint project of ASU HREM facility and Gatan.

Aharonov, R.R., Coll, B.F. and Fontana, R.P. (1993) *Surf. Coat. Technol.* **61**, 223-226.

Bearden, J.A. (1967) X-ray wavelengths and X-ray atomic energy levels. National Standards Reference Data Series- National Bureau of Standards. NSRDS-NBS, Washington.

Benninghoven, A., Rüdenauer, F.G. and Werner, H.W. (1987) Secondary Ion Mass Spectrometry Basic Concepts, Instrumental aspects, applications and trends. John Wiley & Sons, Inc., New York.

Bergman, C. (1988) *Surf. Coat. Technol.*, **36**, 243-255

Bethe, H. A. (1930) *Ann. Der Phys.* **5,** 325-400.

Blix, R. (1926) *J. Iron Steel Inst.* **114**, 117, 229-239.

Chapman, J.N., Nicholson, W.A.P. and Crozier, P.A. (1984) *J. Micros.* **136,** Pt 2, 179-191.

Cliff, G. and Lorimer, G.W. (1975) *J. Micros.* **103,** 203-207.

Craven, A.J. (1995a) in EMAG'95 Birmingham. IOP Conf. Series, **147**, 267-272.

Craven, A.J., (1995b) *J. Micros.* **180,** Pt 3, 250-262.

Craven, A.J. and Buggy, T.W. (1981) *Ultramicroscopy.* **136**, 2, 227.

Crewe, A.V. (1971) 'High Intensity Electron Sources and Scanning Electron Microscopy' in Electron Microscopy and Materials Science. ed. U. Valdre, 162

Daalder, J.E. (1976) *J. Phys. D: Appl. Phys.*, **9**, 2379-2395

Dobrev, D. (1982) *Thin Solid Films.* **92**, 1-2, 41-53

Dorodnov, A.M. (1978) *Sov. Phys. Tech. Phys.*, **23**, 9, 1058-1065

Edington, J.W. (1975) 2 Electron Diffraction in the Electron Microscope. The MacMillan Press Ltd. London.

Egerton, R.F. (1985) Electron Energy-Loss Spectroscopy in the Electron Microscope. Plenum Press, New York.

Eriksson, S. (1934) *Jernkontorets Annaler* **118**, 530

Erturk, E., Heuvel, H.J. and Dederichs, H.G. (1989) *Surf. Coat. Technol.*, **39-40**, 435

Gåhlin, R., Bromark, M., Hedenqvist, P., Hogmark, S. and Håkansson, G. (1995) *Surf. Coat. Technol.* **76-77**, 174-180.

Gerstner, E.G., McKenzie, D.R., Puchert, M.K., Timbrell, P.Y. and Zou, J. (1995) *J. Vac. Sci.Technol.* **13**, 2, 406-411.

Goldschmidt, H.J. (1967) Interstitial alloys. Butterworths, London.

Goldstein, J.I., Costley, J.L., Lorimer, G.W. and Reed, S.J.B. (1977) SEM/77 (ed. Johari, O.) IITRI, Chicago, 1, 315

Habig, K.H. (1986) *J.Vac. Sci. Technol. A.* **4**, 6, 2832-2843.

Håkansson, G (1991) Linköping Studies in Science and Technology. Dissertations. No. 255, Linköping University, Sweden.

Hall, T.A. (1971) in Physical Techniques in Biological Research. (ed. Oster, G.) Academic Press, New York, 157-275.

Hansen, M. (1958) Constitution of Binary Alloys. McGraw-Hill Book Company, New York.

Hantzsche, E. (1981) *Physica* **104C**, 3-16.

Hatto, P. Private communication.

Hatto, P., Scott, C., McGibbon, M., Craven, A., Wilkinson, C., Spencer, T., Rodgers, T., Green, T., Davies, C., Holmes, A. and Tedder, D. (1996) The

Investigation of Synergistic Effects in PVD Coatings with nanometre Multilayer Structures. Final Report of Link Nanotechnology Initiative Project.

Hauzer Holding BV (1990) *Eur. Patent Appl. PCT/EP90, 01032.*

Heinrich, K.F.J. (1979) Mass absorption coefficients for electron probe microanalysis. *National Bureau of Standards Publication,* Gaithersburg, MD. USA.

Hovsepyan, P.E. and Dimitrov, M.T. (1991) Int. Conf. IPAT-91, Brussels.

Hovsepian, P. and Popov, D. (1994) *Vacuum* **45**, 5, 603-607.

Inokuti, M. (1971) *Rev. Mod. Phys.* **43,** 297-347.

Ives, M., Cawley, J. and Brooks, J.S. (1993) *Surf. Coat. Technol.* **61**, 127-132.

Jacobson B.E., Nimmagadda, R. and Bunshah, R.F. (1979) *Thin solid films.* **63,** 333-339.

Jiang, H., Tao, K. and Li, H. (1995) *Thin Solid Films.* **258,** 51-55.

Kaye, G.W.C. and Laby, T. H. (1975) Tables of physical and chemical constants and some mathematical functions. Longman, London 14th Ed.

Krause, M.O. (1979) *J. Phys. Chem. Ref. Data.* **8,** No. 2, 307-327.

Kuruta, H., Lefevre, E., Colliex, C. and Brydson, R. (1993) *Phys. Rev. B* **47,** 13763-13768.

Leapman, R.D., Rez, P. and Mayers, D.F. (1980) *J. Chem. Phys.I.* **72**, 2, 1232-1243.

Ljungcrantz, H., Hultman, L., Sundgren, J.-E., Håkansson, G. and Karlsson, L. (1994) *Surf. Coat. Technol.* **63**, 123-128.

Lunev, V.M., Padalka, V.G. and Khoroshikh, V.M. (1977) *Sov. Phys. Tech. Phys.* **22**, 7, 858-861.

Mack, M. (1990) Surface Technology. Wear Protection. AG & Co. Germany.

Marinov, M. (1977) . *Thin solid films.* **46**, 267.

Martin, P.J. (1986) *Vacuum* **36**, 10, 585-590.

Martin, P.J., Netterfield, R.P., Kinder, T.J. and Descôtes, L. (1991) *Surf. Coat. Technol.* **49**, 239.

Martin, P.J., Netterfield, R.P., McKenzie, D.R., Falconer, I.S., Pacey, C.G., Tomas, P. and Sainty, W.G. (1987) *J. Vac. Sci. Technol. A.* **5**, 1, 22-28.

Matthews, A. (1985) *Surf. Eng.* **1**, 2,93-104.

McKenzie, D.R., Yin, Y., McFall, W.D. and Hoang, N.H. (1996) *J. Phys.: Condens. Matter* **8,** 5883-5890.

Misell, D.L. and Atkins, A.J. (1973) *Philos. Mag.* **27,** 95-106.

Mochvan, B.A. and Demshishin, A.V. (1969) *Fiz. Met. Metalloved.* **28**, 653.

Münz, W.D. (1991) *Surf. Coat. Technol.* **48**, 81

Münz, W.D., Schroeder, J., Petersein, H., Håkansson, G., Hultman, L. and Sundgren, J.E. (1989) *Int. Conf. Surtec. '89, October 11-13.* **5**, 1, 22

Natoli, C.R. (1983) in EXAFS and Near Edge Structure (ed. by Bianconi, A., Incoccia, L. and Stipcich, S.), Springer Series in Chemical Physics 27, Springer Verlag, Berlin.

Nicholson, W.A.P. (1994a) Analytical electron microscopy II. Practical problems with energy dispersive spectrometry. EMAS 1994 proceedings.

Nicholson, W.A.P. (1994b) Standardless quantitation of thin film specimens. *Mikrochim. Acta.* **114/115,** 53-70.

Paterson, J.H., Chapman, J.N., Nicholson, W.A.P. and Titchmarsh, J.M. (1989) *J Micros.* **154,** Pt 1, 1-17.

Perry, A.J. (1989) *Thin Solid Films* **170**, 1, 63-70.

Perry, A.J. (1990) *J. Vac. Sci. Technol. A.* **8**, 3, 1351-1358.

Pinsker, Z.G. and Abrosimova, L.N. (1958) *Sov. Phys. Crystallog.* **3**, 285

Plyutto, A.A., Ryuzhkov, V.N. and Kapin, A.G. (1964) *Zh. Eksp. Teor. Fiz.* **47**, 494 (*Sov. Phys. JETP* **20**, 328 (1965))

Polmear, I.J. (1981) Light Alloys : metallurgy of the light metals. Edward Arnold, London.

Robins, J.L. and Swan, J.B. (1960) *Proc. Phys. Soc.* (London) **76**, 857

Robinson, P.A. and Matthews, A. (1990) *Surf. Coat. Technol.,* **43-44**, 288

Rother, B. (1988) *Surf. Eng.* **4**, No. 4, 335-341

Scott, C.P. Private communication

Scott, C.P., Craven, A.J., Hatto, P. and Davies, C. (1996) *J. Micros.* **182**, 3, 186-191.

Sundgren J.-E., Rockett, A. and Greene J.E. (1986) *J. Vac. Sci. Technol. A.* **4**, 6, 2770-2783.

Takagi, T. (1984) *J. Vac. Sci. Technol.* **A2**, 2, 382-388.

Thornton, J.A. (1974) *J. Vac. Sci. Technol.* **11**, 666

Tuma, D.T., Chen, C.L. and Davies, D.K. (1978) *J. Appl. Phys.*, **49**, 7, 3821.

Vyskocil, J. and Musil, J. (1990) *Surf. Coat. Technol.* **43/44,** 229-311.-

Wang, D., Wang, X., Yang, G., Liu, X., Jia, Y., Zhou, G. and Li, G. (1995) *J. Appl. Phys.* **77**, 7, 2945-2951.

Ward-Close, C.M. (1982) in Royal Aircraft Establishment Technical Report 82035, London

Wehenkel, C. and Gauthé, B. (1974) *Phys. Staus. Solidi (b)* **64**, 515-525.

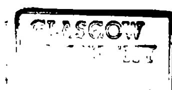

Williams, D.B. and Edington, J.W. (1976) *J. Micros.*, **108**, 113-145.

Yamada, I., Saris, F.W., Takagi, T., Matsubara, K., Takaoka, H. and Ishimyama, S. (1980) *Jpn. J. Appl. Phys.* **19**, L181

Zaluzec, N.J. (1979) in Introduction to Analytical Electron Microscopy. (eds. J.J. Hren, J.I. Goldstein & D.C. Joy) Plenum, New York.